DEPARTAMENTO DE ASTROFISICA

Universidad de La Laguna

Modeling of Non-ideal Magnetohydrodynamic Effects in the Solar Atmosphere.

Memoria que presenta
D. Pedro Alejandro González Morales
para optar al grado de Doctor por
la Universidad de La Laguna.

Directora:
Dra. Elena Khomenko

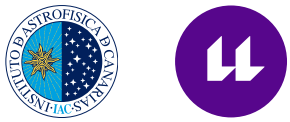

INSTITUTO Đ ASTROFISICA Đ CANARIAS
Abril 2020

Examination date: June, 2020
Thesis supervisors: Dr. Elena Khomenko

Part of the material included in this document has been already published in *Astronomy & Astrophysics* and *Astrophysical Journal of Astronomy*

A mis padres,
a mi hermana

Resumen

Comprender la conexión que establece el campo magnético entre las capas de la atmósfera solar es uno de los desafíos más importantes de la Física Solar. Sabemos que estas regiones están formadas por plasma débilmente ionizado, pudiéndose llegar en algunos lugares a tener una fracción de ionización tan baja como 10^{-4}. En estas condiciones, la presencia de neutros puede llegar a ser importante. La interacción entre el plasma débilmente ionizado y los campos magnéticos conlleva la aparición de efectos no ideales en el plasma, y con ellos aparecen desviaciones del marco establecido por la magnetohidrodinámica (MHD) ideal. Efectos no ideales son la difusión Ohmica, la difusión ambipolar, el efecto Hall, y el efecto de batería de Biermann, siendo la difusión ambipolar el único directamente relacionado con la presencia de neutros. Estos efectos aparecen en la ley generalizada de Ohm así como en la ecuación de la energía en forma de términos extras, conformando así el sistema de ecuaciones de la MHD no ideal. Bajo ciertas condiciones, estos términos pueden introducir restricciones importantes a la hora de resolver numéricamente las ecuaciones, por ejemplo sobre el paso temporal usado en la integración numérica o en la estabilidad del los esquemas numéricos.

En esta tesis, dos esquemas numéricos han sido introducidos en el código numérico MHD Mancha3D para solventar esas limitaciones. El primero de ellos es conocido como "super time-stepping" (STS) y está diseñado para superar las limitaciones impuestas sobre el paso temporal en ecuaciones parabólicas pudiéndose aplicar a la difusión ambipolar. El segundo esquema es conocido como "Hall diffusion scheme" (HDS) y está diseñado para superar las limitaciones introducidas por el término Hall cuando este domina. Estas dos técnicas numéricas pueden ser usadas al unísono mediente la técnica conocida como "Strang operator splitting". La validación para cada uno los esquemas mencionados es realizada comparando los resultados numéricos con las soluciones analíticas de los diferentes experimentos.

A continuación, usando el nuevo código, se han realizado una serie de experimentos numéricos para estudiar la transformación de modos mediante el término Hall en una estratificación quasirealista con parámetros termodinámicos semejantes a los de la atmósfera solar. Los resultados obtenidos confirman la eficacia del mecanismo para el caso solar. La eficiencia de la transformación de modos es sensible al ángulo existente entre el vector de ondas y el campo magnético así como de la frecuencia de la onda. Además, la eficiencia se incrementa cuando la dirección de propagación está alineada con la dirección del campo y con la frecuencia de las ondas.

Por último, han sido realizadas simulaciones realistas en tres dimensiones de la dínamo local solar donde el campo magnético ha sido iniciado mediante el efecto batería. Este campo magnético semilla es amplificado hasta niveles solares mediente la dinamo local asociada a los movimientos convectivos. El efecto Ambipolar disipa las perturbaciones incompresibles asociadas a las ondas magnéticas, reduciéndose el flujo de Poynting y convirtiendo la energía magnética en energía térmica. El término Hall introduce un nuevo mecanismo para la trasformación de modos fast-to-Alfvén y genera corrientes adicionales. Debido a su naturaleza no compresiva de las ondas Alfvén tenemos que estas pueden viajar

hacia capas superiores y que las corrientes generadas pueden ser disipadas por la difusion ambipolar, cerrándose de esta manera el ciclo de calentamiento atmosférico. Por lo tanto, la acción de estos tres efectos no ideales puede ser considerada como un mecanismo muy atractivo para la generación, transporte y calentamiento de la cromosfera y/o capas superiores de la atmósfera solar.

Abstract

Understanding the connection between solar atmospheric layers through the magnetic field is a challenging task in solar physics. These regions are form by plasma weakly ionized and in some places the ionization fraction can be as low as 10^{-4} meaning that the presence of neutrals could be important. The interaction of weakly ionized plasma with magnetic fields entails the arise of non-ideal effects and the departure of the ideal magnetohydrodynamic (MHD) framework. Non-ideal effects are Ohmic diffusion, ambipolar diffusion, the Hall effect, and the Biermann battery effect, being the ambipolar diffusion the only one directly related to the presence of neutrals. These effects appear as a series of extra terms into the generalized Ohm's law and into the total energy equation, conforming this way the non-ideal MHD set of equations. Under certain conditions, these terms could introduce severe restrictions for solving numerically the equations, for example on the integration time step or compromising the stability of the numerical scheme.

In this thesis, two numerical schemes are introduced into the MHD numerical code Mancha3D to overcome those limitations. The first of them is known as super time-stepping (STS) and it is designed to overcome the limitations imposed over the temporal time step by parabolic equations and can be applied to the ambipolar diffusion term. The second scheme is called the Hall diffusion scheme (HDS) and it is used when the Hall term becomes dominant. These two numerical techniques can be used together by using the Strang operator splitting technique. The validation for each of these schemes is provided by comparing the analytical solution with the numerical one for a suite of numerical tests.

Next, using the new code, a set of numerical experiments are performed to study the wave mode transformation by means of the Hall term into a quasi-realistic stratification in thermodynamic parameters resembling the solar atmosphere. The results confirm the efficacy of the mechanism for the solar case. The efficiency of mode transformation is a sensitive function of the angle between the wave propagation direction and the magnetic field, and of the wave frequency. It also increases when the field direction and the wave direction are aligned for increasing wave frequencies.

Finally realistic three-dimensional simulations of solar local dynamo where the magnetic field is seeded by the battery effect are performed. This magnetic field is amplified to solar values by the convective local dynamo. Ambipolar effect allows to dissipate incompressible perturbations associated to magnetic waves removing the magnetic Poynting flux and converting the magnetic energy into the thermal energy. Hall term introduces a new fast-to-Alfvén mode transformation mechanism and helps generating currents. The Alfvén waves generated could travel to upper layers and the currents could be dissipated by the ambipolar diffusion closing the cycle. The action of all three effects can be considered as an attractive mechanism of energy generation, transport, and chromospheric heating.

Contents

1

Introduction

This reservoir can scarcely be other than the sub-atomic energy which... exists abundantly in all matter; we sometimes dream that man will one day learn how to release it and use it for his service. The store is well-nigh inexhaustible, if only it could be tapped.

- Arthur Stanley Eddington, 1920

Since many years ago, the human kind have looked at the sky and wonder about its mysteries. The Sun was probably one of the first astronomical bodies we notice and tried to understand better. It is during the twentieth century when it has gradually became clear that many of the phenomena observed about the Sun such as sunspots, prominences or plage regions are related to the existence of the magnetic field. Historically, the Sun has been viewed either as, *quiet Sun* where all the magnitudes change with the radius symmetrically and the magnetic field is negligible and an *active Sun* over in the latter view all the transient structures (sunspots, prominences, etc.) are characterized by the existence of magnetic field. The Sun is an ordinary G2 V spectral type star, an enormous ball of plasma held together by its own gravity. The interior of the Sun is hiden from us and only the surface can be seen directly, however thanks to the helioseismology it is possible to recover properties of the solar interior by measuring the solar oscillations. Through this technique, the interior of our star can be inferred and divided into three main parts namely the core, the radiative zone and the convection zone as sketched in Fig. 1.1.

The energy of the Sun is produced in its core by nuclear reaction as Eddington pointed out in 1925. This energy escapes to the exterior as energetic photons travelling through the radiative zone during many years by continuous absorption and emission (radiative diffusion) until the above layer, the convection zone. Once those photons reach the convection zone, a parcel of plasma can transport heat as it rises to the upper layers and yields some energy to the surrounding before falling and getting hot again. The lower boundary of the convection zone was called by Spiegel & Zahn (1992) *tachocline* and has a strong shear in the angular velocity. This shear could deform magnetic field lines lying originally in the meridional planes building up a strong toroidal magnetic field thus creating the main ingredient of the $\alpha\Omega$ dynamo model. On the top of the convection zone lies the solar atmosphere, a region where the photons can escape as radiation to the universe, being then possible to measure phenomena such as the oscillations generated by the convective motions.

The solar atmosphere is then an interface between the solar interior and the interstellar space. It is formed by three regions, from bottom to top we have the photosphere, the chromosphere and the corona as can be seen in Fig. 1.1 or in more detail in Fig. 1.2. The photosphere is the deepest and densest layer of the solar atmosphere. It is the layer where the solar interior become transparent for the radiation and the photons can escape. Usually it is defined as the surface where the optical depth

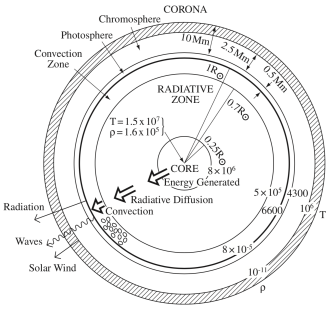

FIGURE 1.1— Schematic structure of the Sun indicating the sizes of various regions, not drawn to scale. The shaded region represents the highly variable boundary between chromosphere and corona (from 2.5 to 15 Mm). Temperatures are expressed in Kelvin and densities in kg m^{-3} (Priest 2014).

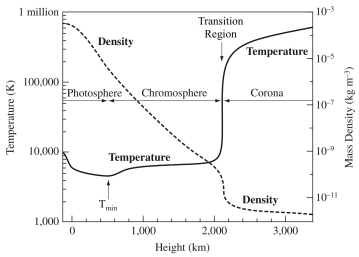

FIGURE 1.2— Schematic structure of the solar atmosphere showing the mean variation of temperature and density with height according to the VAL model by Vernazza et al. (1981). Courtesy Eugene Avrett.

for the radiation at 500 nm becomes the unity ($\tau_{500} = 1$). The chromosphere is an irregular layer and optically thick in strong spectral lines it is located on top of the photosphere and expanding up to the transition region. The transition region is a very thin layer which separates the chromosphere and corona and it is where the thermal conduction start to kick off. Static and stratified models such as the model Vernazza-Avrett-Loeset (VAL) locates it around 2 Mm height from the photosphere (Vernazza et al. 1981), see Fig. 1.2. The corona extends from the transition region to the heliosphere, the outer layer of the solar atmosphere and where our planet is submerged. Figure 1.3 is a composite image obtain from data of the Solar Dynamics Observatory (SDO) using different instruments and wavelength where it is possible to see all the atmospheric layers mentioned above (Pesnell et al. 2012).

Solar convection zone is an important part of our Sun since many important processes take place there. The most prominent feature of the solar surface are the sunspots and the granulation pattern at the solar surface. The granulation pattern was first observed and described by Herschel (1801) as a pattern of *corrugations* and *indentations* of the luminous "hot clouds" which are floating over the cooler solar surface. The term *granules* was assigned by Dawes (1864) in response to the description of Nasmyth (1865) as "willow leaves", which was in the correct track concerning the temperature as a driver. The controversy lasted until 1896 when Janssen showed some good photographs of the solar surface and its granulation pattern as Dawes coined, see Fig. 1.4. Since then, several observation have been made giving us information about it morphology and temporal evolution as well as its relation with the heat transport in the interior of the Sun by convection. From those observations is inferred the existence of magnetic fields all over, which modify the convective motions via the Lorentz force inhibiting plasma motion perpendicular to the field lines (Alfvén 1943). As a consequence, a suppression appears in the convective energy transport and/or a modification in the generation of waves. This inhibition produces for example one of the most recognizable structures in the photosphere, the sunspots. Those regions are darker than the surrounding due to the fact that their magnetic field strength is enough to inhibit the convective motions and produce a temperature dropping.

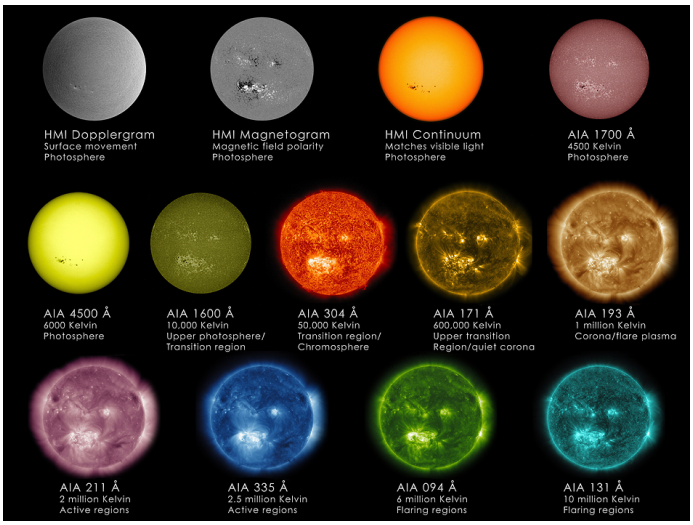

FIGURE 1.3— "The Many Faces of the Sun", a composite image from the Helioseismic and Magnetic Imager (HMI) and the Atmospheric Imaging Assembly (AIA) instruments onboard the Solar Dynamics Observatory (SDO) spacecraft (Scherrer et al. 2012; Lemen et al. 2012; Pesnell et al. 2012). Credit: NASA/SDO. At the top, 1700 shows in ultraviolet light continuum the solar surface and the chromosphere. In the middle row, 4500 shows in white light continuum the photosphere, 1600 shows in C IV the transition region between the photosphere and the lowest levels of the chromosphere, 304 shows in He II the upper transition region and the chromosphere, 171 shows in Fe IX the quiet corona and coronal loops, 193 shows in Fe XII and Fe XXIV a slightly higher region of the corona and solar flares. In the lower row, 211 shows in Fe XIV hotter active region in the corona, 335 shows in Fe XVI also active regions in the solar corona, 94 shows in Fe XVIII regions of the corona during solar flares and 131 shows in Fe XX and Fe XXIII material in flares.

Since the first theoretical studies of Chandrasekhar (1961), several numerical magneto-convection experiments have been done. The first numerical experiment was done by Weiss (1966) and, due to the limitations in computational power, opened a path where highly idealized models are used to reproduce some physical processes together to the use of analytical tools for a better comprehension of the phenomena. The purely kinematic model of Weiss (1966) was extended by Galloway et al. (1977) to the dynamical regimen and later on by Hurlburt & Toomre (1988) taking into account compressibility effects. This idealized approach assumes in general an ideal gas equation of state (EOS) and an energy transport done mainly by convection. This approach has been useful to gain a physical insight of the convective properties and since then has been used by several authors (e.g., Galloway et al. 1977; Hurlburt & Toomre 1988; Cattaneo 1999; Abbett et al. 2000; Hurlburt & Rucklidge 2000; Cattaneo et al. 2003; Bushby et al. 2008). With the improvements in computation power a new and complementary approach emerged with the simulations carried out by Nordlund (1982, 1983). In these three-dimensional simulations of solar granulation, the anelastic approximation was considered together with an imposed external magnetic field and, for the first time, a non-grey radiative transfer

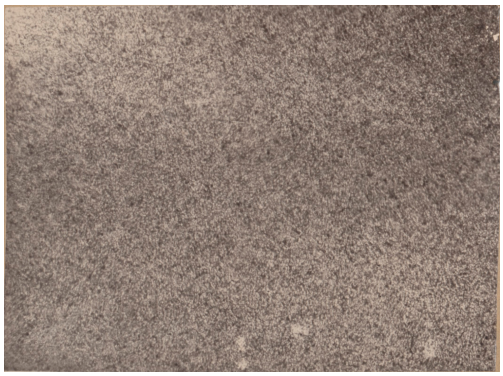

FIGURE 1.4— Solar surface image taken on September 9th, 1883 at the *Observatoire de Meudon* showing the granulation pattern with enough spatial resolution to end the debate around its shape (Solar disc diameter $0''.894$, north is on the left). Extracted from Janssen (1896).

for the energy transport. This realistic approach includes complex physics to aim a direct comparison with observations and vice versa, this is, to provide artificial data cubes for testing observational tools and procedures. For example, in the upper convection zone and photosphere a local thermodynamic equilibrium (LTE) is assume. In the chromosphere, a non-local thermodynamic equilibrium (NLTE) effects are also included, as it were done in the *Bifrost* code (Skartlien et al. 2000; Hayek et al. 2010; Gudiksen et al. 2011; Leenaarts et al. 2011; Carlsson & Leenaarts 2012). Partial ionization of several elements is considered, and to calculate the temperature and pressure, a tabulated EOS is used taking into account the LTE ionization of elements or molecules formation. However, these realistic simulations, due to the solar diffusivities are smaller than the simulated one, it fail in modeling the solar conditions. This imply that it is impossible at the same time capture structures of several megameters and resolve the diffusive length scales. This means that all realistic simulations parametrize the sub-grid effects trying to obtain a realistic description of them on the numerical resolved scales. More information about those two approach can be found in the review done by Schüssler (2001), Nordlund et al. (2009), or Stein (2012).

The lower solar atmosphere of the Sun can be modeled considering data from observations and by a static boundary conditions with spherical symmetry. Figure 1.2 shows the mean variation of temperature and density of the solar atmosphere according to the model Vernazza-Avrett-Loeset (VAL-C) by Vernazza et al. (1981). This is a semi-empirical one-dimensional model obtained by solving the non-LTE radiative transfer equations with statistical and hydrostatic equilibrium. The model fits the results obtained from a number of observed spectral lines formed in different regions in the solar atmosphere. However, 1D models are too simplistic due to the three-dimensional complexity of the magnetic field topology and the dynamic of the solar atmosphere seen in observations, being both observables driven by convective motions. This produces a connexion between different phenomena, and makes coupling throughout the atmosphere. Figure 1.5 schematically summarizes this complexity for the quiet Sun by merging information acquired from observations and numerical simulations.

The quiet Sun is a very dynamic region where the granulation pattern is formed due to convective overshoot. It covers at least 90% of the solar surface and has an important amount of magnetic flux as Trujillo Bueno et al. (2004) had shown using spectropolarimetric data and the Hanle effect. The quiet

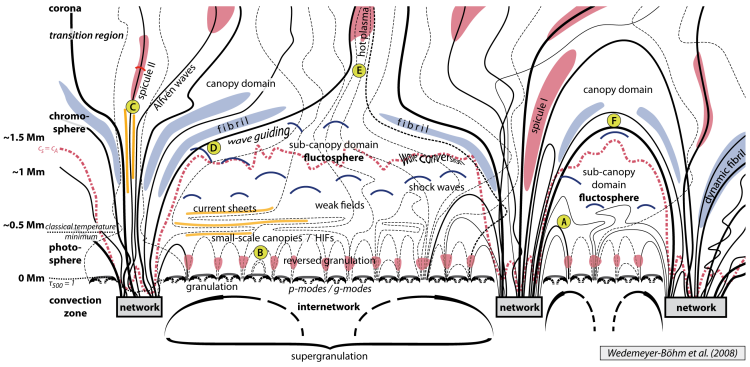

FIGURE 1.5— Simplified schematic structure of the lower quiet Sun atmosphere, not drawn to scale. Extracted from Wedemeyer-Böhm et al. (2009).

Sun is constituted at large scale by a pattern of super-granule cells, where the magnetic field is slowly advected and concentrated to the supergranulation inter lanes by the large scale convective motions. Patches of magnetic field called *magnetic network* are formed this way. The magnetic field strength of the magnetic network can reach values of kG, the typical size of super-granules is 12–50 Mm, and their typical lifetime is 20–50h (DeRosa & Toomre 2004).

The space between the magnetic network is called internetwork and it contains almost magnetically unperturbed granulation. Granules are driven by the convective motion and overshooting. They interact with small scale weak magnetic fields in the quiet Sun. Granules are the bright center of small cell where hot material is ascending and spreads out and cools at the surface, and then sink through the dark intergranular lanes while it warms up and compresses. This cell pattern have a diameter of the order of 1 Mm and a lifetime of about 20 minutes. Convective turbulent motions in the convection zone stochastically excite waves. These waves are turned into p-modes, and travel through the Sun interior while being refracted and reflected at the surface. In the upper atmospheric layers, waves can also be transformed due to the magnetic field.

The magnetic field anchored to the photospheric network expanses with height over the internetwork, enclosing its weak magnetic field in a structure similar to a roof called *magnetic canopy*. The topology and height of this canopy change dynamically and not only in time but space. Magnetic elements are also located in the internetwork region, see mark A in Fig. 1.5 (Schrijver & Title 2003).

A small-scale canopy forms over the granules known as horizontal internetwork fields (HIFs), see the mark B in Figure 1.5. This structure appears due to the slow advection motion to the intergranular lanes of the emergent weak magnetic field due to convection and is probably generated by a small-scale local dynamo (Schüssler & Vögler 2008). Above the HIFs and around the classical minimum temperature height ($\approx$ 0.5 Mm) horizontal current sheets can appear. The region above the HIFs can be considered as the bottom boundary of a chromospheric region dominated by shock waves and it is referred as *clapotisphere* by Rutten (1995, 2007) or *fluctosphere* by Wedemeyer-Böhm & Wöger (2007). These shocks shuffle and entangle dynamically the magnetic field and, as a consequence, the

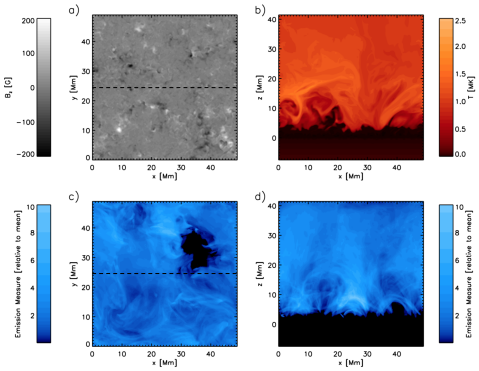

FIGURE 1.6— Snapshot of the quiet Sun setup from numerical simulations by Rempel (2017). Panels a) and c) are horizontal view of the vertical magnetic field at 700 km above photosphere and the emission measure respectively. Panels b) and d) are the vertical cut along the dashed line in panels a) and c). This setup correspond to a quiet Sun configuration with vertical zero net flux an a mixed polarity field originated from a small scale dynamo. The peak of the magnetic heating in the lower corona is located around 5–10 Mm.

region where the sound speed equals the Alfvén speed, the *equipartition layer*, changes dynamically as is sketched by the red dotted line in Fig. 1.5. This results in a set of regions with low and high plasma-β instead of a closed surface, as it was shown by Schrijver & van Ballegooijen (2005) using numerical simulations.

The most recognizable feature of the chromosphere, at least when observing the solar limb, are the *spicules*, see Figure 1.8. Base on observations, it is possible to distinguish two kinds of them. Spicules of type I, associated to shock waves, are coming from the photosphere propagating along magnetic field lines anchored to the photosphere, and are extended into the upper layers. Spicules of type II are generated by magnetic reconnection, they are more dynamic, thinner, and show a higher velocity than spicules of type I, see mark C. They show a shorter lifetime than the type I in chromospheric lines such as Ca II, but in upper chromosphere lines (e.g., Mg II) or TR lines (e.g. Si IV or He II), show longer lifetime, this is due to heating associated to the spicules (Pereira et al. 2014; Skogsrud et al. 2016). Alfvénic waves can be found everywhere in the chromosphere associated to both types of spicules (De Pontieu et al. 2004, 2007a,b; Hansteen et al. 2006; Rouppe van der Voort et al. 2007; Langangen et al. 2008). It is around the equipartition layer were the wave mode transformation can occur (Cally 2006, 2007). In this scenario, some waves and shocks can be guided by the magnetic field lines upward (mark D), compressing and heating chromospheric plasma in channels (mark E) or in closed loops (mark F).

Understanding the connection between solar atmospheric layers through the magnetic field is a challenging task in solar physics. The atmospheric regions are constituted by partially ionized plasma with a low ionization fraction. It is known that partial ionization plays an important role in the chromosphere (Martínez-Sykora et al. 2012; Khomenko et al. 2014; Ballester et al. 2018). For modeling the behavior of plasmas the equations of magnetohydrodynamics (MHD) are useful tool. Combining the moments of the Boltzmann equation for each plasma component together with Maxwell's equations, as is briefly described in Chapter 2, it is possible to derive the set of MHD equations. The solar atmosphere is frequently modeled via MHD approximation. This model is valid for cases with a strongly coupled collisional media and has been an excellent tool to understand the physical interaction between the magnetic field and the plasma in the solar atmosphere. MHD allows easily to include an

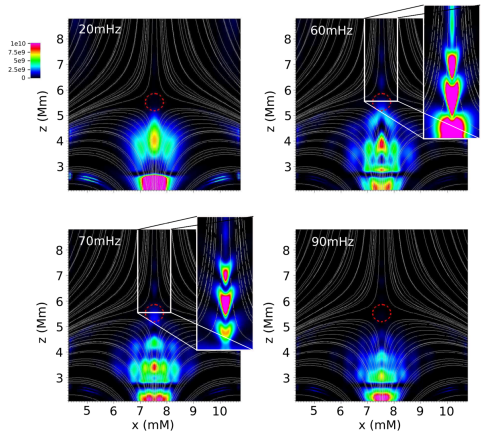

FIGURE 1.7— Spatial distribution of waves around a coronal null point for four selected frequencies. The interaction of fast magneto-acoustic waves with the null point generates a pressure driven slow magneto-acoustic train wave where the null point acts as a resonator for certain frequencies of waves channeled outward along the separatrix. The frequency distribution depends of the atmospheric properties. Extracted from Santamaria & Van Doorsselaere (2018).

important number of physical effects such as radiative transfer, heat conduction along magnetic field lines or hydrogen time-dependent ionization. MHD has been successfully used to model a number of phenomena (e.g., Asplund et al. 2000; Schaffenberger et al. 2005; Vögler et al. 2005; Stein & Nordlund 2006; Khomenko & Collados 2006; Nordlund et al. 2009; Rempel 2017; Santamaria & Van Doorsselaere 2018). However, under the conditions of the solar high photosphere or the chromosphere this coupling becomes weak and the MHD formalism is not valid any more.

The presence of neutrals together with the weakening of collisional coupling due to that the density fall off with height leads to the invalidation of the assumptions underpinning the ideal MHD approach and produces a series of non-ideal effects. These non-ideal effects are the ambipolar diffusion and the Hall effect (modified by collisions with neutrals). They can be described by a series of extra terms in the generalized induction equation and in the energy conservation equation under the non-ideal MHD formalism, together with the Ohmic diffusion and the Biermann battery effect, as we will see in the following chapters of this thesis. These non-ideal effects have been actively studied during recent years in the Sun by several authors (e.g., Kumar & Roberts 2003; Khodachenko et al. 2004; Forteza et al. 2007; Pandey & Wardle 2008; Vranjes et al. 2008; Soler et al. 2009, 2010; Zaqarashvili et al. 2011; Khomenko & Collados 2012; Martínez-Sykora et al. 2012; Leake et al. 2014; Shelyag et al. 2016; Martínez-Sykora et al. 2017, 2018; Khomenko et al. 2017, 2018; Nóbrega-Siverio et al. 2016, 2017, 2018). A recent review can be found in Ballester et al. (2018).

Aim and outline of this work

As it was mentioned before, understanding the connection between solar atmospheric layers through the magnetic field is a challenging task in solar physics. To push forward our knowledge in this direction, and try to answer some questions, the work presented here follows the realistic modeling initiated by Khomenko et al. (2017) using the Biermann battery term to seed the quiet Sun magnetic field and later on extended by Khomenko et al. (2018) adding the ambipolar diffusion. The main goal

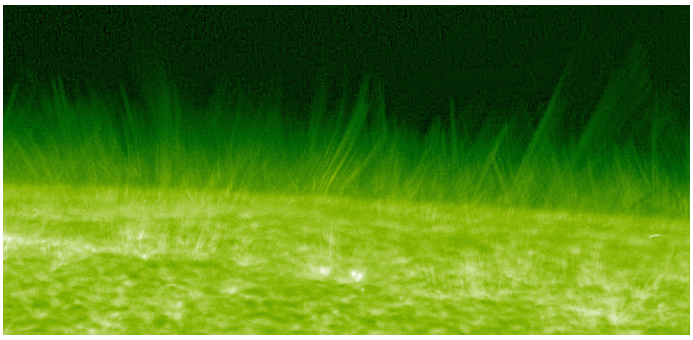

FIGURE 1.8— Solar spicules observed at the solar limb with the Solar Optical Telescope (SOT) onboard of Hinode spacecraft. The used wavelength correspond to calcium H line (396nm). Image credit: NAOJ/JAXA.

of this PhD project is to understand how the non-ideal effects associated to the partial ionization of the solar atmospheric plasma modify the energy distribution of thermal and magnetic structures in quiet Sun regions. We continue those studies by adding the Hall effect, allowing then a full coupling between fast and slow magneto-acoustic modes and as a consequence the coupling of the fast mode to the Alfvén mode through the Hall current.

To achieve this, Chapter 2 starts by introducing the non-ideal MHD formalism and some concepts which are going to be needed along this thesis. Next, in Chapter 3 a in depth description of the code MANCHA3D, used along this work, is done. In Chapter 4 a new numerical scheme (MHDSTS) is introduced since, under the non-ideal MHD single-fluid formalism, when ambipolar diffusion or Hall effect dominate, it can introduce severe restrictions not only on the integration time step but also it can compromise the stability of the traditional Runge-Kutta numerical scheme. This numerical scheme is formed by blocks, the first of them is known as super time-stepping (STS) and it is designed to overcome the limitations imposed when the ambipolar diffusion term is dominant. The second block is called the Hall diffusion scheme (HDS) and it is used when the Hall term becomes dominant. These two numerical techniques can be used together by applying the Strang operator splitting technique.

With the code ready, an extension of the study done by Cally & Khomenko (2015) about the coupling between fast magneto-acoustic and Alfvén waves is done in the Chapter 5. This coupling can be observe in fully ionized plasmas mediated by stratification and 3D geometrical effects. However, Cally & Khomenko (2015) under the approximation of cold plasma, have shown that in a weakly ionized plasma, such as the solar photosphere and chromosphere, the Hall current introduces a new coupling mechanism. This chapter extends their study to the case of warm plasma using a quasi-realistic stratification in thermodynamic parameters resembling the solar atmosphere.

Finally, in Chapter 6, a step beyond the state of the art of solar local dynamo simulation is taken. From the numerical experiments done by Khomenko et al. (2018) it is know that ambipolar diffusion allows to dissipate incompressible perturbations associated to magnetic waves removing the magnetic Poynting flux and converting the magnetic energy into the thermal energy. Chapter 6 goes further by presenting realistic three-dimensional simulations of solar dynamo where the Hall effect is also considered. The simulations have a magnetic field which is seeded by the battery effect and then amplified to solar values by the local dynamo. Once the system is stable, two new branches are gener-

ated by switching on/off the ambipolar diffusion and the Hall effect obtaining in total three branches which are compared statistically. The action of all three effects can be considered as an attractive mechanism of energy generation, transport, and chromospheric heating. Hall term introduces a new fast-to-Alfvén mode transformation mechanism to obtain Alfvén waves which could travel to upper layers and generates currents which could be dissipated by the ambipolar diffusion closing the cycle and helping to the atmospheric heating.

Summary

- ⊙ MANCHA3D code is extended and modified to overcame the limitations imposed by the non-ideal terms which appear into the MHD equations when partial ionization effects are considered. Using the Strang splitting technique the STS and HDS numerical schemes were added to the ideal MHD operator. Several test are presented to compare the numerical and analytical solutions.
- ⊙ Fast-to-Alfvén mode transformation analytical study on cold plasmas is extended by means of numerical simulations of warm plasmas allowing thus the complete process of coupling between fast and slow magneto-acoustic modes and subsequent coupling of the fast mode to the Alfvén mode through the Hall current.
- ⊙ Three-dimensional numerical experiments of solar local dynamo with a magnetic field seeded by the action of the Biermann battery effect and amplified by the local dynamo are done to investigate the non-ideal effects which arise due to the presence of neutrals in the atmosphere. Ambipolar diffusion and Hall effects are taken into account. Time evolution and statistical properties of different parameter were compared and analyzed statically to reveal the consequences of taking into account separately some of those non-ideal effects or considering them all together.

2

Theoretical Concepts

In general, we look for a new law by the following process. First, we guess it. [...] Then we compute the consequences of the guess, to see what, if this is right, if this law we guess is right, to see what it would imply and then we compare the computation results to nature, or we say compare to experiment or experience, compare it directly with observations to see if it works.

- Richard P. Feynman lecture, 1960s

In this chapter, theoretical concepts employed during this work are described. The multi-fluid description is introduced in Section 2.1 to derive the single-fluid description for a plasma with non-ideal effects of Section 2.2. The physical meaning of the non-ideal terms is discussed in Subsection 2.2.1. Section 2.3 introduces the concepts of MHD waves and mode conversion needed in Chapters 5 and 6.

2.1 Multi-fluid description

A plasma system is composed in general by a very large number of particles interacting between them. The dynamic state of each particle at a given time can be described by its position $\mathbf{r}$ and velocity $\mathbf{u}$ vectors. This vectors form a six-dimensional space or phase space, often called μ-space. Some of those particles could have internal degrees of freedom such as the chemical specie (α), ionization degree (I), or excitation level (E). We can consider the many-particle phase state or Γ-space for the whole system of particles. Those internal degrees of freedom correspond to a single micro-state $a = \{\alpha \mathrm{IE}\}$. Following Bittencourt (2004) and considering the coordinates $\mathbf{r}$ and $\mathbf{u}$ independent variables, we can define the distribution function in phase space $f_a(\mathbf{r}, \mathbf{u}, t)$ as the density of points corresponding to the particles in a micro-state a.

$$f_a(\mathbf{r}, \mathbf{u}, t) = \frac{d^6 N_a(\mathbf{r}, \mathbf{u}, t)}{d^3 r d^3 u} \,, \tag{2.1}$$

where $d^6 N_a(\mathbf{r}, \mathbf{u}, t)$ is the number of particles in the micro-state a inside an element of volume $d^3 r d^3 u$ around the point $(\mathbf{r}, \mathbf{u})$ at a given time t. Using the mass conservation principle, the average number of particles of element α satisfy:

$$n_\alpha = \sum_{\mathrm{I}} n_{\alpha \mathrm{I}} = \sum_{\mathrm{I,E}} n_{\alpha \mathrm{IE}} \,. \tag{2.2}$$

The ionization stage I generally indicates the number of electrons in the system thus $\mathrm{I} = 0$ represents neutrals. For electrons the notation of the micro-state can be simplified with the subscript e, for

neutrals with an n, and for ions with an i. Considering charge neutrality, we request that the number of electrons be equal to

$$n_e = \sum_{\alpha,\mathrm{I}} \mathrm{I} \cdot n_{\alpha \mathrm{I}} \, . \tag{2.3}$$

At this point we assume that our plasma is coupled enough by collisions to apply the fluid approximation and therefore it is possible to describe the plasma using the transport equations derived from the Boltzmann equation

$$\frac{\partial f_a}{\partial t} + \mathbf{u} \cdot \nabla f_a + \mathbf{a} \cdot \nabla_u f_a = \left(\frac{\partial f_a}{\partial t} \right)_{\mathrm{coll}} \, , \tag{2.4}$$

where f_a is the distribution function of particles in the micro-state a, $\mathbf{u}$ is the particle velocity, and $\mathbf{a}$ its acceleration. This equation, from left to right, is telling us that the number of particles inside a unit volume of the phase space changes in time due to particles entering or leaving this volume across its boundary, or because external forces are accelerating the particles, or finally because there are collisions with other particles during the time interval dt. This collision term describes either elastic or inelastic collisions, and introduces a challenge in solving the equation due to its complexity, for it may include momentum exchange, chemical or nuclear reactions, or ionization-recombination process among others. Because it must satisfy the conditions of conservation of the particles number, momentum, and energy, some approximations can be done to derive this term.

To obtain the transport equations for a scalar magnitude $\chi(\mathbf{u})$, we multiply the Boltzmann equation (2.4) by this quantity and then we integrate the resulting equation over the velocity space. The velocity of each particle is defined as the center mass velocity plus a random velocity

$$\mathbf{u} = \mathbf{u}_a + \mathbf{c}_a \, . \tag{2.5}$$

Choosing for χ the mass m_a, we get the equation of continuity or conservation of mass

$$\frac{\partial \rho_a}{\partial t} + \nabla \cdot (\rho_a \mathbf{u}_a) = S_a \, , \tag{2.6}$$

selecting χ as the momentum $m_a \mathbf{u}$, we obtain the equation of motion or conservation of momentum

$$\frac{\partial \rho_a \mathbf{u}_a}{\partial t} + \nabla \cdot (\rho_a \mathbf{u}_a \mathbf{u}_a + \hat{\mathbf{p}}_a) = \rho_a r_a (\mathbf{E} + \mathbf{u}_a \times \mathbf{B}) + \rho_a \mathbf{g} + \mathbf{R}_a \, , \tag{2.7}$$

where the notation $\mathbf{u}_a \mathbf{u}_a \equiv \mathbf{u}_a \otimes \mathbf{u}_a$ will represent the dyadic or tensor product of two vectors along this work. Selecting χ as the kinetic energy plus the potential energy of excitation-ionization $m_a u_a^2/2 + E_a$, we obtain the equation of energy transport or conservation of energy

$$\frac{\partial}{\partial t} \left(\epsilon_a + \frac{\rho_a u_a^2}{2} \right) + \nabla \cdot \left(\mathbf{u}_a \left[\epsilon_a + \frac{\rho_a u_a^2}{2} \right] + \hat{\mathbf{p}}_a \mathbf{u}_a + \mathbf{Q}_a \right) = M_a + \frac{E_a}{m_a} S_a + \rho_a \mathbf{u}_a \cdot \mathbf{g} + \rho_a r_a \mathbf{u}_a \cdot \mathbf{E} \, , \tag{2.8}$$

where ρ_a is the mass density, $\mathbf{u}_a$ is the center of mass velocity, $\hat{\mathbf{p}}_a$ is the pressure tensor, ϵ_a is the internal energy density, $\mathbf{Q}_a$ is the heat flow vector, $\mathbf{g}$ is the gravity acceleration vector, $\mathbf{E}$ is the electric field vector, $\mathbf{B}$ is the magnetic field vector and $r_a = q_a/m_a$ is the charge over mass ratio. The effect of the collisions are collected in a new set of terms on the right-hand side. These terms cover the loss or gain of mass S_a, momentum $\mathbf{R}_a$, and energy M_a.

The definition of the tensor and scalar pressure, the heat flow vector and internal energy will be done through the random velocities c_a as

$$\hat{\mathbf{p}}_a = \rho_a \langle \mathbf{c}_a \mathbf{c}_a \rangle \, ; \quad p_a = \frac{1}{3} \rho_a \langle c_a^2 \rangle \, ; \quad \mathbf{Q}_a = \frac{1}{2} \rho_a \langle c_a^2 \mathbf{c}_a \rangle \, , \tag{2.9}$$

$$\epsilon_a = \frac{1}{2}\rho_a \langle c_a^2 \rangle + n_a E_a = \frac{3}{2} p_a + n_a E_a \, . \tag{2.10}$$

For photons, since they do not have mass at rest and there is no relativistic effects involved in our system, there is no force acting on them. In this case, after some manipulation the energy equation takes the standard form of the radiative transfer equation (Mihalas 1978; Khomenko et al. 2014):

$$\frac{dI_\nu}{ds} = j_\nu - k_\nu I_\nu \, . \tag{2.11}$$

which describe the behavior of the radiation intensity I_ν along the direction of the ray s when photons of a fixed frequency ν are traveling through a medium absorbing (k_ν) or emitting (j_ν) photons.

The set of equations (2.6), (2.7), and (2.8), derived from the Boltzmann equation, can be simplified into the so called two-fluid formalism by neglecting the electron inertia compared to the typical ion inertia. The details of this process is show by Khomenko et al. (2014). When the collisions are strongly dominant over all other forces, the collision frequency results larger than any cyclotron frequency associated to the particles. Under this situation, the momentum transfer between particles becomes very efficient and then, the differences in velocities or energy between different kinds of particles will be very small. Therefore each set of equations associated to each kind of particles gives redundant information and it is possible to sum up all the equations for different micro-states leading to the so called single-fluid formalism. This formalism will be explain in more detail in the next subsection. Notice that both formalisms are avoiding to solve the transport equations for electrons therefore we are loosing information about the electric field which has to be supplied by adding the generalized Ohm's law.

2.1.1 Single-fluid description

For a single-fluid description, we assume that the collisional coupling is strong enough and that the plasma is form by $2N+1$ components; N neutrals, N ions, and one electron. Then the definitions for the macroscopic variables will be

- Total mass density:

$$\rho = \sum_{a=1}^{2N+1} n_a m_a = \rho_n + \rho_i + \rho_e \tag{2.12}$$

- Center of mass velocity:

$$\mathbf{v} = \frac{1}{\rho} \sum_{a=1}^{2N+1} \rho_a \mathbf{u}_a = \frac{1}{\rho} \left(\rho_n \mathbf{u}_n + \rho_i \mathbf{u}_i + \rho_e \mathbf{u}_e \right) \tag{2.13}$$

- Drift velocity respect to the average center of mass $\mathbf{v}$ for each species:

$$\mathbf{w}_a = \mathbf{u}_a - \mathbf{v} \tag{2.14}$$

- Total current density, summing only over ions:

$$\mathbf{J} = q_e \sum_{a=1}^{N} (n_a \mathbf{u}_a) + q_e n_e \mathbf{u}_e \tag{2.15}$$

⊙ Total kinetic pressure tensor:

$$\hat{\mathbf{p}} = \sum_{a=1}^{2N+1} \hat{p}_a + \sum_{a=1}^{2N+1} \rho_a \mathbf{w}_a \mathbf{w}_a \tag{2.16}$$

⊙ Total pressure scalar:

$$p = \sum_{a=1}^{2N+1} p_a + \frac{1}{3} \sum_{a=1}^{2N+1} \rho_a \mathrm{w}_a^2 \tag{2.17}$$

⊙ Total heat flow vector:

$$\mathbf{Q} = \sum_{a=1}^{2N+1} \left(\mathbf{Q}_a + \hat{\mathbf{p}}_a \mathbf{w}_a + \frac{3}{2} p_a \mathbf{w}_a + \frac{1}{2} \rho_a \mathrm{w}_a^2 \mathbf{w}_a \right) \tag{2.18}$$

⊙ Total heat flux vector corrected for potential ionization - recombination energy flux (χ_a):

$$\mathbf{Q}' = \mathbf{Q} + \sum_{a=1}^{2N} \chi_a \mathbf{w}_a \tag{2.19}$$

Summing up the Equations (2.6), (2.7), and (2.8) over all the species we get a quasi-MHD set of equations which includes non-ideal terms. Those terms (loss or gain of mass, momentum, and energy) do not appear into the ideal MHD formalism.

$$\frac{\partial \rho}{\partial t} + \nabla \cdot (\rho \mathbf{v}) = 0 \,, \tag{2.20}$$

$$\frac{\partial \rho \mathbf{v}}{\partial t} = \nabla \cdot (\rho \mathbf{v}\mathbf{v} + \hat{\mathbf{p}}) = \mathbf{J} \times \mathbf{B} + \rho \mathbf{g} \,, \tag{2.21}$$

$$\frac{\partial}{\partial t} \left(\epsilon + \frac{\rho \mathbf{v}^2}{2} \right) + \nabla \cdot \left(\mathbf{v} \left[\epsilon + \frac{\rho \mathbf{v}^2}{2} \right] + \hat{\mathbf{p}} \mathbf{v} + \mathbf{Q} + \mathbf{F}_R \right) = \mathbf{J} \cdot \mathbf{E} + \rho \mathbf{v} \cdot \mathbf{g} \,, \tag{2.22}$$

where $\mathbf{F}_R$ is the integrated radiative energy flux over all directions ($d\Omega$) and frequencies (ν).

$$\mathbf{F}_R(\mathbf{r}, t) = \int_0^\infty \oint \mathbf{n} I_\nu(\mathbf{r}, \mathbf{n}, \nu, t) d\Omega \mathrm{d}\nu \,. \tag{2.23}$$

Collisional terms vanish from the equations since the collisional forces compensate each other.

2.1.2 Generalized Ohm's law

The missing piece in equation (2.22), the electric field of the Joule term $\mathbf{J} \cdot \mathbf{E}$, can be calculated through the generalized Ohm's law. This generalized Ohm's law can be obtained after multiplying the ion motion equation by $r_{\alpha \mathrm{I}}$ and adding them up, see Bittencourt (2004).

$$\begin{aligned} \sum_{\alpha,\mathrm{I}\neq 0}^{N+1} \rho_{\alpha \mathrm{I}} r_{\alpha \mathrm{I}}^2 (\mathbf{E} + \mathbf{u}_{\alpha \mathrm{I}} \times \mathbf{B}) = \frac{\partial \mathbf{J}}{\partial t} + \nabla \cdot (\mathbf{J}\mathbf{u}_c + \mathbf{u}_c \mathbf{J}) + \nabla \cdot \sum_{\alpha,\mathrm{I}\neq 0}^{N+1} \rho_{\alpha \mathrm{I}} r_{\alpha \mathrm{I}} \mathbf{w}_{\alpha \mathrm{I}} \mathbf{w}_{\alpha \mathrm{I}} + \\ + \sum_{\alpha,\mathrm{I}\neq 0}^{N+1} r_{\alpha \mathrm{I}} \nabla \cdot \hat{\mathbf{p}}_{\alpha \mathrm{I}} - \sum_{\alpha,\mathrm{I}\neq 0}^{N+1} r_{\alpha \mathrm{I}} \mathbf{R}_{\alpha \mathrm{I}} \,, \end{aligned} \tag{2.24}$$

where the current density is defined as

$$\mathbf{J} = \sum_{\alpha,\mathrm{I}\neq 0}^{N+1} \rho_{\alpha\mathrm{I}} r_{\alpha\mathrm{I}} \mathbf{u}_{\alpha\mathrm{I}} \,, \tag{2.25}$$

with $\mathbf{u}_{\alpha\mathrm{I}}$ the velocity individual particles, $\mathbf{u}_c$ the center mass velocity of all charged species, and $\mathbf{w}_{\alpha\mathrm{I}} = \mathbf{u}_{\alpha\mathrm{I}} - \mathbf{u}_c$ the drift velocity of the species. In this case, the summation in the Equation (2.25) contains the charge of the particles, therefore only velocities of ionized particles are taken into account. The only assumption made to obtain this expression was the charge neutrality.
This expression as it is has no practical use for us since it is giving the same information as the momentum equation for ions, but there are several approximations that can be done, especially for the solar atmosphere case.

Solar atmosphere

For a plasma where the currents vary slowly in time compared to hydrodynamical processes, it is reasonable to assume that the currents are stationary and then, it is safe to neglect the term

$$\frac{\partial \mathbf{J}}{\partial t} + \nabla \cdot (\mathbf{J}\mathbf{u}_c + \mathbf{u}_c\mathbf{J}) \approx 0 \,, \tag{2.26}$$

in Eq. (2.24).
The velocities drifts of individual species respect to the charge velocity ($\mathbf{w}_{\alpha\mathrm{I}}$) are expected to be small for a plasma near the equilibrium and as a result, the second order terms in velocity drifts can be neglected as well,

$$\nabla \cdot \sum_{\alpha,\mathrm{I}\neq 0}^{N+1} \rho_{\alpha\mathrm{I}} r_{\alpha\mathrm{I}} \mathbf{w}_{\alpha\mathrm{I}} \mathbf{w}_{\alpha\mathrm{I}} \approx 0 \,. \tag{2.27}$$

It is also reasonable to assume that singly ionized ions are the dominant in the regions of the atmosphere where we want to apply these equations (chromosphere). The collision term can be then approximated as

$$\sum_{\alpha,\mathrm{I}\neq 0}^{N} r_{\alpha\mathrm{I}} \mathbf{R}_{\alpha\mathrm{I}} \approx -\mathbf{J} \left(\sum_{\alpha,\mathrm{I}=1}^{N} \nu_{e;\alpha\mathrm{I}} + \sum_{b}^{N} \nu_{e;b0} \right) + e n_e (\mathbf{u}_c - \mathbf{u}_n) \left(\sum_{b}^{N} \nu_{e;b0} - \sum_{\alpha,\mathrm{I}=1}^{N} \sum_{b}^{N} \nu_{\alpha\mathrm{I};b0} \right) \,, \tag{2.28}$$

after considering that the coefficient containing the atomic mass of the colliding ions of type α and neutrals of type β, $A_{\alpha\beta}^{-1/2} = \sqrt{(A_\alpha + A_\beta)/(A_\alpha A_\beta)}$, have a very little variation. This can be done since, for the solar case, the abundance of heavy atoms and their probability of collision are small in comparison to the lightest atoms. The term $\sum_\alpha (n_{\alpha\mathrm{I}}/n_e)\mathbf{w}_{\alpha\mathrm{I}}$ can be also neglected since sum of the drift velocities ($\mathbf{w}_{\alpha\mathrm{I}}$) is expected to be small (Khomenko et al. 2014). The approximation of taking only singly ionized ions is reasonable, since in the temperature range of interest, where partially ionized plasma exists, the abundance of multiply ionized ions is negligible. With this, the equation (2.24) can be written as:

$$\mathbf{E} + \mathbf{u}_c \times \mathbf{B} = \eta\mu_0 \mathbf{J} + \eta_H \mu_0 \frac{(\mathbf{J} \times \mathbf{B})}{|B|} - \eta_B \mu_0 \frac{\nabla \cdot \hat{\mathbf{p}}_e}{|B|} - \chi\mu_0 (\mathbf{u}_c - \mathbf{u}_n) \,, \tag{2.29}$$

where η is the Ohmic diffusivity

$$\eta = \frac{\rho_e}{e^2 n_e^2 \mu_0} \left(\sum_{\alpha,\mathrm{I}=1}^{N} \nu_{e;\alpha\mathrm{I}} + \sum_{b}^{N} \nu_{e;b0} \right) \,, \tag{2.30}$$

η_H and η_B are the Hall and Biermann battery coefficients respectively,

$$\eta_H = \eta_B = \frac{|\mathbf{B}|}{e n_e \mu_0} \,, \tag{2.31}$$

and the coefficient χ is define as

$$\chi = \frac{m_e}{e\mu_0}\left(\sum_b^N \nu_{e;b0} - \sum_{\alpha,\mathrm{I}=1}^N \sum_b^N \nu_{\alpha\mathrm{I};b0}\right) \,. \tag{2.32}$$

For a single-fluid case, it is useful to write the Ohm's law in term of the center of mass velocity of the whole plasma

$$\mathbf{E} + \mathbf{v}\times\mathbf{B} = \mathbf{E} + \mathbf{u}_c \times \mathbf{B} - \xi_n \mathbf{w}\times\mathbf{B} \,, \tag{2.33}$$

where $\xi_n = \rho_n/\rho$ is the neutral fraction. Following Braginskii (1965), we obtain the expression for the relative velocity between ions and neutrals,

$$\mathbf{w} = \mathbf{u}_c - \mathbf{u}_n \approx \frac{\xi_n}{\alpha_n}(\mathbf{J}\times\mathbf{B}) - \frac{\mathbf{G}}{\alpha_n} + \sum_b^N \rho_e \nu_{e;b0} \frac{\mathbf{J}}{e n_e \alpha_n} \,, \tag{2.34}$$

where the collisional parameter is defined as

$$\alpha_n = \sum_b^N \rho_e \nu_{e;b0} + \sum_{\alpha,\mathrm{I}=1}^N \sum_b^N \rho_{\alpha\mathrm{I}} \nu_{\alpha\mathrm{I};b0} \,, \tag{2.35}$$

and the pressure term is

$$\mathbf{G} = \xi_n \nabla\cdot\hat{\mathbf{p}}_c - \xi_i \nabla\cdot\hat{\mathbf{p}}_n \,, \tag{2.36}$$

where $\hat{\mathbf{p}}_c$ and $\hat{\mathbf{p}}_n$ are the tensor pressure for charges and neutrals respectively and $\xi_i = \rho_i/\rho$ is the ion fraction. This allow us to write the expression (2.29) as

$$\mathbf{E}^* = \mathbf{E} + \mathbf{v}\times\mathbf{B} = \eta_0\mu_0\mathbf{J} - \eta_A\mu_0\frac{[(\mathbf{J}\times\mathbf{B})\times\mathbf{B}]}{|B|^2} + \eta_H\mu_0\frac{(\mathbf{J}\times\mathbf{B})}{|B|} - \eta_B\mu_0\frac{\nabla\cdot\hat{\mathbf{p}}_e}{|B|} + \eta_p\mu_0\frac{(\mathbf{G}\times\mathbf{B})}{|B|^2} \,. \tag{2.37}$$

The second term on the right-hand side is the ambipolar diffusion term and it appears after the change of reference system, Eq. (2.33). The last term is related to the partial pressure gradients and in general it is small compared to the other terms, which is why it is usually neglected. The ambipolar diffusion coefficient is defined as

$$\eta_A = \frac{\xi_n^2 |\mathbf{B}|^2}{\alpha_n \mu_0} \,, \tag{2.38}$$

and the partial pressure gradient coefficient as

$$\eta_p = \frac{\xi_n |\mathbf{B}|^2}{\alpha_n \mu_0} \,. \tag{2.39}$$

2.2 Single-fluid MHD equations

With the ingredients presented in the section above we are ready to write the non-ideal single-fluid MHD system of equations for a single-fluid multicomponent plasma (N ions, N neutrals and one electron component) where the non-ideal effects due to the collisions will be encoded into several terms in the induction and total energy conservation equations. From the set of equation (2.20), (2.21), and

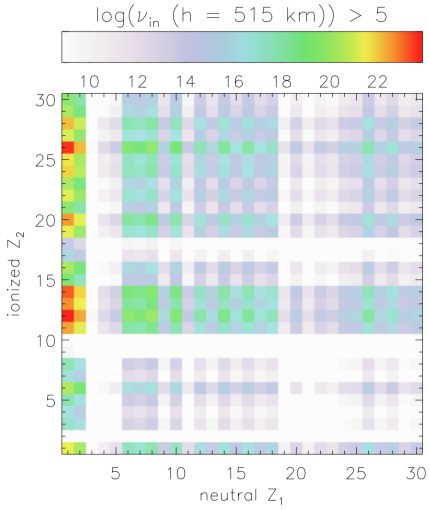

FIGURE 2.1— Collisional frequency map computed according to a classical model using Eqs. (2.48) and (2.48). The atmospheric model used is VAL-C and the height is 515 km. The abscissa is the atomic number of the first colliding particle and ordinates the atomic number of the second colliding particle. The most frequent collisions occurs between H and He and other ions (first two columns). Extracted from Khomenko et al. (2014).

(2.22) and using the generalized Ohm's equation (2.37) we get the continuity equation as

$$\frac{\partial \rho}{\partial t} + \nabla \cdot (\rho \mathbf{v}) = 0 \,, \tag{2.40}$$

the momentum conservation equation, after using the Ampère's law, as

$$\frac{\partial (\rho \mathbf{v})}{\partial t} + \nabla \cdot \left[\rho \mathbf{v}\mathbf{v} + \left(p + \frac{\mathbf{B}^2}{2\mu_0} \right) \mathbf{I} - \frac{\mathbf{B}\mathbf{B}}{\mu_0} \right] = \rho \mathbf{g} \,, \tag{2.41}$$

and the induction equation in the total plasma frame system as

$$\frac{\partial \mathbf{B}}{\partial t} = \nabla \times \left[(\mathbf{v} \times \mathbf{B}) - \eta \mu_0 \mathbf{J} - \eta_H \frac{\mu_0}{|B|} (\mathbf{J} \times \mathbf{B}) + \eta_A \frac{\mu_0}{|B|^2} [(\mathbf{J} \times \mathbf{B}) \times \mathbf{B}] + \eta_B \frac{\mu_0}{|B|} \nabla p_e \right] , \tag{2.42}$$

where we retained the convective, Ohmic, Hall, ambipolar, and Biermann battery terms and neglected the pressure related term on the right-hand side of Equation (2.37). The coefficients multiplying these terms are, respectively, the Ohmic (η), Hall (η_H), ambipolar (η_A), and battery (η_B) coefficients, and all have the same units of diffusivity ($l^2 t^{-1}$, i.e. $m^2 s^{-1}$ in SI). Those coefficients are defined by Equations (2.30), (2.31), and (2.38). The total energy conservation equation

$$\begin{aligned} \frac{\partial e}{\partial t} + \nabla \cdot \left[\mathbf{v} \left(e + p + \frac{|\mathbf{B}|^2}{2\mu_0} \right) - \frac{\mathbf{B}(\mathbf{v} \cdot \mathbf{B})}{\mu_0} \right] &= \rho \mathbf{v} \cdot \mathbf{g} + \\ + \nabla \cdot [\mathbf{B} \times (\eta + \eta_A) \mathbf{J}_\perp] + \nabla \cdot \left[\eta_B \frac{\nabla p_e \times \mathbf{B}}{|B|} \right] + Q_{\rm rad} \,, \end{aligned} \tag{2.43}$$

is written in terms of the total energy density per volume unit e, which is the sum of the kinetic, internal and magnetic energies,

$$e = \frac{1}{2}\rho \mathbf{v}^2 + \epsilon + \frac{\mathbf{B}^2}{2\mu_0} \,, \tag{2.44}$$

The electric current is defined as

$$\mu_0 \mathbf{J} = \nabla \times \mathbf{B} \,, \tag{2.45}$$

and the current perpendicular to the field lines,

$$\mathbf{J}_\perp = -\frac{(\mathbf{J} \times \mathbf{B}) \times \mathbf{B}}{|B|^2} \,, \tag{2.46}$$

and Gauss's law for magnetism is

$$\nabla \cdot \mathbf{B} = 0 \,. \tag{2.47}$$

To close the system, the equation of state is used.

The expressions for the collisional frequencies between ions and neutrals (ν_{in}) and electrons with neutrals (ν_{en}) are taken from Spitzer (1956). For the collisions between electrons and ions (ν_{ei}) we use the expressions from Braginskii (1965)

$$\nu_{in} = n_n \sqrt{\frac{8 k_B T}{\pi m_{in}}} \sigma_{in} \,, \tag{2.48}$$

$$\nu_{en} = n_n \sqrt{\frac{8 k_B T}{\pi m_{en}}} \sigma_{en} \,, \tag{2.49}$$

$$\nu_{ei} = \frac{n_e e^4 \ln \Lambda}{3 \epsilon_0^2 m_e^2} \left(\frac{m_e}{2\pi k_B T} \right)^{3/2} \,, \tag{2.50}$$

where $m_{in} = m_i m_n / (m_i + m_n)$ and $m_{en} = m_e m_n / (m_e + m_n)$ are the reduced masses. The cross sections for a weakly ionized plasma assuming elastic collisions between solid spheres approximately are $\sigma_{in} = 5 \times 10^{-19} \mathrm{m}^2$ and $\sigma_{en} = 10^{-19} \mathrm{m}^2$ (Vranjes & Krstic 2013; Huba 2016). The Coulomb logarithm, $\ln \Lambda$, is defined as

$$\Lambda = \frac{12\pi (\epsilon_0 k_B T)^{3/2}}{n_e^{1/2} e^3} \,; \tag{2.51}$$

$$\ln \Lambda \approx 16.33 - \frac{1}{2} \ln \left(n_e [\mathrm{m}^{-3}] \right) + \frac{3}{4} \ln \left(T [\mathrm{K}] \right) \,. \tag{2.52}$$

The equations above assume charge neutrality ($n_e = n_i$) and negligible electron mass in comparison with ions/protons mass ($m_e / m_i \approx 0$).

In the particular case of considering a plasma formed only by hydrogen the coefficients multiplying the non-ideal terms in the induction and energy equations result as

$$\eta = \frac{m_e (\nu_{ei} + \nu_{en})}{e^2 n_e \mu_0} \,, \tag{2.53}$$

$$\eta_H = \eta_B = \frac{|B|}{e n_e \mu_0} \,, \tag{2.54}$$

and

$$\eta_A = \frac{(\rho_n / \rho)^2 |B|^2}{(\rho_i \nu_{in} + \rho_e \nu_{en}) \mu_0} \,. \tag{2.55}$$

A more detailed derivation of these equations and a discussion of the relative importance of the non-ideal terms along the solar atmosphere can be found in Khomenko et al. (2014).

2.2.1 Physical meaning/effects of non-ideal terms.

Ohmic term

This term is a classical non-ideal plasma effect present in plasmas. If the plasma is fully ionized, this term is due to the collisions between ions and electrons, otherwise also the collisions between neutrals and electrons should be taken into account. In a plasma, the charge particles move in helical trajectories around the magnetic field, collisions interrupt them so the frozen-in condition breaks and the magnetic field is diffused, meanwhile as a consequence, the magnetic configuration is relaxed, allowing the dissipation of currents. Then, magnetic energy is transform into heat through the Ohmic diffusion term (Joule heating). This relaxation also contributes to the magnetic reconnection and wave instabilities.

Ambipolar term

Ambipolar diffusion term is present in both induction and energy equations and it appears due to the decoupling between charged and neutral components. To investigate this term, we can manipulate the internal energy equation using the Ohm's law, and write it down as

$$\frac{\mathrm{D}\epsilon}{\mathrm{D}t} + \gamma\epsilon\nabla\cdot\mathbf{v} = \eta\mathbf{J}^2 + \eta_A\mathbf{J}_\perp^2 \ . \tag{2.56}$$

The term $\eta\mathbf{J}^2$ correspond to the Joule heating due to the Ohmic dissipation and the term $\eta_A\mathbf{J}_\perp^2$ to the ambipolar dissipation. Both terms have similar form and then it is feasible to interpret the ambipolar term in a similar way as it was done with the Ohmic dissipation. The ambipolar diffusion term is converting magnetic energy into heat by relaxing the magnetic field configuration and dissipating currents. However, the time scale is dictated by ion-neutral collisions, and is significantly shorter than the Ohmic time scale. This would introduce some handicaps in resolving the induction equations as we will show in Chapter 4. Notice that the ambipolar diffusion only affects perpendicular currents which means that by itself it can not produce magnetic reconnection, although certainly due to the relaxation of the magnetic field configuration it can help to trigger it. The effects of the ambipolar diffusion stops when the plasma becomes fully ionized ($\eta_A = 0$) or when the magnetic field adopts a force-free configuration ($\mathbf{J}\times\mathbf{B} = 0;\ \mathbf{J}_\perp = 0$).

Hall term

Hall term appears when there is not enough coupling between ions and neutrals, for example in partially ionized plasmas. This results in the generation of an additional current which can induce effects into magnetic structures and their temporal evolution. One important effect produced by the Hall term is fast-to-Alfvén wave mode transformation, which differs from the geometrical transformation commented in Section 2.4. This transformation occurs because the Hall effect injects, under the appropriate conditions, perturbations in the direction perpendicular to the plane formed by the wave vector and the magnetic field. In Chapters 5 and 6 the physical properties of this term are studied in more detail. This term could introduce some handicaps for resolving the non-ideal MHD equations, however some special numerical techniques can be used to overcame them as it is commented in Chapter 4.

Battery term

This term is interesting since it can be seen as a source term which introduces a seed magnetic field due to gradients in the electron pressure. Seeding magnetic fields by the Battery term was originally

proposed by Kulsrud & Zweibel (2008) as a mechanism for seeding the galactic dynamo. Recently, Khomenko et al. (2017) have investigated its relation to the solar local dynamo, and we will take it into consideration in Chapter 6 to carry on non-ideal MHD magneto-convection simulations.

2.3 Ideal MHD waves

Waves are present in the solar atmosphere and they manifest in a variety of types depending of their own restoring forces. The plasma pressure drives *sound waves*, the magnetic tension drives *Alfvén wave*, the magnetic pressure drives *compressional Alfvén waves* and gravity drives *internal gravity waves*. Another driving force is the Coriolis force which produces *internal waves* but it is not considered here. If all those forces act together, they produce *magneto-acoustic gravity* modes. If the gravity is not considered, the modes are called *magneto-acoustic waves*. And if the magnetic field is absent but not the gravity, the modes are turned into *acoustic gravity waves*.

Considering an ideal single-fluid plasma, the system of equations is given by

$$\frac{\partial \rho}{\partial t} + \nabla \cdot (\rho \mathbf{v}) = 0 \,, \tag{2.57}$$

$$\frac{\partial (\rho \mathbf{v})}{\partial t} + \nabla \cdot \left[\rho \mathbf{v}\mathbf{v} + \left(p + \frac{\mathbf{B}^2}{2\mu_0} \right) \mathbf{I} - \frac{\mathbf{B}\mathbf{B}}{\mu_0} \right] = \rho \mathbf{g} \,, \tag{2.58}$$

$$\frac{\partial e}{\partial t} + \nabla \cdot \left[\frac{\rho \mathbf{v}^2}{2} \mathbf{v} + \frac{\gamma p}{\gamma - 1} \mathbf{v} + \frac{1}{\mu_0} \nabla \cdot [\mathbf{B} \times (\mathbf{v} \times \mathbf{B})] \right] = \rho \mathbf{v} \cdot \mathbf{g} \,, \tag{2.59}$$

$$\frac{\partial \mathbf{B}}{\partial t} = \nabla \times (\mathbf{v} \times \mathbf{B}) \,, \tag{2.60}$$

$$\nabla \cdot \mathbf{B} = 0 \,, \tag{2.61}$$

where the equation of energy (2.59) is written in terms of the total density of energy per volume unit, Eq. (2.44), and the system is closed using the equation of state for an ideal gas

$$p = \frac{\mathbb{R}}{\mu} \rho T \,, \tag{2.62}$$

where $\mathbb{R}$ is the gas constant and μ the mean molecular weight.

2.3.1 Some approximations

The previous equations are written making some assumptions. In the layers treated here (solar near surface layer and solar atmosphere), the Reynolds number $R_e = vL/\nu_k$ is high ($\approx 10^8$) and then the kinematic viscosity (ν_k) of the fluid can be neglected. The magnetic Reynolds number $R_m = vL/\eta$ is also high, being the order of 10^3 to 10^6. Under this condition, it is possible to assume a perfect conductive plasma (high electric conductivity) by neglecting the magnetic diffusivity. Neglecting the magnetic diffusion means that the magnetic field becomes "frozen-in" to plasma. For simplicity, a few more considerations can be assumed, as constant gravity along the outward normal to the solar surface (z-axis), and a stratification thermally in equilibrium so the processes which occur are adiabatic (p/ρ^γ remains constant) and the terms corresponding to the energy losses can be dropped from the energy equation.

2.3.2 Linearized equations

From observations it is known that the solar oscillations have very small amplitudes compared to the typical sound speed of the solar atmosphere, and for that reason they can be considered as small perturbations around a static equilibrium state. Following Christensen-Dalsgaard (2014) and Priest (2014), our physical quantities $\zeta(\mathbf{r},t)$ can be written in general as

$$\zeta(\mathbf{r},t) = \zeta_0(\mathbf{r}) + \zeta_1(\mathbf{r},t)\ , \tag{2.63}$$

where the subscript "0" refers to the equilibrium quantities and the subscript "1" represents a small *Eulerian* perturbation. This can be written using a *Lagrangian* frame of reference where a differential element of volume is moved from its position of equilibrium $\mathbf{r}_0$ an infinitesimal distance $\boldsymbol{\xi}$ as

$$\delta\zeta(\mathbf{r}) = \zeta(\mathbf{r}_0+\boldsymbol{\xi}) - \zeta_0(\mathbf{r}_0) = \zeta(\mathbf{r}_0) + \boldsymbol{\xi}\cdot\nabla\zeta_0 - \zeta_0(\mathbf{r}_0) = \zeta_1(\mathbf{r}_0) + \boldsymbol{\xi}\cdot\nabla\zeta_0\ . \tag{2.64}$$

Thus, the perturbation in velocity is obtained as the time derivative of the displacement vector $\boldsymbol{\xi}$:

$$\mathbf{v}_1 = \frac{\partial\boldsymbol{\xi}}{\partial t}\ , \tag{2.65}$$

by neglecting squares and products of small quantities and taking into account the approximations mentioned before, a linear system of equations is easily obtained:

$$\frac{\partial\rho_1}{\partial t} + \nabla\cdot(\rho_0\mathbf{v}_1) = 0\ , \tag{2.66}$$

$$\frac{\partial(\rho_0\mathbf{v}_1)}{\partial t} + \nabla p_1 + (\nabla\times\mathbf{B}_1)\times\frac{\mathbf{B}_0}{\mu_0} = \rho_1\mathbf{g}\ , \tag{2.67}$$

$$\frac{\partial p_1}{\partial t} + (\mathbf{v}_1\cdot\nabla)p_0 = \gamma\frac{p_0}{\rho_0}\left(\frac{\partial\rho_1}{\partial t} + (\mathbf{v}_1\cdot\nabla)\rho_0\right)\ , \tag{2.68}$$

$$\frac{\partial\mathbf{B}_1}{\partial t} = \nabla\times(\mathbf{v}_1\times\mathbf{B}_0)\ , \tag{2.69}$$

$$\nabla\cdot\mathbf{B}_1 = 0\ , \tag{2.70}$$

where for the equation of energy the adiabatic approximation was used.
A general wave equation can be derived for the perturbation in velocity:

$$\frac{\partial^2\mathbf{v}_1}{\partial t^2} = c_s^2\nabla(\nabla\cdot\mathbf{v}_1) - (\gamma-1)g\hat{\mathbf{z}}(\nabla\cdot\mathbf{v}_1) - g\nabla\mathbf{v}_{1z} + [\nabla\times(\nabla\times(\mathbf{v}_1\times\mathbf{B}_0))]\times\frac{\mathbf{B}_0}{\mu_0\rho_0}\ , \tag{2.71}$$

where $c_s^2 = \gamma p/\rho$ is the adiabatic sound speed. Now, assuming a solution in the form of plane waves, so all variables have a spatial and time dependence of the form $\exp[-i(\omega t + \mathbf{k}\cdot\mathbf{r})]$ and a z dependence to be determined, the perturbed quantities will have the general form $\zeta_1(\mathbf{r},t) = \zeta(z)e^{-i(\omega t+\mathbf{k}\cdot\mathbf{r})}$ and the general solution can be written as:

$$\omega^2\mathbf{v}_1 = c_s^2\mathbf{k}(\mathbf{k}\cdot\mathbf{v}_1) + i(\gamma-1)g\hat{\mathbf{z}}(\mathbf{k}\cdot\mathbf{v}_1) + ig\mathbf{k}v_{1z} + [\mathbf{k}\times(\mathbf{v}_1\times\mathbf{B}_0))]\times\frac{\mathbf{B}_0}{\mu_0\rho_0}\ , \tag{2.72}$$

where ω is the wave frequency and $\mathbf{k}$ is the wavenumber.
For analogy with an elastic string of mass ρ_0 per length unit, where the tension allows transverse waves to propagate along the string with the speed $\mathbf{T}/\rho_0$, it is logical to assume, that now the magnetic

tension, would produce transverse waves propagating along the magnetic field $\mathbf{B}_0$ with a speed known as *Alfvén speed* and defined as:

$$\mathbf{v}_A = \frac{\mathbf{B}_0}{\sqrt{\mu_0 \rho_0}} , \tag{2.73}$$

and then the Equation (2.72) can be re-written as:

$$\begin{aligned} \omega^2 \mathbf{v}_1 = (c_s^2 + v_A^2)(\mathbf{k}\cdot\mathbf{v}_1)\mathbf{k} + (\mathbf{v}_A\cdot\mathbf{k})\big[(\mathbf{v}_A\cdot\mathbf{k})\mathbf{v}_1 - \\ - (\mathbf{v}_1\cdot\mathbf{k})\mathbf{v}_A - (\mathbf{v}_A\cdot\mathbf{v}_1)\mathbf{k}\big] + ig\big[(\gamma-1)\hat{\mathbf{z}}(\mathbf{k}\cdot\mathbf{v}_1) + \mathbf{k}v_{1z}\big] . \end{aligned} \tag{2.74}$$

2.3.3 Magnetoacoustic waves in an unstratified medium.

If the wavelength of the perturbations is smaller than the pressure scale height, the gravity can be neglected from Equation (2.74) yielding to the solution

$$\omega^2 \mathbf{v}_1 = (c_s^2 + v_A^2)(\mathbf{k}\cdot\mathbf{v}_1)\mathbf{k} + (\mathbf{v}_A\cdot\mathbf{k})\left[(\mathbf{v}_A\cdot\mathbf{k})\mathbf{v}_1 - (\mathbf{v}_1\cdot\mathbf{k})\mathbf{v}_A - (\mathbf{v}_A\cdot\mathbf{v}_1)\mathbf{k}\right] , \tag{2.75}$$

this equation leads to simple solutions for some propagation parallel or perpendicular to the background magnetic field.

Propagation $\mathbf{k} \perp \mathbf{B}_0$

When the propagation of the wave is perpendicular to the magnetic field $\mathbf{k}\cdot\mathbf{v}_A = 0$ then the Equation (2.75) can be reduced to

$$\omega^2 \mathbf{v}_1 = (c_s^2 + v_A^2)(\mathbf{k}\cdot\mathbf{v}_1)\mathbf{k} , \tag{2.76}$$

from where is obtained that $\mathbf{v}_1 \parallel \mathbf{k}$, so that $\mathbf{k}\cdot\mathbf{v}_1 = kv_1$ and then the dispersion relation correspond to a *longitudinal wave*

$$\omega^2 = k^2(c_s^2 + v_A^2) . \tag{2.77}$$

This wave is known as *compressional Alfvén wave* or *fast Alfvén wave*.

Propagation $\mathbf{k} \parallel \mathbf{B}_0$

When the propagation occurs along the magnetic field $\mathbf{k} \parallel \mathbf{B}_0$ and then $\mathbf{k}\cdot\mathbf{v}_A = kv_A$, allowing to write the Equation (2.75) as

$$\omega^2 \mathbf{v}_1 = k^2 v_A^2 \mathbf{v}_1 + (c_s^2/v_A^2 - 1)k^2(\mathbf{v}_1\cdot\mathbf{v}_A)\mathbf{v}_A , \tag{2.78}$$

now there are two possible solutions, one for $\mathbf{v}_1 \parallel \mathbf{B}_0 \parallel \mathbf{k}$, resulting in a *longitudinal sound wave* with the phase velocity $\omega/k = c_s$ and the other one for $\mathbf{v}_1 \perp \mathbf{B}_0 \parallel \mathbf{k}$, leading to a transverse wave with the phase velocity $\omega/k = v_A$ and known as *Alfvén wave*, *shear Alfvén wave* or *slow Alfvén wave*.

Propagation in any direction

Introducing a Cartesian coordinate system with the y-axis normal to the plane where $\mathbf{k}$ and $\mathbf{B}_0$ lie, the Equation (2.75) can be split into three equations, each for three projections x, y, and z.
Using the equations corresponding to the components x and z, the dispersion relation

$$\omega^4 - \omega^2 k^2(c_s^2 + v_A^2) + c_s^2 v_A^2 k^4 \cos^2\theta_B = 0 , \tag{2.79}$$

can be obtained, which has two $\omega/k > 0$ solutions, the one with higher propagation speed is called *fast magneto-acoustic wave* and the other with the lower speed, *slow magneto-acoustic wave*. Using

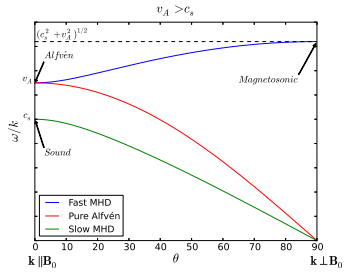

FIGURE 2.2— The phase velocity of the fast MHD mode increases from v_A to the limit value of $\sqrt{c_s^2+v_A^2}$ so it is changing from an Alfvén wave to a Magneto-sonic wave, while the Slow MHD wave starts as a Sound wave and disappears when the angle increases. The Pure Alfvén wave starts as Alfvén wave with the speed v_A at $\theta = 0°$ and disappears when $\theta = 90°$.

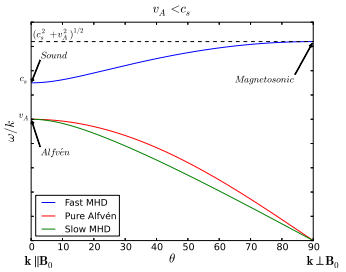

FIGURE 2.3— The phase velocity for the fast MHD mode increases from c_s to the limit value of $\sqrt{c_s^2+v_A^2}$ so the Sound wave becomes a Magneto-sonic wave while the Slow MHD wave starts as the Alfvén wave and disappears when the angle increases. The Pure Alfvén wave starts as Alfvén wave with the speed c_s at $\theta = 0°$ and disappears when $\theta = 90°$.

the other component equation for $v_{1y} \neq 0$, the solution is a linearly polarized wave perpendicular to both $\mathbf{k}$ and $\mathbf{B}_0$ with phase speed

$$\omega = k v_A \cos(\theta_B) \tag{2.80}$$

and known as *Pure Alfvén wave*. Then, Alfvén waves (Alfvén 1942) are plasma perturbations whose restoring force is the magnetic tension instead of gas or magnetic pressure. They carry energy along the magnetic field lines but the motion of the charged particles, which provide the inertia, and the magnetic field perturbation are transverse to the field.

The Figures 2.2 and 2.3 show the phase velocity for all these solutions as a function of the angle θ_B between $\mathbf{k}$ and $\mathbf{B}_0$ for both cases $v_A > c_s$ and $v_A < c_s$ respectively.

2.3.4 Magnetoacoustic-gravity waves.

Now, if the gravity is not negligible, the Equation (2.75) has to be considered. Following the work done by Ferraro & Plumpton (1958) and Zhugzhda & Dzhalilov (1984), a Cartesian system where $\mathbf{v}_1$ will be independent of the y-coordinate can be considered, so the coefficients of the plane wave approximation will be only z-coordinate dependent $\mathbf{f}(z) = (f_x, f_y, f_z)$. A vertical constant magnetic field with the propagation occurring only in the vertical direction ($k = 0$) can be also considered. Then, the solution can be split into three components and simplified as shown bellow.

$$\left[v_A^2\left(\frac{\partial^2}{\partial z^2} - k^2\right) - k^2 c_s^2 + \omega^2\right] f_x = -ik\left(c_s^2 \frac{\partial}{\partial z} - g\right) f_z \quad \xrightarrow{k=0} \quad \begin{cases} f_x = 0 & \text{(a)} \\ v_A^2 \frac{\partial^2 f_x}{\partial z^2} + \omega^2 f_x = 0 & \text{(b)} \end{cases} \tag{2.81}$$

$$\left(c_s^2 \frac{\partial^2}{\partial z^2} - \gamma g \frac{\partial}{\partial z} + \omega^2\right) f_z = -ik\left[c_s^2 \frac{\partial}{\partial z} - (\gamma - 1) g\right] f_x \quad \xrightarrow{k=0} \quad c_s^2 \frac{\partial^2 f_z}{\partial z^2} - \gamma g \frac{\partial f_z}{\partial z} + \omega^2 f_z = 0\,, \tag{2.82}$$

$$v_A^2 \frac{\partial^2 f_y}{\partial z^2} + \omega^2 f_y = 0\,. \tag{2.83}$$

Acoustic solution

From Equation (2.82), taking a solution of the form $f_z = A\exp(z/2H_0)\exp(ik_z z)$, the dispersion relation $k_z c_s = \mp\sqrt{\omega^2 - \omega_c^2}$ and the solutions

$$f_z = A\exp\left[\left(\frac{1}{2H_0} \mp \frac{\sqrt{\omega^2-\omega_c^2}}{c_s}\right) z\right] \quad \text{if} \quad \omega < \omega_c\,,$$
$$f_z = A\exp\left[\left(\frac{z}{2H_0} \mp i\frac{\sqrt{\omega^2-\omega_c^2}}{c_s}\right) z\right] \quad \text{if} \quad \omega > \omega_c\,, \tag{2.84}$$

can be obtained, where $\omega_c = \gamma g/(2c_s)$ is the acoustic cut-off frequency and $H_0 = c_s^2/(\gamma g)$ is the pressure scale height. When $\omega < \omega_c$ the perturbation is evanescent and produces stationary waves. When $\omega > \omega_c$ the perturbation amplitude grows exponentially with height, it is a propagating wave.

Magnetic solution

The Equations (2.83) and (2.81b) give the solution for Alfvén waves with the general form of

$$f_{\{x,y\}} = A\mathcal{J}_0\left(\frac{2\omega H_0}{v_A}\right) + B\mathcal{Y}_0\left(\frac{2\omega H_0}{v_A}\right)\,, \tag{2.85}$$

where $\mathcal{J}_0$ and $\mathcal{Y}_0$ are the *Bessel functions* of order zero of first and second type, and A and B are two constants.

2.4 Mode transformation

For mode transformation (or mode conversion) it is important to define the plasma β coefficient. This coefficient offers information about if the medium is magnetically dominated or not. It is strictly defined as the ratio between the gas and magnetic pressure $\beta = p_{\rm gas}/p_{\rm mag}$. Values of $\beta > 1$ means the medium is gas dominated and values $\beta < 1$ means the medium is magnetically dominated. Values of $\beta \approx 1$ correspond to a region called *equipartition layer*.

In the solar atmosphere, the presence of gradients and strong vertical stratification allow for the process of mode transformation. The Alfvén speed can increase orders of magnitude in a short distance at the upper photosphere and low chromosphere, because of the density fall off. Therefore a geometrical region, where the sound speed is equal to the Alfvén speed ($v_A = c_s$), will exist at some height in the atmosphere.

Due to the phase velocity of both modes will be similar around this layer, to keep the continuity of the dispersion relation, different modes can interact with each other producing a waves transformation and then the energy may be transfer from one mode to the other. Fast/slow magnetoacoustic coupling takes place around this region.

The mathematical formalism of mode conversion was developed by Schunker & Cally (2006) and Cally (2006, 2007) based on the generalized ray theory of Tracy et al. (2003). In the solar literature, the equipartition layer is either defined as where the plasma β or the ratio of acoustic and Alfvén speeds squared, c_s^2/v_A^2, reaches unity. This last definition is more convenient from the point of view of wave propagation. These two definitions differ by the factor $\gamma/2$. The wave speed equipartition is the more physically relevant criterion, but in practice there is little difference due to the mode wavelength is typically larger than the transition region width.

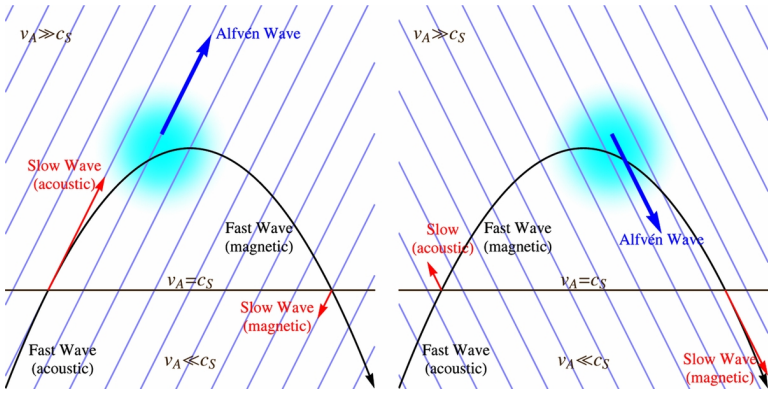

FIGURE 2.4— Mode conversion diagram from Khomenko & Cally (2012). The blue lines represent the magnetic field projection over the plane. This magnetic field is given by the inclination angle θ respect the vertical and the azimuth angle ϕ. The left panel shows a fast (acoustic) wave into a high β region propagating upwards. When this wave reaches the equipartition layer the rays split into a fast (magnetic) wave, shown in black, and a slow (acoustic) wave propagating along the field lines, shown in red. Due to the Alfvén speed is increasing upward, the fast wave will be refracted around z_r and the geometrical mode conversion fast-to-Alfvén wave occurs in the region represented as a fuzzy blob.

Fast-to-slow magneto acoustic mode conversion

If the angle between the magnetic field and the wave vector is small, $\theta_B \approx 0$ around the equipartition layer, the fast MHD mode may become a slow MHD mode but keeping its physical nature (magnetic or sonic). On the other hand, if the vectors are perpendicular in that region, $\theta_B \approx \pi/2$, a slow mode continues as slow mode, but changing its physical nature from acoustic to magnetic and the same occurs for the fast mode. For frequencies above the cut-off frequency ω_c, the coefficient of transformation fast-to-slow was derived by Cally (2006) as

$$\mathcal{C} = \exp\left[-k\pi \sin^2\theta_B \left(\frac{\partial\beta}{\partial s}\right)^{-1}\right], \tag{2.86}$$

where plasma β is defined here as $\beta = c_s^2/v_A^2$, s is the distance along the direction $\mathbf{k}$ and θ_B is the angle between the magnetic field $\mathbf{B}$ and the direction of wave propagation $\mathbf{k}$. If the angle is other than the mentioned before, the transformation is partial, therefor the transformation depends on the angle and part of the incident fast mode goes into a slow one, and another part continues as fast.

Fast-to-Alfvén mode conversion

In the solar atmosphere, Alfvén waves can appear for example by a random perturbation in the photosphere (Kudoh & Shibata 1999), by magnetic reconnection (Kigure et al. 2010), or by means of ideal-MHD fast-to-Alfvén transformation. This mode transformation happens where the fast wave reflects due to the density stratification, this is, around a reflection height (z_r), as Cally & Hansen (2011) suggested. This height is typically well above the equipartition level, but depends on the wave

frequency and horizontal wavenumber, see the blue fuzzy blob in Figure 2.4. In a low β plasma, the reflection point is near the height where the horizontal phase speed matches the Alfvén speed, and so is higher for high frequency and for near-vertical propagation. This process could be an important mechanism to provide energy to the solar corona. This is so because unlike fast waves, which reflect in the transition region or chromosphere due to the rapidly increasing Alfvén speed, Alfvén waves generated through the mode transformation close to the transition region are more able to overcome this barrier, and to reach the corona. The efficiency of this mode conversion depends on the local relative inclination between the wave vector and the background magnetic field, for this reason is also called geometrical fast-to-Alfvén mode transformation (Cally & Goossens 2008; Cally 2009; Cally & Hansen 2011; Khomenko & Cally 2011, 2012; Felipe 2012). Observations realized by De Pontieu et al. (2007c), Tomczyk et al. (2007) or Jess et al. (2009) have shown that Alfvén waves are everywhere in the corona. Later on, observations from McIntosh et al. (2011) and Jess et al. (2012) have shown that these Alfvénic waves are of sufficient amplitude to heat some regions and contribute to the acceleration of the solar wind. Recently, Srivastava et al. (2017) have reported the first observation of high-frequency torsional Alfvén waves (∼12–42 mHz) in the solar chromosphere. In Chapter 5 a new mechanism of mode transformation fast-to-Alfvén by means of the non-ideal Hall effect will be discussed.

2.5 Mode identification: a note on the velocity projections

In a semi empirical solar stratification, as the one we had considered for our experiments presented later in this thesis, the identification of the different modes is a tough task because they are physically mixed. In this work, in order to carry out the mode selection we have used the properties of MHD waves and made the change of base using the triad $(\mathbf{e}_{\rm long}, \mathbf{e}_{\rm perp}, \mathbf{e}_{\rm trans})$ as used by Cally & Goossens (2008), also mention as the *mixed field line/magnetic surface triad* by Goedbloed et al. (2010),

$$\mathbf{e}_{\rm long} = \cos\phi \sin\theta\, \mathbf{e}_x + \sin\phi \sin\theta\, \mathbf{e}_y + \cos\theta\, \mathbf{e}_z \,, \tag{2.87a}$$
$$\mathbf{e}_{\rm perp} = -\cos\phi \sin^2\theta \sin\phi\, \mathbf{e}_x + (1 - \sin^2\phi \sin^2\theta)\, \mathbf{e}_y - \cos\theta \sin\theta \sin\phi\, \mathbf{e}_z \,, \tag{2.87b}$$
$$\mathbf{e}_{\rm tran} = -\cos\theta\, \mathbf{e}_x, + \cos\phi \sin\theta\, \mathbf{e}_z \,. \tag{2.87c}$$

This new basis allow us to select the Alfvén mode (for any plasma β). However, $\mathbf{e}_{\rm long}$ and $\mathbf{e}_{\rm tran}$ generally select a mixture of slow/fast magneto-acoustic modes depending on plasma β.

To verify the behavior of the projections, we can use the ideal MHD formulation and consider a simple case with an infinite uniform plasma with a constant vertical magnetic field $\mathbf{B} = B_0 \mathbf{e}_z$ and $k_y = 0$. In this case, the transformation between the bases is simplified to

$$\mathbf{e}_{\rm long} = \mathbf{e}_z, \quad \mathbf{e}_{\rm perp} = \mathbf{e}_y, \quad \mathbf{e}_{\rm tran} = \mathbf{e}_x \,. \tag{2.88}$$

We can define the displacement associated to the Alfvén wave and the slow/fast magneto-acoustic waves as

$$\mathbf{X}_F = (\boldsymbol{\xi} \cdot \mathbf{e}_{\rm tran})\, \mathbf{e}_{\rm tran} = \xi_x \mathbf{e}_{\rm x} \,, \tag{2.89a}$$
$$\mathbf{X}_A = (\boldsymbol{\xi} \cdot \mathbf{e}_{\rm perp})\, \mathbf{e}_{\rm perp} = \xi_y \mathbf{e}_{\rm y} \,, \tag{2.89b}$$
$$\mathbf{X}_S = (\boldsymbol{\xi} \cdot \mathbf{e}_{\rm long})\, \mathbf{e}_{\rm long} = \xi_z \mathbf{e}_{\rm z} \,. \tag{2.89c}$$

The eigenfunctions for the incompressible Alfvén wave $\boldsymbol{\xi}_A$, and both the slow and fast magneto-acoustic waves, $\boldsymbol{\xi}_{\{S,F\}}$, in this case are given by

$$\boldsymbol{\xi}_A = \xi_y \mathbf{e}_y \,, \tag{2.90}$$

$$\boldsymbol{\xi}_S = \xi_z \left(\frac{\omega_S^2}{\omega_S^2 - k^2 v_A^2} \frac{k_x}{k_z} \mathbf{e}_x + \mathbf{e}_z \right) = \xi_x \left(\mathbf{e}_x + \frac{\omega_S^2 - k^2 v_A^2}{\omega_S^2} \frac{k_z}{k_x} \mathbf{e}_z \right) , \tag{2.91}$$

$$\boldsymbol{\xi}_F = \xi_z \left(\frac{\omega_F^2}{\omega_F^2 - k^2 v_A^2} \frac{k_x}{k_z} \mathbf{e}_x + \mathbf{e}_z \right) = \xi_x \left(\mathbf{e}_x + \frac{\omega_F^2 - k^2 v_A^2}{\omega_F^2} \frac{k_z}{k_x} \mathbf{e}_z \right) , \tag{2.92}$$

where the slow/fast magneto-acoustic frequencies, $\omega_{\{S,F\}}$, are

$$\omega_{\{S,F\}} = \frac{k^2(c_s^2 + v_A^2)}{2} \left\{ 1 \pm \left(1 - \frac{4\omega_C^2}{k^2(c_s^2 + v_A^2)} \right)^{1/2} \right\} , \tag{2.93}$$

with $\omega_C = k_z v_C$ being the cusp frequency, and v_C the cusp velocity $v_C^2 = c_s^2 v_A^2/(c_s^2 + v_A^2)$. It is clear from Eq. (2.90) that $\boldsymbol{\xi}_A = \mathbf{X}_A$ holds in general. From Eqs. (2.91) and (2.92) it can be seen that the slow and fast mode displacements are formed by a linear combination of eigen displacements (2.89). In the limit of low plasma β,

$$\boldsymbol{\xi}_S \approx \mathbf{X}_S, \;\; \boldsymbol{\xi}_F \approx \mathbf{X}_F. \tag{2.94}$$

while in the limit of high plasma β,

$$\boldsymbol{\xi}_S \approx \xi_z(\mathbf{e}_z - \frac{k_z}{k_x}\mathbf{e}_x), \;\; \boldsymbol{\xi}_F = \xi_x(\mathbf{e}_x + \frac{k_z}{k_x}\mathbf{e}_z). \tag{2.95}$$

So the above projection only allows us to separate fast and slow magneto-acoustic modes in the limit of low plasma β. More details about this can be found in Goossens (2003), chapter 5.

2.6 Convection

The Standard Model considers the interior of the Sun as a sphere form by concentric shells where all the thermodynamic variables are function of the radial distance from the center, Fig 1.1. Assuming the perfect gas law for the EOS it is possible to write a hydrostatic force balance between the pressure and gravity as

$$\frac{dp}{dr} = -\rho g \, , \tag{2.96}$$

and consider a steady-state energy balance

$$\frac{dL(r)}{dr} = 4\pi r^2 \rho \epsilon \, , \tag{2.97}$$

where ϵ is the rate of nuclear energy generation and $L(r)$ is the thermal energy outflow trough a sphere, which outside the core has a constant value ($L_\odot = 3.86 \times 10^{26}$ W). Inside the radiative zone the energy is transport by radiation and it is in radiative equilibrium so the temperature gradient for radiative transport can be written as

$$\frac{dT}{dr} = -\frac{3\kappa_{\rm R}\rho}{16\sigma_{\rm SB}T^3} \frac{L}{4\pi r^2} \, , \tag{2.98}$$

where $\sigma_{\rm SB} = 5.6705 \times 10^{-8}$W m^{-2} K^{-4} is the Stefan-Boltzmann constant and $\kappa_{\rm R}$ the Rosseland mean opacity.

Inside the convective zone the temperature gradient becomes steeper, reaching a limit where the material can not remain in a stable equilibrium against gravity and the energy will be transported by convection. The rise of the opacity when moving outwards originates the increase of the temperature gradient, so hot bubble of matter move upward. The opposite occurs when those bubbles reach the

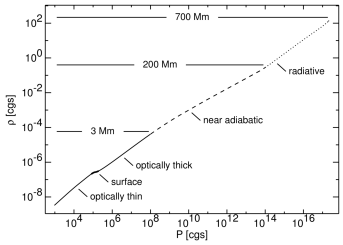

FIGURE 2.5— Averaged pressure and density relation into the Solar stratification. The dashed part of the curve roughly correspond with the convective zone and shows a near adiabatic relation between them. Extracted from Nordlund et al. (2009).

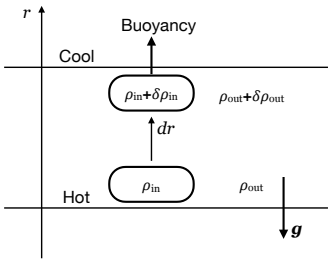

FIGURE 2.6— Vertical displacement of a convective bubble traveling outward a distance dr. The conditions inside the bubble are designated by a subscript "in" and outside by the subscript "out".

photosphere, the opacity decreases letting photons to escape and the cooled down material starts to sink. Convective motions then involve mass movements, which in general are turbulent and have a subsonic velocity. Thus the stratification can be considered adiabatic, see Fig. 2.5, and then most of the convection zone, specially the lower part, can be considered close to a perfect polytrope.

The rising bubbles, Fig. 2.6, are feeling a buoyancy force while the density changes inside ($\delta\rho_{\rm in}$) are smaller than the density changes outside ($\delta\rho_{\rm out}$), this is,

$$\delta\rho_{\rm in} < \delta\rho_{\rm out} \, . \tag{2.99}$$

By considering the perfect gas law ($p = k_{\rm B}\rho T/m$) and differentiating it, we can write the changes in pressure, density, and temperature inside,

$$\frac{\delta p_{\rm in}}{p} = \frac{\delta\rho_{\rm in}}{\rho} + \frac{\delta T_{\rm in}}{T} \, , \tag{2.100}$$

and outside the parcels of matter,

$$\frac{\delta p_{\rm out}}{p} = \frac{\delta\rho_{\rm out}}{\rho} + \frac{\delta T_{\rm out}}{T} \, . \tag{2.101}$$

Because the movement upward is slow the bubble of plasma remains in horizontal pressure equilibrium with the surroundings and then $\delta p_{\rm in} = \delta p_{\rm out}$ which implies, after using Eqs. (2.99), (2.100), and (2.101), that the parcel of matter will continue rising if

$$\left|\frac{dT_{\rm out}}{dr}\right| > \left|\frac{dT_{\rm in}}{dr}\right| \, . \tag{2.102}$$

Under the previous assumption, the parcel of matter is governed by

$$p_{\rm in} = \frac{k_B}{m}\rho_{\rm in}T_{\rm in}, \quad \frac{dp_{\rm in}}{dr} = -\rho_{\rm in}g, \quad \frac{p_{\rm in}}{\rho_{\rm in}^{\gamma}} = \text{constant} \, , \tag{2.103}$$

which combined become

$$\left|\frac{dT_{\rm out}}{dr}\right| > \frac{\gamma-1}{\gamma}\frac{gm}{k_{\rm B}}\,. \tag{2.104}$$

This Equation is known as the Schwarzschild criterion for convective instability. At the surface and across the convection zone the EOS is strongly affected by ionization fraction since at the bottom part the gas is fully ionized and at the surface the gas is partially ionized. This will introduce changes in the values of the factor $(\gamma-1)/\gamma$ in the Eq. (2.104).

The first numerical treatment of those convective motions considered that the rising bubble travels outward some distance before disintegrating and thermalizes with the surroundings. This distance is known as mixing-length and can be written in terms of a free parameter α and the pressure scale height H_p, Eq. (2.105), as $l = \alpha H_p$.

$$H_p = -\frac{1}{p}\frac{\partial p}{\partial r}\,. \tag{2.105}$$

More about the mixing-length formalism can be found for example in Carroll & Ostlie (1996). In Chapter 6 we will discuss recent numerical magneto-convection simulations.

3

The numerical code MANCHA3D

Always code as if the guy who ends up maintaining your code will be a violent psychopath who knows where you live. Code for readability.

- John F. Woods, Programmer and former UK based computer game producer, 1991.

THIS chapter describes briefly the current version of the numerical code MANCHA3D developed by Felipe et al. (2010). We will use this code as a starting point to implement the new numerical techniques exposed in Chapter 4 and it is used to carry out the numerical experiments, tests and simulations shown in Chapters 5 and 6.

3.1 Outline

The current implementation of the numerical code MANCHA3D is a parallel tridimensional extension of the code developed by Khomenko & Collados (2006). It solves the non-linear non-ideal 3D MHD equations for the perturbations written in conservative form (Felipe et al. 2010; Khomenko & Collados 2012). It is written in FORTRAN 95 and it is fully parallelized using the MPI and HDF-5 libraries.

To avoid high frequency numerical noise and improve the numerical stability artificial diffusion terms are added instead of their physical counterparts following the work of Vögler et al. (2005). Each numerical diffusivity coefficient has its own contribution formed by a constant in time contribution, a hyperdiffusivity part and a shock-resolving part. Because in some simulations a high diffusivity is not desirable (especially when solving for waves) the code can perform an additional filtering to damp small wavelengths using the method described by Parchevsky & Kosovichev (2007). This way, the artificial diffusivity remains low and the numerical noise is avoided. For spatial integration MANCHA3D uses a centered 6^{th} order accurate derivative, following Nordlund & Galsgaard (1995). To advance in time it uses an explicit multi-step Runge-Kutta (RK) scheme, accurate to 4^{th} order (Vögler et al. 2005; Khomenko & Collados 2006; Felipe et al. 2010). To prevent wave reflection at the boundaries, especially when working with complex magnetic field configurations, the code has a perfectly matched layer (PML; Berenger 1994, 1996; Hu 1996; Hesthaven 1998; Hu 2001; Parchevsky & Kosovichev 2009). It also has the possibility of using some adaptive mesh refinement (AMR) method (Berger & Colella 1989) to follow the evolution of fine structures.

More recently, a new radiative transfer module has been added to solve the radiative transfer equations using the short characteristic method. It is also possible to choose between an ideal equation of state or a realistic one in thermodynamical equilibrium based on precalculated tables, which include

the ionization equilibrium solution and the electron pressure needed to calculate the non-ideal terms, see Khomenko & Collados (2012) and Khomenko et al. (2017) for details.

The pure MHD part of the code has been verified against standard numerical tests by Felipe et al. (2010) and the code has been used in a wide range of numerical experiments (both ideal and realistic), such as modeling of wave propagation, instabilities, and magneto-convection (e.g., Felipe et al. 2010; Khomenko & Collados 2012; Felipe et al. 2013; Luna et al. 2016; Felipe et al. 2016; Santamaria et al. 2016; Khomenko et al. 2017).

The non-ideal MHD part of the code has been used in recent numerical experiments such as the seed of magnetic fields by means of the Biermann battery term, mode transformation in the presence of ambipolar diffusion or the effects introduced by the ambipolar term into the radiative magneto-convection phenomena (e.g., Khomenko et al. 2017; Cally & Khomenko 2018; Khomenko et al. 2018). Chapter 4 contains the numerical validation of each of the non-ideal terms implemented into the current version of the code.

3.2 MHD equations for the perturbations

Inserting an expression like (2.63) for each variable into the equations of continuity (2.57), motion (2.58), energy (2.59), and induction (2.60), a system of non-linear differential equations for the perturbations in a magnetized non-ideal plasma can be obtained.

- Continuity

$$\frac{\partial \rho_1}{\partial t} + \nabla \cdot [(\rho_0 + \rho_1)\mathbf{v}_1] = \left(\frac{\partial \rho_1}{\partial t}\right)_{\text{diff}} , \tag{3.1}$$

where in this section and bellow the subscript "0" denotes the background values, the subscript "1" is for the perturbations, and the subscript "diff" denotes the artificial diffusion terms which will be describe in Section 3.5.

- Momentum

$$\begin{aligned} &\frac{\partial[(\rho_0+\rho_1)\mathbf{v}_1]}{\partial t} + \nabla \cdot \left[(\rho_0+\rho_1)\mathbf{v}_1\mathbf{v}_1 + \left(p_1 + \frac{\mathbf{B}_1^2}{2\mu_0} + \frac{\mathbf{B}_1 \cdot \mathbf{B}_0}{\mu_0}\right)\mathbf{I} - \right. \\ &\left. - \frac{1}{\mu_0}(\mathbf{B}_0\mathbf{B}_1 + \mathbf{B}_1\mathbf{B}_0 + \mathbf{B}_1\mathbf{B}_1)\right] = (\rho_0+\rho_1)\mathbf{g} + \mathbf{S}(t) + \left(\frac{\partial[(\rho_0+\rho_1)\mathbf{v}_1]}{\partial t}\right)_{\text{diff}} , \end{aligned} \tag{3.2}$$

- Energy

$$\begin{aligned} &\frac{\partial e_1}{\partial t} + \nabla \cdot \left[\mathbf{v}_1\left((e_0+e_1) + (p_0+p_1) + \frac{|\mathbf{B}_0+\mathbf{B}_1|^2}{2\mu_0}\right) - \right. \\ &\left. - \frac{1}{\mu_0}(\mathbf{B}_0+\mathbf{B}_1)\left[\mathbf{v}_1 \cdot (\mathbf{B}_0+\mathbf{B}_1)\right]\right] = (\rho_0+\rho_1)\mathbf{v}_1 \cdot \mathbf{g} + Q_{\text{rad}} + \\ &+ \left(\frac{\partial e_1}{\partial t}\right)_{\text{diff}} + \left(\frac{\partial e_1}{\partial t}\right)_{\text{non-ideal}} , \end{aligned} \tag{3.3}$$

where the last term on the right-hand side with the subscript "non-ideal" is the sum of non-ideal terms.

$$\left(\frac{\partial e_1}{\partial t}\right)_{\text{non-ideal}} = \left(\frac{\partial e_1}{\partial t}\right)_{\text{Ohm}} + \left(\frac{\partial e_1}{\partial t}\right)_{\text{Ambi}} + \left(\frac{\partial e_1}{\partial t}\right)_{\text{Batt}} . \tag{3.4}$$

Expanding these terms we have:

$$\begin{aligned}\left(\frac{\partial e_1}{\partial t}\right)_{\text{Ohm}}+\left(\frac{\partial e_1}{\partial t}\right)_{\text{Ambi}} &= \nabla\cdot[\mathbf{B}\times(\eta+\eta_A)\,\mathbf{J}_\perp] = \\ &= \frac{\partial}{\partial x}\Big((\eta+\eta_A)(B_yJ_{\perp z}-B_zJ_{\perp y})\Big)- \\ &- \frac{\partial}{\partial y}\Big((\eta+\eta_A)(B_xJ_{\perp z}-B_zJ_{\perp x})\Big)+ \\ &+ \frac{\partial}{\partial z}\Big((\eta+\eta_A)(B_xJ_{\perp y}-B_yJ_{\perp x})\Big)\,,\end{aligned} \tag{3.5}$$

$$\begin{aligned}\left(\frac{\partial e_1}{\partial t}\right)_{\text{Batt}} &= \nabla\cdot\left[\eta_B\frac{\nabla p_e\times\mathbf{B}}{|B|}\right] = \\ &= \frac{\partial}{\partial x}\Big(\frac{\eta_B}{|B|}(\frac{\partial p_e}{\partial y}B_z-\frac{\partial p_e}{\partial z}B_y)\Big)- \\ &- \frac{\partial}{\partial x}\Big(\frac{\eta_B}{|B|}(\frac{\partial p_e}{\partial x}B_z-\frac{\partial p_e}{\partial z}B_x)\Big)+ \\ &+ \frac{\partial}{\partial x}\Big(\frac{\eta_B}{|B|}(\frac{\partial p_e}{\partial x}B_y-\frac{\partial p_e}{\partial y}B_x)\Big)\,,\end{aligned} \tag{3.6}$$

with

$$e_1=\frac{1}{2}(\rho_0+\rho_1)\mathbf{v}_1^2+\frac{p_1}{\gamma-1}+\frac{1}{2\mu_0}(\mathbf{B}_1^2+2\mathbf{B}_0\cdot\mathbf{B}_1)\,. \tag{3.7}$$

⊙ Induction

$$\frac{\partial\mathbf{B}_1}{\partial t}=\nabla\times[\mathbf{v}_1\times(\mathbf{B}_0+\mathbf{B}_1)]+\left(\frac{\partial\mathbf{B}_1}{\partial t}\right)_{\text{diff}}+\left(\frac{\partial\mathbf{B}_1}{\partial t}\right)_{\text{non-ideal}}\,, \tag{3.8}$$

The first term on the right-hand side is called convective term and can be written in components as:

$$\left(\frac{\partial B_x}{\partial t}\right)_{\text{conv}} = \frac{\partial}{\partial y}\Big(v_xB_y-v_yB_x\Big)+\frac{\partial}{\partial z}\Big(v_xB_z-v_zB_x\Big)\,, \tag{3.9a}$$

$$\left(\frac{\partial B_y}{\partial t}\right)_{\text{conv}} = -\frac{\partial}{\partial x}\Big(v_xB_y-v_yB_x\Big)+\frac{\partial}{\partial z}\Big(v_yB_z-v_zB_y\Big)\,, \tag{3.9b}$$

$$\left(\frac{\partial B_z}{\partial t}\right)_{\text{conv}} = -\frac{\partial}{\partial x}\Big(v_xB_z-v_zB_x\Big)-\frac{\partial}{\partial y}\Big(v_yB_z-v_zB_y\Big)\,, \tag{3.9c}$$

and the third one is the sum of non-ideal terms,

$$\left(\frac{\partial\mathbf{B}_1}{\partial t}\right)_{\text{non-ideal}}=\left(\frac{\partial\mathbf{B}_1}{\partial t}\right)_{\text{Ohm}}+\left(\frac{\partial\mathbf{B}_1}{\partial t}\right)_{\text{Ambi}}+\left(\frac{\partial\mathbf{B}_1}{\partial t}\right)_{\text{Hall}}+\left(\frac{\partial\mathbf{B}_1}{\partial t}\right)_{\text{Batt}}\,. \tag{3.10}$$

Expanding those terms we have the Ohmic term:

$$\left(\frac{\partial B_x}{\partial t}\right)_{\text{Ohm}} = -\frac{\partial}{\partial y}\Big(\eta\mu_0J_z\Big)+\frac{\partial}{\partial z}\Big(\eta\mu_0J_y\Big)\,, \tag{3.11a}$$

$$\left(\frac{\partial B_y}{\partial t}\right)_{\text{Ohm}} = \frac{\partial}{\partial x}\Big(\eta\mu_0J_z\Big)-\frac{\partial}{\partial z}\Big(\eta\mu_0J_x\Big)\,, \tag{3.11b}$$

$$\left(\frac{\partial B_z}{\partial t}\right)_{\text{Ohm}} = -\frac{\partial}{\partial x}\Big(\eta\mu_0J_y\Big)+\frac{\partial}{\partial y}\Big(\eta\mu_0J_x\Big)\,, \tag{3.11c}$$

for the ambipolar term:

$$\left(\frac{\partial B_x}{\partial t}\right)_{\text{Ambi}} = -\frac{\partial}{\partial y}\left(\eta_A \mu_0 J_{\perp z}\right) + \frac{\partial}{\partial z}\left(\eta_A \mu_0 J_{\perp y}\right), \tag{3.12a}$$

$$\left(\frac{\partial B_y}{\partial t}\right)_{\text{Ambi}} = \frac{\partial}{\partial x}\left(\eta_A \mu_0 J_{\perp z}\right) - \frac{\partial}{\partial z}\left(\eta_A \mu_0 J_{\perp x}\right), \tag{3.12b}$$

$$\left(\frac{\partial B_z}{\partial t}\right)_{\text{Ambi}} = -\frac{\partial}{\partial x}\left(\eta_A \mu_0 J_{\perp y}\right) + \frac{\partial}{\partial y}\left(\eta_A \mu_0 J_{\perp x}\right), \tag{3.12c}$$

for the Hall term:

$$\left(\frac{\partial B_x}{\partial t}\right)_{\text{Hall}} = -\frac{\partial}{\partial y}\left(\frac{\eta_H \mu_0}{|B|}(J_x B_y - J_y B_x)\right) - \frac{\partial}{\partial z}\left(\frac{\eta_H \mu_0}{|B|}(J_x B_z - J_z B_x)\right), \tag{3.13a}$$

$$\left(\frac{\partial B_y}{\partial t}\right)_{\text{Hall}} = \frac{\partial}{\partial x}\left(\frac{\eta_H \mu_0}{|B|}(J_x B_y - J_y B_x)\right) - \frac{\partial}{\partial z}\left(\frac{\eta_H \mu_0}{|B|}(J_y B_z - J_z B_y)\right), \tag{3.13b}$$

$$\left(\frac{\partial B_z}{\partial t}\right)_{\text{Hall}} = \frac{\partial}{\partial x}\left(\frac{\eta_H \mu_0}{|B|}(J_x B_z - J_z B_x)\right) + \frac{\partial}{\partial y}\left(\frac{\eta_H \mu_0}{|B|}(J_y B_z - J_z B_y)\right), \tag{3.13c}$$

and for the Biermann battery term:

$$\left(\frac{\partial B_x}{\partial t}\right)_{\text{Batt}} = \frac{\partial}{\partial y}\left(\frac{\eta_B \mu_0}{|B|}\frac{\partial p_e}{\partial z}\right) - \frac{\partial}{\partial z}\left(\frac{\eta_B \mu_0}{|B|}\frac{\partial p_e}{\partial y}\right), \tag{3.14a}$$

$$\left(\frac{\partial B_y}{\partial t}\right)_{\text{Batt}} = -\frac{\partial}{\partial x}\left(\frac{\eta_B \mu_0}{|B|}\frac{\partial p_e}{\partial z}\right) + \frac{\partial}{\partial z}\left(\frac{\eta_B \mu_0}{|B|}\frac{\partial p_e}{\partial x}\right), \tag{3.14b}$$

$$\left(\frac{\partial B_z}{\partial t}\right)_{\text{Batt}} = \frac{\partial}{\partial x}\left(\frac{\eta_B \mu_0}{|B|}\frac{\partial p_e}{\partial y}\right) - \frac{\partial}{\partial y}\left(\frac{\eta_B \mu_0}{|B|}\frac{\partial p_e}{\partial x}\right). \tag{3.14c}$$

Where for simplicity the vector components in both the energy and induction equations were written in a compact form as: $B_l = B_{0l} + B_{1l}$, $J_{\perp l} = J_{\perp 0l} + J_{\perp 1l}$, and $J_l = J_{0l} + J_{1l}$ with $l = x, y, z$.

The artificial diffusion terms, with a physical counterpart except for the Eq. (3.1), were added for numerical stability reasons following Vögler et al. (2005) and will be treated in Subsection 3.5. In some situations, such as when the wavelength is much smaller than the photon mean free path (optically thin mediums), the radiative term Q_{rad} can be calculated through Newton's cooling law

$$Q_{\text{rad}} = -c_v \rho_0 \frac{T_1}{\tau_R}, \quad c_v = \frac{1}{\gamma - 1}\frac{\mathbb{R}}{\mu}, \tag{3.15}$$

where τ_R is the radiative relaxation time. In a more realistic situations, Q_{rad} is computed using the radiative transfer module, see Section 3.9. Finally, the system is closed either with an ideal equation of state or a realistic one in thermodynamical equilibrium based in precalculated tables, see Section 3.8.

3.3 Spatial integration

The current version of the code works with a centered sixth order accurate spatial derivatives using six grid points. First the quantity is interpolated, giving us the result at mid-point.

$$f_{i+1/2} = \frac{3}{265}(f_{i+3} + f_{i-2}) - \frac{25}{256}(f_{i+2} + f_{i-1}) + \frac{75}{128}(f_{i+1} + f_i). \tag{3.16}$$

Then, doing the numerical derivative, the result is returned back to the original spatial centered mesh.

$$\frac{\partial f_i}{\partial x} = \frac{3}{640}\frac{(f_{i+5/2} - f_{i-5/2})}{\Delta x} - \frac{25}{384}\frac{(f_{i+5/2} - f_{i-3/2})}{\Delta x} + \frac{75}{64}\frac{(f_{i+3/2} - f_{i+1/2})}{\Delta x} \,. \tag{3.17}$$

This can be done because the interpolation and differentiation operators are computationally equivalent. The reason of choosing a fifth order interpolation and a sixth order derivative is based on tests done by Nordlund & Galsgaard (1995), which shown how the noise level is enhanced at wavenumbers close to the Nyquist frequency using lower order operators. As a consequence, a lower diffusion coefficients can be used.

3.4 Temporal integration

To advance the solution in time an explicit fourth order Runge-Kutta (RK) scheme is used in MANCHA3D using the formulation well tested by Vögler et al. (2005), Khomenko & Collados (2006) or Felipe et al. (2010) among others. The system of equations written in conservative form can be schematically represented as

$$\frac{\partial \mathbf{U}}{\partial t} = \mathcal{R}(\mathbf{U}) = -\nabla \mathbf{F}(\mathbf{U}) + \mathbf{S}(\mathbf{U}) \,, \tag{3.18}$$

where $\mathcal{R}(\mathbf{U})$ represents an operator formed by the sum of the spatial derivatives of fluxes $\mathbf{F}(\mathbf{U})$ and the source terms, $\mathbf{S}(\mathbf{U})$. The vector $\mathbf{U} = \mathbf{U}_0 + \mathbf{U}_1$, is the set of variables in the equations: $[\rho, \rho\mathbf{v}, \mathbf{B}, e](\mathbf{r}, t)$.

The next time step is calculated using an explicit RK scheme that can be written as

$$\mathbf{U}^{(\frac{1}{4})} = \mathbf{U}^{(0)} + \frac{\Delta t}{4}\mathcal{R}(\mathbf{U}^{(0)}) \,, \tag{3.19a}$$

$$\mathbf{U}^{(\frac{1}{3})} = \mathbf{U}^{(0)} + \frac{\Delta t}{3}\mathcal{R}(\mathbf{U}^{(\frac{1}{4})}) \,, \tag{3.19b}$$

$$\mathbf{U}^{(\frac{1}{2})} = \mathbf{U}^{(0)} + \frac{\Delta t}{2}\mathcal{R}(\mathbf{U}^{(\frac{1}{3})}) \,, \tag{3.19c}$$

$$\mathbf{U}^{(1)} = \mathbf{U}^{(0)} + \Delta t\mathcal{R}(\mathbf{U}^{(\frac{1}{2})}) \,, \tag{3.19d}$$

where $\mathbf{U}^{(0)}$ corresponds to the solution at t_0 and $\mathbf{U}^{(1)}$ corresponds to the solution at $t_1 = t_0 + \Delta t$, with Δt given by the Courant, Friedrichs and Lewy (CFL) condition (Courant et al. 1928), see Section 3.6.

Since MANCHA3D solves the non-linear MHD equations for perturbations, the RK scheme only advances in time the perturbed quantities $\mathbf{U}_1 = [\rho_1, \rho\mathbf{v}, \mathbf{B}_1, e_1](\mathbf{r}, t)$.

3.5 Artificial diffusivity

Due to the high Reynolds and magnetic Reynolds numbers existing in the solar atmosphere, the characteristic lengths of the diffusivity are not resolved, and perturbations at such scales have to be dumped to avoid numerical noise. To avoid the growth of the noise, numerical viscosity and diffusivity have to be included. The code has implemented the numerical viscosity and diffusivity coefficients as a sum of three contributions, a shock-resolving part (3.21), a hyperdiffusive part (3.22) and a constant contribution (3.23).

$$\nu_l(\mathbf{U}_1) = \nu_l^{\text{shk}} + \nu_l^{\text{hyp}}(\mathbf{U}_1) + \nu_l^{\text{cnt}} \,, \tag{3.20}$$

$$\nu_l^{\text{shk}} = \begin{cases} C_{\text{shk}} \cdot \Delta x_l^2 \cdot |\nabla \cdot \mathbf{U}_1| & \nabla \cdot \mathbf{U}_1 < 0 \\ 0 & \nabla \cdot \mathbf{U}_1 \geq 0 \end{cases} \,, \tag{3.21}$$

$$\nu_l^{\rm hyp}(\mathbf{U}_1) = C_{\rm hyp}\cdot c_{\rm tot}\cdot \Delta x_l \cdot \frac{\max_3 \Delta_l^3 \mathbf{U}_1}{\max_3 \Delta_l^1 \mathbf{U}_1}\,, \tag{3.22}$$

$$\nu_l^{\rm cnt} = C_{\rm cnt}\cdot (c_{\rm s}+v_{\rm A})\cdot \Delta x_l \cdot F(x,y,z)\,, \tag{3.23}$$

where $l = x, y, z$ and $c_{\rm tot}$ is the sum of flow velocity, sound speed and Alfvén speed,

$$c_{\rm tot} = v_{\rm flow} + c_{\rm s} + v_{\rm A}\,, \tag{3.24}$$

and where $\Delta_l^1\mathbf{U}_1$ and $\Delta_l^3\mathbf{U}_1$ are given by

$$(\Delta_l^1\mathbf{U}_1)_{i+\frac{1}{2}} = |(\mathbf{U}_1)_{i+1} - (\mathbf{U}_1)_i|\,, \tag{3.25}$$

$$(\Delta_l^3\mathbf{U}_1)_{i+\frac{1}{2}} = |3\,[(\mathbf{U}_1)_{i+1} - (\mathbf{U}_1)_i] - [(\mathbf{U}_1)_{i+2} - (\mathbf{U}_1)_{i-1}]|\,, \tag{3.26}$$

representing the first and third absolute differences of $\mathbf{U}_1$.
Once these coefficients are calculated, they must be introduced into the MHD equations (3.1), (3.2), (3.3), and (3.8) as a numerical implementation of the diffusive terms denoted with subscript "diff".

$$\left(\frac{\partial \rho_1}{\partial t}\right)_{\rm diff} = \sum_l \frac{\partial}{\partial x_l}\left(\nu_{x_l}(\rho_1)\frac{\partial \rho_1}{\partial x_l}\right)\,, \tag{3.27a}$$

$$\left(\frac{\partial \rho \mathbf{v}_1}{\partial t}\right)_{\rm diff} = \nabla\cdot\overline{\overline{\tau}}\,, \tag{3.27b}$$

$$\left(\frac{\partial e_1}{\partial t}\right)_{\rm diff} = \nabla\cdot(\mathbf{v}_1\overline{\overline{\tau}}) + \nabla\cdot(\mathbf{B}_1\times\boldsymbol{\mathcal{E}})\,, \tag{3.27c}$$

$$\left(\frac{\partial \mathbf{B}_1}{\partial t}\right)_{\rm diff} = -\nabla\times\boldsymbol{\mathcal{E}}\,, \tag{3.27d}$$

(3.27e)

where $\overline{\overline{\tau}}$ is the stress tensor

$$\tau_{kl} = \frac{1}{2}(\rho_0+\rho_1)\left(\nu_k(v_{1l})\frac{\partial v_{1l}}{\partial x_k} + \nu_l(v_{1k})\frac{\partial v_{1k}}{\partial x_l}\right)\,, \tag{3.28}$$

and $\boldsymbol{\mathcal{E}}$, is the vector quantity defined as

$$\boldsymbol{\mathcal{E}} = \begin{bmatrix} \nu_y(B_{1z})\partial_y B_{1z} - \nu_z(B_{1y})\partial_z B_{1y} \\ \nu_z(B_{1x})\partial_z B_{1x} - \nu_x(B_{1z})\partial_x B_{1z} \\ \nu_x(B_{1y})\partial_x B_{1y} - \nu_y(B_{1x})\partial_y B_{1x} \end{bmatrix}\,. \tag{3.29}$$

All mixed derivative, as those present in Eq. (3.27a), are done using the spatial integration of Section 3.3 twice.

3.6 Time step

The CFL criterion ensures that in a time step Δt the information transported by waves or flows travels a distance not bigger than the mesh size. The time step must be smaller than the advective time step ($\Delta t_{\rm adv}$) and the diffusion time step ($\Delta t_{\rm diff}$).

$$\Delta t_{\rm adv} = C_{\rm adv}\cdot\frac{1}{\max(c_s, v_A)}\sqrt{\left(\frac{1}{\Delta x^2}+\frac{1}{\Delta y^2}+\frac{1}{\Delta z^2}\right)^{-1}}\,, \tag{3.30}$$

$$\Delta t_{\rm diff} = C_{\rm diff} \cdot \min\left(\frac{\Delta x^2}{\nu_x}, \frac{\Delta y^2}{\nu_y}, \frac{\Delta z^2}{\nu_z}\right) , \tag{3.31}$$

where $C_{\rm adv}$ and $C_{\rm diff}$ are two constants in the interval (0,1].

When physical non-ideal terms are considered, the time step has to be the minimum of all the time steps, both advective, physical and numerical diffusive, and viscose time steps given by the Equations (3.32), (3.33), and (3.34).

$$\Delta t_{\rm Ohmic} = C_{\rm Ohmic} \cdot \frac{\min(\Delta x^2, \Delta y^2, \Delta z^2)}{\eta} , \tag{3.32}$$

$$\Delta t_{\rm Ambi} = C_{\rm Ambi} \cdot \frac{\min(\Delta x^2, \Delta y^2, \Delta z^2)}{\eta_A} , \tag{3.33}$$

$$\Delta t_{\rm Hall} = C_{\rm Hall} \cdot \frac{\min(\Delta x^2, \Delta y^2, \Delta z^2)}{\eta_H} , \tag{3.34}$$

where $C_{\rm Ohmic}$, $C_{\rm Ambi}$, and $C_{\rm Hall}$ are constants in the interval (0,1]. Due to by definition $\eta_H = \eta_B$, the Biermann battery time step results equal to the Hall time step, $\Delta t_{\rm Batt} = \Delta t_{\rm Hall}$, and then

$$\Delta t = \min\left(\Delta_{\rm adv}, \Delta t_{\rm diff}, \Delta t_{\rm Ohmic}, \Delta t_{\rm Ambi}, \Delta t_{\rm Hall}\right) . \tag{3.35}$$

Usually, the restrictions from Hall and Ohmic terms are negligible for the spatial steps considered and can be dropped out from Eq. (3.35).

3.7 Filtering

Following the suggestions of Hesthaven (1998) to improve the stability of the code, a filter is implemented in the current version of MANCHA3D using the method described by Parchevsky & Kosovichev (2007). This filter helps to reduce the strength of the artificial diffusion terms since those terms modify the amplitude of the perturbation.

$$u_{\rm filt} = u(x_l) - D(x_l) = u(x_l) - C_{\rm filt} \cdot \sum_{m=-3}^{3} d_m u(x_l + m\Delta x_l) , \tag{3.36}$$

where the filter can be applied to any spatial direction. $C_{\rm filt}$ is the filter strength constant, taking values into the interval (0,1]. $D(x_l)$ is a damping function where the coefficients d_m are selected in the Fourier transform space according to the filter response function $G(k)$, which relates the original transform function $g(k)$ to the filtered transform function, as $g_{\rm filt} = G(k)g(k)$,

$$G(k\Delta x) = 1 - C_{\rm filt} \cdot \sum_{m=-3}^{3} d_m e^{imk\Delta x} = 1 - C_{\rm filt} \cdot \sin^6\left(\frac{k\Delta x}{2}\right) . \tag{3.37}$$

The coefficients d_m have the values:

$$d_0 = \frac{5}{16}, \qquad d_1 = d_{-1} = -\frac{15}{64}, \qquad d_2 = d_{-2} = \frac{3}{32}, \qquad d_3 = d_{-3} = -\frac{1}{64} . \tag{3.38}$$

3.8 Realistic equation of state

The equation of state (EOS) implemented in MANCHA3D is in thermodynamical equilibrium and considers a solar like chemical mixture based on the work of Anders & Grevesse (1989). It also considers the effects of the first and second atomic ionization for all the elements with an atomic number $Z \leq 92$ and the formation of hydrogen molecules. Based on Saha equation, the method described by Mihalas (1967) is followed to precalculate a series of tables for internal energy, density, and electron pressure as a function of the thermodynamical variables (p, T), which form a grid where those tabulated variables can be interpolated during simulations. This procedure allows an efficient conversion between variables and makes faster the computing of non-ideal terms. There is a freedom of using different EOS with different chemical composition or adding terms like the electron degeneration, that would be relevant in other simulations.

3.9 Numerical radiative transfer

In the solar atmosphere we can assume that the speed of light is much bigger than the flow velocities, meaning that the radiation field at a given time only depends of the atmospheric state at that given time. This means that the emission and absorption functions can be calculated based on the previous time step, allowing us to solve the radiative transfer (RT) equation (2.11) explicitly.

MANCHA3D is capable of solving the non-gray RT equation using the short characteristic method described by Olson & Kunasz (1987) to compute the losses term $Q_{\rm rad}$ assuming local thermodynamic equilibrium (LTE). The solver discretizes the formal solution of the RT equation in such a way that reduces the computation time.

The wavelength treatment is done following the multigroup method described by Nordlund (1982), also known as opacity binning method. This method sorts and groups the frequencies into small packages called bins according to the strength of the corresponding opacity. For each bin the RT is solved using an averaged opacity obtained from an opacity distribution function and continuum opacities from the ATLAS9 stellar atmosphere catalog by Kurucz (1993). In order to calculate the intensity for a given frequency and direction, the integration is done over the bins in frequency, and over the directions, using a quadrature with three rays per octant, thereby the computational time is reduced drastically. When only one bin is used the method simplifies into the gray approximation. For more details, Vögler et al. (2004) offers a description of the opacity binning method, as implemented in MANCHA3D (Khomenko et al. 2018).

The LTE approximation limits the height above the photosphere due to the assumptions underlying LTE. In the optically thin corona, $Q_{\rm rad}$ can be computed using the Equation (3.15) of Newtonian cooling.

3.10 Boundary conditions

3.10.1 Non-reflective boundary condition

Using the equations for perturbations instead the full variable equations it is easy to implement particular non-reflective boundary conditions at all the sides of the numerical box to avoid incoming perturbations due to reflexions. This boundary condition is know as perfectly matched layer (PML) and was developed by Berenger (1994, 1996) for Maxwell's equations and later applied to the Euler's equations by Hu (1996, 2001). The idea to use PML was extended to the MHD equations by Parchevsky & Kosovichev (2009) and was well tested by them.

The main idea of this method is to split each of the conservation equation into the three Cartesian direction and apply a damping factor individually to each of them, thus the Equation (3.18) can be written for the perturbations, $\mathbf{U}_1 = \mathbf{U}_{1,x} + \mathbf{U}_{1,y} + \mathbf{U}_{1,z}$, as

$$\frac{\partial \mathbf{U}_1}{\partial t} + \frac{\partial \mathbf{F}_x(\mathbf{U}_1)}{\partial x} + \frac{\partial \mathbf{F}_y(\mathbf{U}_1)}{\partial y} + \frac{\partial \mathbf{F}_z(\mathbf{U}_1)}{\partial z} = \mathbf{S}(\mathbf{U}_1)\,, \tag{3.39}$$

where applying the splitting results

$$\frac{\partial \mathbf{U}_{1,x}}{\partial t} + \frac{\partial \mathbf{F}_x(\mathbf{U}_1)}{\partial x} + \sigma_x \mathbf{U}_{1,x} = \mathbf{S}_x(\mathbf{U}_1)\,, \tag{3.40a}$$
$$\frac{\partial \mathbf{U}_{1,y}}{\partial t} + \frac{\partial \mathbf{F}_y(\mathbf{U}_1)}{\partial y} + \sigma_y \mathbf{U}_{1,y} = \mathbf{S}_y(\mathbf{U}_1)\,, \tag{3.40b}$$
$$\frac{\partial \mathbf{U}_{1,z}}{\partial t} + \frac{\partial \mathbf{F}_z(\mathbf{U}_1)}{\partial z} + \sigma_z \mathbf{U}_{1,z} = \mathbf{S}_z(\mathbf{U}_1)\,, \tag{3.40c}$$

where $\mathbf{U}_{1,l}$ is a vector contained the perturbation of the conserved variables, $\mathbf{F}_l$ are the fluxes of those variables, and $\mathbf{S}_l$ are the source terms in the direction $l = x, y, z$. The absorption coefficients σ_l are calculate as

$$\sigma_l = \frac{A_l}{\Delta x_l} \cdot \left(\frac{x_l - x_l^{\mathrm{PML}}}{x_l^{\mathrm{PML}}} \right)^2\,, \tag{3.41}$$

resulting in a smooth function going from small values at the interface in each direction to the value given by the PML strength coefficients A_l at the width of the PML in each direction, x_l^{PML}. This is done to avoid reflections due to strong variation at the boundary.

Sponge PML

PML damps well perturbations in the normal direction to the boundary, however perturbations in the tangential direction remain undamped. Under some conditions (e.g. inclined field in low-β plasma) it can introduce some instabilities or numerical noise within the PML domain. Those instabilities some times can grow and compromise the stability of the simulation. This problem is specially present in the experiments of Chapter 5 when the waves had a certain incident angle α of around 35 to 55 degrees. It uses to appear as a moving chess board pattern along the PML domain. After some tests, it was observed that instead of applying the PML following the Eqs. (3.40), was better option to applied each of the directional absorption coefficients over all the split variables into the PML domain, as the Eqs. (3.42) shown. We have called this modification "sponge-PML" and it have increased significantly the numerical stability of these experiments without affecting particularly the solution into the numerical domain.

$$\frac{\partial \mathbf{U}_{1,x}}{\partial t} + \frac{\partial \mathbf{F}_x(\mathbf{U}_1)}{\partial x} + \sigma_x \mathbf{U}_1 = \mathbf{S}_x(\mathbf{U}_1)\,, \tag{3.42a}$$
$$\frac{\partial \mathbf{U}_{1,y}}{\partial t} + \frac{\partial \mathbf{F}_y(\mathbf{U}_1)}{\partial y} + \sigma_y \mathbf{U}_1 = \mathbf{S}_y(\mathbf{U}_1)\,, \tag{3.42b}$$
$$\frac{\partial \mathbf{U}_{1,z}}{\partial t} + \frac{\partial \mathbf{F}_z(\mathbf{U}_1)}{\partial z} + \sigma_z \mathbf{U}_1 = \mathbf{S}_z(\mathbf{U}_1)\,. \tag{3.42c}$$

3.10.2 Convection boundary condition

In order to get a stable convection regime, a set of upper and bottom boundary conditions are provided externally since they are not include by default into the code.

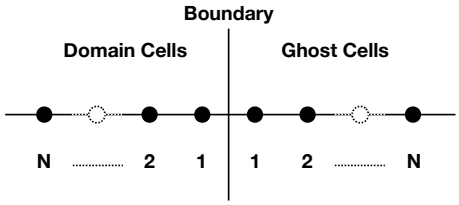

FIGURE 3.1— Boundary condition cells notation.

Top boundary

The upper boundary is set closed to flows with a stress-free condition for the horizontal components of the velocity field. Physically this implies that vertical convective fluxes vanish at the boundary.

$$v_z\big|_{\rm top} \equiv 0, \qquad \left.\frac{\partial \rho}{\partial z}\right|_{\rm top} \equiv 0, \qquad \left.\frac{\partial e_{\rm int}}{\partial z}\right|_{\rm top} \equiv 0\,. \tag{3.43}$$

The stress-free boundary:

$$\left.\frac{\partial v_x}{\partial z}\right|_{\rm top} \equiv 0, \qquad \left.\frac{\partial v_z}{\partial z}\right|_{\rm top} \equiv 0\,. \tag{3.44}$$

For the magnetic field vertical field lines are imposed:

$$B_{x,y}\big|_{\rm top} \equiv 0 \xrightarrow{\nabla\cdot\mathbf{B}=0} \left.\frac{\partial B_z}{\partial z}\right|_{\rm top} \equiv 0\,. \tag{3.45}$$

This set of conditions allows free movement of the field lines; numerically it can be written as:

$$[v_z]_j^{\rm ghost} = -[v_z]_j^{\rm domain}, \qquad [\rho]_j^{\rm ghost} = [\rho]_j^{\rm domain}, \qquad [e_{\rm int}]_j^{\rm ghost} = [e_{\rm int}]_j^{\rm domain}\,, \tag{3.46}$$

$$[v_x]_j^{\rm ghost} = [v_x]_j^{\rm domain}, \qquad [v_y]_j^{\rm ghost} = -[v_y]_j^{\rm domain}\,, \tag{3.47}$$

$$[B_z]_j^{\rm ghost} = [B_z]_j^{\rm domain}, \qquad [B_{x,y}]_j^{\rm ghost} = -[B_{x,y}]_j^{\rm domain}\,, \tag{3.48}$$

with $j = 1, 2, \ldots, n_{\rm ghost}$, where $n_{\rm ghost}$ is the number of ghost cells outside the numerical domain.

Bottom boundary

The lower boundary is located inside the convective zone and should allow free movement of fluid trough it as an open boundary. This requires knowing the physical conditions outside the numerical domain which are unknown and then must be replaced with reasonable information. Considering that the magneto-acoustic speed is higher than the fluid speed, that is, convective motion are slow enough, it is possible to assume that the total pressure (3.49) is constant across this boundary (3.50),

$$p_{\rm tot} = p + \frac{\mathbf{B}^2}{2\mu_0}\,, \tag{3.49}$$

$$p_{\rm tot}\big|_{\rm bot} = p_{\rm tot,0}\ , \tag{3.50}$$

and then the gas pressure at the boundary will be:

$$p\big|_{\rm bot} = p_0 = p_{\rm tot,0} - \frac{\mathbf{B}^2}{2\mu_0} \implies [p]_j^{\rm ghost} = -[p]_j^{\rm domain}\ . \tag{3.51}$$

At this boundary, the downflows ($v_z < 0$) and upflows ($v_z > 0$) should have a smooth behavior going in and out of the domain more or less homogeneously. This can be achieved by considering the conditions (3.52) for velocity, and since at this depth the radiative exchange and thermal diffusion are negligible, both flows can be considered isentropic, condition (3.53), and thus it is possible to determine the values of the internal energy per unit of mass at the ghost cells considering the relation $\varepsilon_0 = e_{\rm int}/\rho \propto p^\xi$ for one dimensional models (e.g. Spruit 1974). For this expression, Vögler et al. (2005) use a value of $\xi = 0.25$ that correspond to a depth of 800–1000 km in the convection zone for the Spruit (1974) model. This value is an approximation since for a partially ionized gas, this parameter, has a dependency on other thermodynamical variables.

$$\begin{cases} \frac{\partial v_x}{\partial z}\big|_{\rm bot} = \frac{\partial v_y}{\partial z}\Big|_{\rm bot} = \frac{\partial v_z}{\partial z}\big|_{\rm bot} \equiv 0 & v_z < 0\ , \\ v_x\big|_{\rm bot} = v_y\big|_{\rm bot} \equiv 0, \qquad \frac{\partial v_z}{\partial z}\big|_{\rm bot} \equiv 0 & v_z > 0\ , \end{cases} \tag{3.52}$$

$$\frac{\partial s}{\partial z}\Big|_{\rm bot} \equiv 0\ . \tag{3.53}$$

For downflows, the condition (3.53), where s is the entropy density per unit mass, numerically results in

$$\left[\frac{e_{\rm int}}{\rho}\right]_j^{\rm ghost} = \left[\frac{e_{\rm int}}{\rho}\right]_j^{\rm domain} \cdot \left(\frac{[p]_j^{\rm ghost}}{[p]_j^{\rm domain}}\right)^\xi\ , \tag{3.54}$$

where the ghost cell values for density are obtained by the interpolation of EOS tables to get the values for the internal energy density.

For the upflows, are assumed constant values for the internal energy density per unit of mass across the lower boundary (ϵ_0) and pressure (p_0). These two assumptions set the entropy density per unit of mass at the bottom boundary to a constant value (s_0) and then, the condition (3.53), results in

$$\left[\frac{e_{\rm int}}{\rho}\right]_j^{\rm ghost} = \left[\frac{e_{\rm int,0}}{\rho_0}\right]_j^{\rm domain} \cdot \left(\frac{[p]_j^{\rm ghost}}{p_0}\right)^\xi = \epsilon_0 \cdot \left(\frac{[p]_j^{\rm ghost}}{p_0}\right)^\xi\ . \tag{3.55}$$

This constant value for the internal energy density can be used to control the vertical energy flux across the boundary and the domain to maintain a solar like energy flux ($F_\odot = 6.34 \times 10^{10}$ erg s^{-1} cm^{-2}) at the top boundary. The values of ε_0 at the bottom boundary, along the simulation time, must be adjusted as a function of current energy flux values at the top ($F_{\rm top}$). This adjustment is done in the Kelvin-Helmholtz timescale $\tau_{\rm KH}$.

$$\varepsilon_0^{t_1} = \varepsilon_0^{t_0} \cdot \left(1 + \frac{\Delta t}{\tau_{KH}} \cdot \frac{F_\odot - F_{\rm top}}{F_\odot}\right); \qquad \tau_{\rm KH} = \frac{\int_{\rm box} e_{\rm int} dV}{\int_{\rm top} F_\odot dx dy}\ . \tag{3.56}$$

Since the strength of the magnetic field affects the convective motion, on the lower boundary the value of ε_0 changes. For this reason, for the upflows we set a magnetic field threshold of $B_{\rm t} = 800$ G and treat the regions with $v_z \geq 0$ and $|\mathbf{B}| > B_t$ as the downflows by using the Eq. (3.54) instead of Eq. (3.55).

Mass control

The last step is to take care of the possible variations in the mass flows of our computational domain. Since the domain can only contain a limited number or convective cells, statistical fluctuations in the total mass can be significant. To control this, the condition of constant pressure at the bottom boundary, Eq. (3.50), can be used. This correction ($\delta M_{\rm corr}$), in order to be smooth, is balanced in a timescale of $\tau_{\rm mass} \approx 30$ s, thus at each time step results in,

$$\delta M_{\rm corr} = \delta M \cdot \frac{\Delta t}{\tau_{\rm mass}} = \frac{M - M_0}{M_0} \cdot \frac{\Delta t}{\tau_{\rm mass}} \,, \tag{3.57}$$

where M is the total mass at the current time and M_0 the initial total mass. This expression guaranty that the total pressure ($p_{\rm tot}$) has a smooth variation across the numerical box based on a previous time step. The pressure in the upflow region results

$$p_{\rm up} = p_{\rm tot,0} + \Delta p \,, \tag{3.58}$$

having an associated change in density which induce a change in the vertical mass flux at the bottom allowing to control the influx of mass. This new value of $p_{\rm up}$ will be used at the next step as a starting value of $p_{\rm tot,0}$ meaning that the downflow region has a lag of one time step behind the adjusted pressure. The value of Δp is found iteratively and since it is very small, it does not lead to the generation of important horizontal pressure gradients.

3.10.3 Periodic boundary condition

The periodicity of the numerical domain is an intrinsic characteristic of the spatial derivative if nothing else is specified.

4

Super Time-Stepping in MANCHA3D

Talk is cheap. Show me the code.

- Linus Torvalds, 2000.

As was discusses in the previous chapters, this thesis uses a single-fluid approximation, which is valid for the case of a strongly coupled collisional media, such as solar photosphere and low chromosphere. Under the single-fluid formalism the main non-ideal effects are described by a series of extra terms in the generalized induction equation and in the energy conservation equation. These effects are: Ohmic diffusion, ambipolar diffusion, the Hall effect, and the Biermann battery effect. From the point of view of the numerical solution of the single-fluid equations, when ambipolar diffusion or Hall effects dominate, it can introduce severe restrictions on the integration time step and can compromise the stability of the numerical scheme. In this Chapter we introduce two numerical schemes to overcome those limitations. The first of them is known as super time-stepping (STS) and is designed to overcome the limitations imposed when the ambipolar diffusion term is dominant. The second scheme is called the Hall diffusion scheme (HDS) and is used when the Hall term becomes dominant. These two numerical techniques can be used together by applying Strang operator splitting. The content of this Chapter have been published and describes the implementation of the STS and HDS schemes in the single-fluid code MANCHA3D (Gonzalez-Morales et al. 2018). The validation for each of these schemes is provided by comparing the analytical solution with the numerical one for a suite of numerical tests.

4.1 Introduction

The importance of the non-ideal effects, as those introduced in Chapter 2, can be evaluated by examining the ratio between the cyclotron frequency and the collisional frequencies. In the photosphere, the cyclotron frequency can exceed the collisional one in strongly magnetized areas such as flux tubes and sunspots, while in the chromosphere this happens over most of its volume even in regions with a weaker magnetic field (Khomenko et al. 2014). It can be expected that in such conditions the neutral and charged particles behave in a different way, with direct repercussions on the plasma dynamics and energy exchange. A recent review of the behavior of partially ionized plasmas in different astrophysical conditions is provided by Ballester et al. (2018).

Mathematically, the treatment of partially ionized plasmas depends on the degree of collisional coupling. The most widely used formalisms are either a two-fluid or single-fluid approach, see the Chapter

2, the recent discussion done by Khomenko et al. (2014), or Ballester et al. (2018) for more details. The two-fluid formalism, including the treatment of ionization-recombination terms was discussed by Meier & Shumlak (2012). While the single-fluid formalism yields a less detailed description, it is numerically more efficient for strongly stratified solar plasma, and therefore it has been adopted in several numerical codes that aim at realistic simulations of the solar atmosphere such as MURaM (Vögler et al. 2005), *Bifrost* (Gudiksen et al. 2011), and Mancha3D [1] (Felipe et al. 2010), the latter being the one used in the current study and explained in detail in Chapter 3. The single-fluid formalism has an advantage since numerically problematic collisional terms (both elastic collisions and ionization-recombination) do not appear explicitly in the equations, greatly simplifying the modeling. For the range of collisional frequencies typical for the solar photosphere and chromosphere, these collisional terms require extremely short time steps, unsuitable for most frequently used explicit numerical codes. In the solar case, the single-fluid formalism can safely be used for the modeling of the dense and collisional photosphere and low chromosphere, for the typical time scales of interest (Zaqarashvili et al. 2011). For both the single and two-fluid formalisms the generalized Ohm's law (Cowling 1957) has to be used to describe the behavior of electric currents. The generalized Ohm's law has a series of additional terms derived from the presence of neutrals, while other standard terms have slightly modified expressions (Khomenko et al. 2014). As a consequence, there appear additional terms in the induction and in the energy conservation equations. The leading non-ideal terms in the single-fluid formalism, as was commented in Chapter 2 are: the ambipolar diffusion (related to neutrals), and the Hall term and the Biermann battery term (related to charges but modified by collisions with neutrals).

In an astrophysical context, ambipolar diffusion is envisaged as a process of diffusion suffered by the magnetic field due to collisions between neutral and charged particles, the latter being frozen into the field. Ambipolar diffusion helps converting magnetic energy into thermal energy on scales that are typically much faster than classical Ohmic diffusion. For the Sun, it has been demonstrated that the ambipolar diffusion is orders of magnitude larger than Ohmic diffusion in the chromospheric layers, therefore greatly contributing to chromospheric heating via Joule dissipation (Khomenko & Collados 2012; Martínez-Sykora et al. 2012; Priest 2014). In the two-fluid treatment, the energy equation for the charged fluid also has a Joule heating term, similar to the single-fluid case, and the expression for the electric field comes from the generalized Ohm's law (see, e.g., Khomenko et al. 2014; Ballester et al. 2018). It is interesting to note, however, that ambipolar diffusion term is not explicitly present in the two-fluid Ohm's law, and in the energy conservation equation in the two-fluid treatment, and the corresponding effect is expressed via explicit ion-neutral collisional terms.

The Hall effect appears when ions decouple from the magnetic field while electrons remain attached to it. In a fully ionized plasma ions decouple from the magnetic field due to the difference between the inertia of ions and electrons, and this decoupling typically happens for processes at high frequencies. In weakly ionised plasmas, however, the ions can become detached from the magnetic field due to collisions with neutrals, leading to a similar effect. The spatial and temporal scales of the Hall effect in partially ionized plasmas are different from those in fully ionized plasmas, but the dynamics are similar in both cases. The Hall term is not dissipative, so it does not contribute to the heating of the environment, however it does redistribute magnetic energy in the system. Therefore, the Hall effect has an important role at many scales, from laboratory to astrophysical plasmas, while ambipolar diffusion is typically only important at low ionization fractions (Parker 2007; Pandey & Wardle 2008; Priest 2014; Ballester et al. 2018).

The Biermann battery effect is somewhat different to the two non-ideal effects discussed above. Its magnitude in the solar case is rather small and it is usually ignored as it is not deemed important.

[1] Recently Popescu Braileanu et al. (2019a) have implemented a semi-implicit algorithm into Mancha3D code to solve the MHD equations for a purely hydrogen plasma under the two-fluid formalism considering collisional coupling between neutrals and charges.

But recently Khomenko et al. (2017) have shown that this term is able to seed the magnetic field for the local solar dynamo. In the present work we will consider this term for completeness.

From a numerical point of view, the battery term only introduces a small source term into the hyperbolic system of equations of single-fluid MHD. So long as this source term is small, it is not necessary to introduce a time step restriction based on it for either accuracy or stability reasons. However, the ambipolar term is diffusive (i.e., parabolic), and the Hall term is dispersive. These two latter terms introduce important restrictions into the integration time step and into the stability of explicit numerical schemes, which are frequently used in hydrodynamic codes solving hyperbolic equations.

This Chapter presents a new numerical scheme aiming to overcome these restrictions. This scheme is implemented as separate modules in the existing single-fluid radiative MHD code MANCHA3D (Khomenko & Collados 2006, 2012; Felipe et al. 2010). The proposed scheme is relatively easy to add into an existing explicit numerical scheme, which allows us to keep all the benefits and flexibility of the explicit approach. We also provide a suite of numerical tests to verify the newly implemented modules and to check their order of accuracy.

This Chapter is organized as follows. In Section 4.2 we show the set of equations corresponding to a single fluid description with a generalized Ohm's law. In Section 4.3 we present the details of the new numerical scheme introduced here. In Section 4.4 we show tests demonstrating the feasibility and reliability of the new scheme introduced, while in Section 4.5 a brief summary is presented.

4.2 Equations

As discussed in the Section 4.1, the peculiarity of solar plasma in the photosphere and in the low chromosphere is that, while being only weakly ionized, it is still very dense and, therefore, collisions play an important role in coupling all plasma and neutral components. Since typically the scales of interest are significantly larger than collisional scales (see Khomenko et al. 2014), the most efficient approach for the mathematical treatment of such plasma is a single-fluid quasi-MHD formalism. The derivation of conservation equations and the generalized induction equation for such a case was discussed in Chapter 2. MANCHA3D solves the following system of equations,

$$\frac{\partial \rho}{\partial t} + \nabla \cdot (\rho \mathbf{v}) = 0 \,, \tag{4.1}$$

$$\frac{\partial (\rho \mathbf{v})}{\partial t} + \nabla \cdot \left[\rho \mathbf{v}\mathbf{v} + \left(p + \frac{\mathbf{B}^2}{2\mu_0} \right) \mathbf{I} - \frac{\mathbf{B}\mathbf{B}}{\mu_0} \right] = \rho \mathbf{g} \,, \tag{4.2}$$

$$\frac{\partial \mathbf{B}}{\partial t} = \nabla \times \left[(\mathbf{v} \times \mathbf{B}) - \eta \mu_0 \mathbf{J} - \eta_H \frac{\mu_0}{|B|} (\mathbf{J} \times \mathbf{B}) + \eta_A \frac{\mu_0}{|B|^2} \left[(\mathbf{J} \times \mathbf{B}) \times \mathbf{B} \right] + \eta_B \frac{\mu_0}{|B|} \nabla p_e \right] \,, \tag{4.3}$$

$$\begin{aligned} \frac{\partial e}{\partial t} + \nabla \cdot \left[\frac{\rho \mathbf{v}^2}{2} \mathbf{v} + \frac{\gamma p}{\gamma - 1} \mathbf{v} + \frac{1}{\mu_0} \nabla \cdot [\mathbf{B} \times (\mathbf{v} \times \mathbf{B})] \right] = \rho \mathbf{v} \cdot \mathbf{g} + \\ + \nabla \cdot [\mathbf{B} \times (\eta + \eta_A) \mathbf{J}_\perp] + \nabla \cdot \left[\eta_B \frac{\nabla p_e \times \mathbf{B}}{|B|} \right] \,, \end{aligned} \tag{4.4}$$

where the non-ideal coefficients η, η_H, η_A, η_B are defined by Equations (2.30), (2.31), and (2.38). To close the system an EOS is used, discussed in Chapter 3.

4.3 Description and implementation of the new numerical scheme

4.3.1 Improved time integration RK

To implement the new numerical scheme into Mancha3D we improved the RK method explained in Section 3.4 by generalizing its accuracy order between one and fourth. In the single-fluid approximation, the system of equations written in conservative form can be schematically represented as

$$\frac{\partial \mathbf{U}}{\partial t} = \mathcal{R}(\mathbf{U}) = -\nabla \mathbf{F}(\mathbf{U}) + \mathbf{S}(\mathbf{U}) + \mathbf{G}(\mathbf{U}) \,, \tag{4.5}$$

where $\mathcal{R}(\mathbf{U})$ represents an operator formed by the sum of the spatial derivatives of fluxes $\mathbf{F}(\mathbf{U})$, the source terms, $\mathbf{S}(\mathbf{U})$, and the non-ideal terms (Ohmic, ambipolar, Hall, and Battery), $\mathbf{G}(\mathbf{U})$. The vector $\mathbf{U} = \mathbf{U}_0 + \mathbf{U}_1$, is the set of variables in the equations: $[\rho, \rho\mathbf{v}, \mathbf{B}, e](\mathbf{r}, t)$.

The next time step is calculated using an explicit RK scheme that can be written in a compact form as

$$\mathbf{U}^{(k)} = \mathbf{U}^{(n)} + \alpha_k \Delta t \mathcal{R}\left(\mathbf{U}^{(k-1)}\right) \,, \quad k = 1, \ldots, m \,, \tag{4.6a}$$

$$\mathbf{U}^{(n+1)} = \mathbf{U}^{(m)} \,, \tag{4.6b}$$

where $\mathbf{U}^{(n+1)}$ corresponds to the solution at $t_{n+1} = t_n + \Delta t$, with Δt given by the CFL condition, Eq (3.35). The order of the RK scheme is given by the chosen $m \leq 4$, and the coefficients α_k can be found in van Leer et al. (1989, Table 6) or easily computed using the Expression (4.7).

$$\alpha_k = \frac{1}{m + 1 - k} \,. \tag{4.7}$$

Mancha3D uses a fourth order RK scheme to solve the non-ideal single-fluid MHD equations, which using this notation corresponds to $m = 4$ in Eqs. (4.6). As in Section 3.4, the RK scheme only integrates in time the perturbed quantities $\mathbf{U}_1 = [\rho_1, \rho\mathbf{v}, \mathbf{B}_1, e_1](\mathbf{r}, t)$.

4.3.2 New MHDSTS scheme

As mentioned in Sect. 4.1, the non-ideal MHD terms are numerically problematic. In the solar atmosphere the value of the ambipolar diffusion coefficient (η_A) strongly increases with height and becomes larger than the classical Ohmic diffusion (η) by several orders of magnitude (Khomenko et al. 2014). When the ambipolar term dominates the equations, the system turns from hyperbolic to parabolic, and very small integration time steps are required in order to fulfill the CFL condition. To avoid such small time steps, the proposed MHDSTS[2] scheme uses the technique known as super time-stepping (STS). This numerical technique was proposed by Gentzsch (1980) to speed up explicit time-stepping schemes for parabolic problems. Later on, Alexiades (1995) and Alexiades et al. (1996) presented a variant of this technique, which is used by O'Sullivan & Downes (2006, 2007) to overcome the limitations caused by a large ambipolar term. As mentioned earlier, this numerical technique allows us to speed up, in a easy and efficient way, explicit time-stepping schemes for parabolic problems.

Besides, the Hall coefficient, η_H dominates over the other two coefficients (η and η_A) over most of the photosphere and then, the Hall effect can dominate the system (Khomenko et al. 2014). In this case, the system becomes skew-dominant, and the integration can not be done using the STS approach because it is unstable. In this situation, the system's eigenvalues become complex and to fulfill the CFL condition we would require that our time-step gets close to zero to maintain stability (O'Sullivan

[2] MHDSTS is the abbreviation for Mhd, HDS and sTS

& Downes 2006, 2007; Gurski & O'Sullivan 2011). Thus, the proposed MHDSTS scheme uses yet another scheme, Hall diffusion scheme (HDS), which was proposed by O'Sullivan & Downes (2006) to overcome this problem.

The STS technique has been used in different fields successfully, for example: Choi et al. (2009) described the implementation of the ambipolar term in a multi-dimensional MHD code based in a total variation diminishing (TVD) scheme showing its use to follow complex MHD flows such as molecular cloud cores or protostellar discs; Grewenig et al. (2010) introduced STS into a new class of numerical schemes called fast explicit diffusion (FED) schemes to speed up the application of anisotropic diffusion filters for image enhancement or image compression tasks; Tsukamoto et al. (2013) presented an explicit scheme for Ohmic dissipation with smoothed particle magnetohydrodynamics (SPMHD) and used the STS technique to solve the Ohmic part of the induction equation; Tomida et al. (2013) also adopted the technique to solve the Ohmic part of the induction equation in problems of protostellar collapse; Wurster et al. (2014) provided an implementation of the STS technique into the PHANTOM-SPMHD code (Price & Federrath 2010a,b; Lodato & Price 2010; Price et al. 2018) for solving the ambipolar part of the induction equation. At this point we also mention that there is another family of STS scheme based on the Legendre polynomials and its properties which have been applied in problems involving thermal conduction in astrophysical plasmas as prominences or coronal rain successfully (Meyer et al. 2012, 2014; Xia & Keppens 2016; Xia et al. 2017) or by Rempel (2017) to extend the MURaM code into the corona by implementing a hyperbolic heat conduction.

Equation (4.5) can be split into different terms (ideal MHD, Ohmic diffusion, ambipolar diffusion, etc.), and these can be grouped together in a number of operators. There are a few options to group those terms into operators, but for our new MHDSTS scheme we have grouped them into three operators (MHD, STS, and HDS) as described in the following sections. The splitting technique we have chosen to solve the system is the Strang splitting. This splitting is written in a way that keeps a second order accuracy along the simulation by permuting the order in which we apply the operators (Strang 1968; LeVeque 2002).

MHD operator

This operator is used to integrate the ideal MHD equations together with the battery term. We decided to include the non-ideal contribution of the Battery term into this solver because it does not limit the time step in solar-like problems (Khomenko et al. 2014). This operator can be defined as

$$\frac{\partial \mathbf{U}}{\partial t} = \mathcal{M}(\mathbf{U}) = \mathcal{L}^{\mathrm{iMHD}}(\mathbf{U}) + \mathcal{L}^{\mathrm{Batt}}(\mathbf{U}) \,, \tag{4.8}$$

where the vector $\mathbf{u}$ is, as before, the set of conserved variables, $\mathcal{L}^{\mathrm{iMHD}}(\mathbf{U}) = -\nabla\mathbf{F}(\mathbf{U}) + \mathbf{S}(\mathbf{U})$ is (as per Equation (4.5)) the standard operator for ideal MHD, and $\mathcal{L}^{\mathrm{Batt}}(\mathbf{U})$ is the operator for the battery term.

The temporal integration of this operator follows the same equations as Eqs. (4.6), but in this case the operator being $\mathcal{M}(\mathbf{U})$ instead of $\mathcal{R}(\mathbf{U})$ and the time-step being Δt_{MHD}, calculated as

$$\Delta t_{\mathrm{MHD}} = dt_{\mathrm{iMHD}} \,, \tag{4.9}$$

where dt_{iMHD} is obtained from the CFL condition applied to the operator $\mathcal{L}^{\mathrm{iMHD}}(\mathbf{U})$, see upper panel in Fig. 4.1. The Battery term time step, Eq. (3.34), does not play a role in this operator due to its source term behavior. It is important to point out that if there are no non-ideal terms this operator becomes a RK operator because there is no need to apply the Strang splitting. In this case, selecting

$m = 4$, we recover the RK scheme. This standard part of the MANCHA3D code was thoroughly verified via either specific numerical tests, applied in 1D, 2D, and 3D (Felipe et al. 2010), or through the scientific numerical simulations by the code published in the literature in the last ten years. The MHD scheme only integrates in time the perturbed quantities $\mathbf{U}_1 = [\rho_1, \rho\mathbf{v}, \mathbf{B}_1, e_1](\mathbf{r}, t)$.

STS operator

This operator is used to treat only the contribution of the Ohmic and ambipolar terms and it can be written as

$$\frac{\partial \mathbf{W}}{\partial t} = \mathcal{S}(\mathbf{W}) = \mathcal{L}^{\rm Ohmic}(\mathbf{W}) + \mathcal{L}^{\rm Ambi}(\mathbf{W}) \,, \tag{4.10}$$

where the vector $\mathbf{W} = \mathbf{W}_0 + \mathbf{W}_1$ corresponds to the conserved variables $[\mathbf{B}, e](\mathbf{r}, t)$ or $[\mathbf{B}, e_{\rm int}](\mathbf{r}, t)$ in the case where we prefer to use the internal energy equation, $\mathcal{L}^{\rm Ohmic}(\mathbf{W})$ is the operator for Ohmic diffusion, and $\mathcal{L}^{\rm Ambi}(\mathbf{W})$ is the operator for ambipolar diffusion.

The main idea behind STS is to demand stability not at each time step, but at the end of a bigger step called *super-step* ($\Delta t_{\rm STS}$). The $\Delta t_{\rm STS}$, see upper panel in Fig. 4.1, is calculated as a sum of *sub-steps* τ_j. To maximize the size and stability of the super-step, the small sub-steps are obtained using the optimality properties of modified Chebyshev polynomials (Alexiades et al. 1996).

$$\tau_j = dt_{\rm dif} \left[(\nu - 1) \cos\left(\frac{2j-1}{N_{\rm STS}} \frac{\pi}{2} \right) + 1 + \nu \right]^{-1} \,, \tag{4.11}$$

in this expression, $dt_{\rm dif}$ is the minimum time step given by the Ohmic term, Eq. (3.32), and by the ambipolar term, Eq. (3.33). $N_{\rm STS}$ is the number of sub-steps, and ν is a damping parameter, associated to the Chebyshev polynomials, to reduce higher frequencies and obtain a strong stability condition for the numerical method. This parameter is within the interval $(0, \lambda_{\rm min}/\lambda_{\rm max}]$, where $\lambda_{\rm min}$ and $\lambda_{\rm max}$ are the smallest and the bigger eigenvalues of the matrix $\mathcal{S}(\mathbf{W})$ respectively (Alexiades et al. 1996; Gurski & O'Sullivan 2011). When ν takes values close to one, the system is highly damped, and the super-step becomes more accurate in the same way that any numerical explicit scheme has smaller errors resulting from small time steps. When ν takes values close to zero, the system becomes unstable.

Thus, the value of the parameters $(N_{\rm STS}, \nu)$ control the stability, accuracy and speed of the method and depend on the spectral properties of the matrix $\mathcal{S}(\mathbf{W})$. But, as pointed out by Alexiades et al. (1996), a precise knowledge of the eigenvalues is not needed to obtain a robust method, so the values can be arbitrarily chosen by the user considering certain limits (stability, speed, error, etc.).
The time update by the STS operator can be written as

$$\mathbf{W}(\mathbf{r}, t_{n+1}) = \mathbf{W}(\mathbf{r}, t_n) + \sum_{j=1}^{N_{\rm STS}} \tau_j \frac{\partial \mathbf{W}(\mathbf{r}, t)}{\partial t}\Big|_{t_n + \sum_{k=1}^{j-1} \tau_k} \,, \tag{4.12}$$

where $t_{n+1} = t_n + \Delta t_{\rm STS}$ and the super-step $\Delta t_{\rm STS}$ is given by

$$\Delta t_{\rm STS} = \sum_{j=1}^{N_{\rm STS}} \tau_j = dt_{\rm dif} F(N_{\rm STS}, \nu) \,, \tag{4.13}$$

with

$$F(N_{\rm STS}, \nu) = \frac{N_{\rm STS}}{2\nu^{1/2}} \frac{\left(1 + \nu^{1/2}\right)^{2N_{\rm STS}} - \left(1 - \nu^{1/2}\right)^{2N_{\rm STS}}}{\left(1 + \nu^{1/2}\right)^{2N_{\rm STS}} + \left(1 - \nu^{1/2}\right)^{2N_{\rm STS}}} \,. \tag{4.14}$$

In the limit when ν tends to zero, the super-step formed by N sub-steps covers an N times bigger interval compared to N explicit time steps, namely:

$$\lim_{\nu\to 0} F(N_{\rm STS},\nu) = N_{\rm STS}^2 \implies \lim_{\nu\to 0} \Delta t_{\rm STS} = N_{\rm STS}^2 dt_{\rm dif}\,. \tag{4.15}$$

The STS scheme is a first order scheme and it belongs to the family of Runge-Kutta-Chebyshev (RKC) methods with N steps. Therefore, if used as described above, the overall precision of the MHDSTS scheme would be of first order, even if the precision of the other operators was bigger. In order to increase its order of accuracy one could perform a Richardson extrapolation (Richardson 1911; Richardson & Gaunt 1927) as suggested by O'Sullivan & Downes (2006). However, this implies many executions of the STS operator: three executions to reach second order, seven executions to reach third order and fifteen executions to reach fourth order.
For that reason, instead of performing a Richardson extrapolation, we consider the STS scheme as an "Eulerian" first-order step of our multi-step RK scheme, so now we should reach fourth order just with four calls to the STS scheme. In other words, we use the STS scheme to obtain the solution at the stable points of the RK scheme and in this way, get a high order solution. We refer to this technique for increasing the order of a numerical scheme as *RK-wrapper*. Thus, the complete temporal scheme for the STS operator can be written similarly to Equations (4.6) but, in this case, using the operator $\mathcal{S}(\mathbf{W})$ and its corresponding time step $\Delta t_{\rm STS}$:

$$\mathbf{W}^{(k)} = \mathbf{W}^{(n)} + \alpha_k \Delta t_{\rm STS} \mathcal{S}\left(\mathbf{W}^{(k-1)}\right)\,, \quad k = 1,\ldots,m\,, \tag{4.16a}$$

$$\mathbf{W}^{(n+1)} = \mathbf{W}^{(m)}\,. \tag{4.16b}$$

Each step of this RK-wrapper has a size of $\alpha_k \Delta t_{\rm STS}$, with α_k given by Eq. (4.7). Each of these steps represents a whole STS super-step, where $dt_{\rm dif}$ is scaled with α_k and the corresponding τ_j values are calculated according to Equation (4.11). With these, the conserved variables of the vector $\mathbf{W}^{(k-1)}$ are calculated using the Expression (4.12). As for the MHD operator, the STS scheme implemented in Mancha3D only integrates in time the perturbed quantities $\mathbf{W}_1 = [\mathbf{B}_1, e_1](\mathbf{r},t)$ or $\mathbf{W}_1 = [\mathbf{B}, e_{\rm int,1}](\mathbf{r},t)$.

HDS operator

The HDS operator only solves the Hall term in the induction equation. It is designed by O'Sullivan & Downes (2006) to overcome the problems originated by a skew-symmetric Hall term dominated system, and it can be written in conservative form as

$$\frac{\partial \mathbf{B}}{\partial t} = \mathcal{H}(\mathbf{B}) = \mathcal{L}^{\rm Hall}(\mathbf{B})\,, \tag{4.17}$$

where $\mathbf{B}$ is the magnetic field $\mathbf{B}(\mathbf{r},t)$, and $\mathcal{L}^{\rm Hall}(\mathbf{B})$ is the operator for the Hall term. This operator works similarly to the MHD operator described above. However, unlike it, the update of the magnetic field components is done using all the information available at the moment. O'Sullivan & Downes (2006) applied the HDS scheme by using a first order RK scheme and then, increasing the accuracy order by the application of a Richardson extrapolation. Instead, we follow the same idea proposed in Section 4.3.2, treating the individual HDS operator as an "Eulerian" step to use the RK-wrapper to increase its accuracy order. By doing so, we keep the stability properties of this implicit-like scheme but reaching a higher accuracy order in time and with less computational effort. The proposed scheme

would be:

$$B_x^{(k)} = B_x^{(n)} + \alpha_k dt_{\rm Hall}\mathcal{H}\left(B_x^{(k-1)}, B_y^{(k-1)}, B_z^{(k-1)}\right) , \tag{4.18a}$$

$$B_y^{(k)} = B_y^{(n)} + \alpha_k dt_{\rm Hall}\mathcal{H}\left(B_x^{(k)}, B_y^{(k-1)}, B_z^{(k-1)}\right) , \tag{4.18b}$$

$$B_z^{(k)} = B_z^{(n)} + \alpha_k dt_{\rm Hall}\mathcal{H}\left(B_x^{(k)}, B_y^{(k)}, B_z^{(k-1)}\right) , \; k=1,\dots,m , \tag{4.18c}$$

$$\mathbf{B}^{(n+1)} = \mathbf{B}^{(m)} . \tag{4.18d}$$

In these equations $dt_{\rm Hall}$ is the time step imposed by the Hall term through the CFL condition given by O'Sullivan & Downes (2007), that is, $dt_{\rm Hall} = 2/\sqrt{27}\min(dx^2, dy^2, dz^2)/\eta_H$. The HDS operator advances in time $\Delta t_{\rm HDS} = N_{\rm HDS} dt_{\rm Hall}$, by repeating the execution of the Equations (4.18) $N_{\rm HDS}$ times, which is the number of sub-cycles needed to cover one super-step $\Delta t_{\rm STS}$ and/or one $\Delta t_{\rm MHD}$; this is further elaborated in the following section, and see upper panel in Fig. 4.1.

If the order in which the Equations (4.18a, 4.18b, and 4.18c) are solved is maintained for successive time steps, an artificial handedness is introduced into the scheme. This could be avoid by reversing the order between time step or, as it was pointed by O'Sullivan & Downes (2007), performing a random permutation of the order in which the magnetic field components (4.18a, 4.18b, and 4.18c) are solved over successive time steps. This is especially important under certain circumstances, as for example if a strong directional bias is introduced in the initial state or in 3D numerical experiments. Such permutation can result in a small loss of numerical stability. The HDS scheme implemented in MANCHA3D only integrates in time the perturbed quantitie $\mathbf{B}_1$.

4.3.3 All together: timing and accuracy order

This new scheme is only worthwhile with respect to the RK when the ambipolar or Hall terms introduce a heavy constraint in the time step as we commented in Sections 4.3.2 and 4.3.2. Then, one should select the time steps for the operators according to the following rule:

$$dt_{\rm dif} \leq \Delta t_{\rm STS}(N_{\rm STS}, \nu) = \Delta t_{\rm HDS}(N_{\rm HDS}) \leq \Delta t_{\rm MHD} . \tag{4.19}$$

When the requirements of $dt_{\rm dif} \leq \Delta t_{\rm MHD}$ is not fulfilled, the evolution of the system is dominated by hyperbolic ideal MHD terms, and there is no need to apply this new MHDSTS scheme, then we are out of the STS (and/or HDS) regime.

To choose the time step for each iteration, one first has to choose the pair $(N_{\rm STS}, \nu)$ to keep the accuracy and stability during the simulation and also to try to maximize the size of the super-step along the simulation.

One option for choosing those values can be obtained using Equation (4.15) and forcing the STS operator to jump in time as far as the MHD operator allows it, so in the limit when $\nu \to 0$, we can write that

$$\Delta t_{\rm STS} \approx dt_{\rm dif} N_{\rm STS}^2 = \Delta t_{\rm MHD} \implies N_{\rm STS} \approx \left\lfloor \sqrt{\frac{\Delta t_{\rm MHD}}{dt_{\rm dif}}} \right\rfloor , \tag{4.20}$$

getting in this way an optimum approximation for $N_{\rm STS}$ which should be very close to the number of sub-steps needed to cover the time step imposed by the ideal MHD CFL (private communication with Nóbrega-Siverio).

Selecting the parameter ν can be a bit tricky, and for that reason it is convenient to define the STS efficiency as:

$$E_{\rm STS} = \nu^{1/2}\frac{\Delta t_{\rm STS}}{dt_{\rm dif} N_{\rm STS}} = \nu^{1/2}\frac{F(N_{\rm STS}, \nu)}{N_{\rm STS}} . \tag{4.21}$$

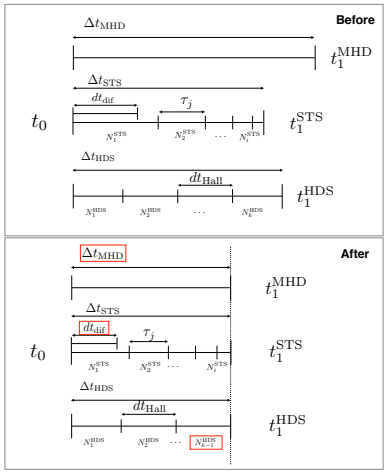

FIGURE 4.1— Example of time step adjusting. In the upper panel it is shown the situation before the adjust, all the super steps are different. In the lower panel the red square shows in each case the quantity that was changed. In this case, the code starts removing one sub-cycle of the HDS, then reduces $dt_{\rm dif}$ to mach the HDS super-step and finally reduces the MHD super-step to mach the other two.

This expression reaches an asymptotic value of 0.5 when $N_{\rm STS} \to \infty$ for a given ν, see dashed line in Fig. 4.2. It can be also approximated as $0.5\tanh\left(2\sqrt{\nu}N_{\rm STS}\right)$, see "+" markers in Fig. 4.2. Using this approximation for the efficiency we can obtain a value of ν to achieve a high efficiency and to maintain the stability and accuracy of the STS scheme.

To do so, we can impose a certain efficiency and calculate, for a chosen $N_{\rm STS}$ what value of ν it corresponds to. After several tests we have concluded that a good compromise between speed and stability is reached fixing the STS efficiency around a 76% of its maximum. This is equivalent to equating tanh to one, in which case we can write $\nu \approx 0.25/N_{\rm STS}^2$. Finally, replacing the value of $N_{\rm STS}$ obtained from Eq. (4.20) we get an estimation for ν. The choice of number of HDS sub-cycles $N_{\rm HDS}$ is done in execution time as $N_{\rm HDS} = \lfloor \Delta t_{\rm STS}/dt_{\rm Hall} \rfloor$.

The upper limit in time for the integration time step at any moment of simulation is given by the CFL condition applied to the ideal MHD operator $\Delta t_{\rm MHD}$. The goal then is to adjust $dt_{\rm iMHD}$, $dt_{\rm dif}$ and $N_{\rm HDS}$ to fulfill the identity $\Delta t_{\rm MHD} = \Delta t_{\rm STS} = \Delta t_{\rm HDS}$ (see Fig. 4.1 for an example).

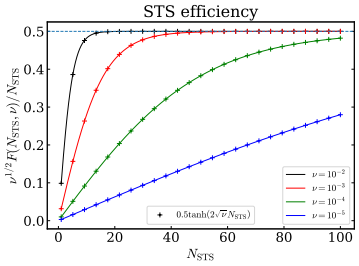

FIGURE 4.2— STS efficiency ($E_{\rm STS}$) defined by Equation (4.21) for different values of ν and its approximation ("+" markers). The dashed line indicates the asymptotic value of $E_{\rm STS}$ when $N_{\rm STS} \to \infty$.

Eventually, as we have mentioned, due to the Strang splitting, the overall order of the MHDSTS

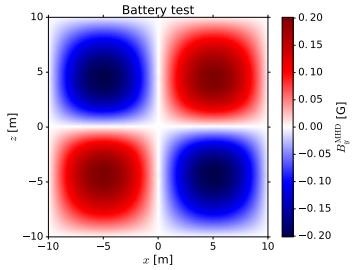

FIGURE 4.3— Biermann battery test. The image shows the y component of the magnetic field vector at one time step ($dt = 0.02$ s) after the beginning of the simulation.

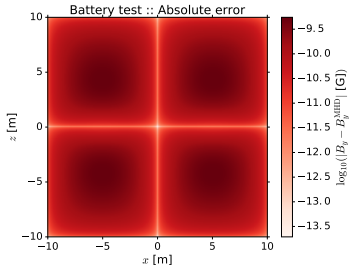

FIGURE 4.4— Logarithm of the absolute error in the B_y component of the magnetic field between the analytical solution and the numerical solution given by the MHD operator. The format of the figure is the same as Fig. 4.3. The error is minimum at locations with maximum electron density n_e.

scheme is limited to second order whenever each operator reaches second order accuracy or higher using the RK-wrapper method. This accuracy is expected to decrease due to the different combinations of values we can choose for the pair (N_{STS}, ν) and the physical characteristics of each simulation.

4.4 Numerical tests

As mentioned in Section 4.3.2, when all the non-ideal terms are switched off the MHDSTS scheme becomes a pure RK scheme because there is no need to apply the Strang splitting. This means that all the previous results obtained with MANCHA3D as well as the tests presented in Felipe et al. (2010) are also valid for this new version. Bearing this in mind, the sections below present specific numerical tests to only validate the newly introduced operators either individually, or working all together.

4.4.1 MHD operator test

For testing the MHD operator applied to the ideal part of the equations and the battery term, we performed the numerical experiment proposed by Tóth et al. (2012). In this test, a magnetic field is generated from scratch by means of the Biermann battery term in the induction equation. For this test, we have removed all the artificial diffusivities and considered only the contribution of the battery term. The initial conditions for this test consist in a homogeneous isothermal background without magnetic field and no velocity fields ($\mathbf{B} = \mathbf{v} = 0$). To initiate the evolution, a small perturbations in electron density (4.22) and electron pressure (4.23) are applied.

$$n_e = n_0 + n_1 \cos(k_x x) \,, \tag{4.22}$$

$$p_e = p_0 + p_1 \cos(k_z z) \,. \tag{4.23}$$

The analytical solution (4.24) is obtained by introducing the initial condition into the MHD equations and integrating it one single time step.

$$\frac{\partial B_y}{\partial t} = \frac{n_1 p_1 k_x k_z \sin(k_x x)\sin(k_z z)}{e[n_0 + n_1 \cos(k_x x)]^2} \,. \tag{4.24}$$

The numerical set-up consists in a 2.5D simulation box in the plane x–z. For this experiment we considered a double periodic domain in both x and z coordinates, covering a physical space of $\pm$ 10 meters, and using the constants, in S.I, $n_0 = 1/e$, $p_0 = 1$, $n_1 = 0.1/e$, $p_1 = 0.1$, $k_x = k_z = 2\pi/L$, and $L = 20$.

The numerical solution is obtained using our MHD operator, Fig. 4.3, and it is compared with the analytical solution by calculating the absolute error between them, see Fig. 4.4. We only compare the numerical solution with the analytical one after one single time step because if the system keeps evolving the analytical solution (4.24) is not valid anymore, in other words, the convective term will contribute to the solution. It can be seen that most of the numerical domain does not exceed $10^{-9.3}$ G of absolute error and this is concentrated in the regions where the initial electron density and electron pressure perturbations are maximum. We have not performed any further convergence tests of the standard MHD operator, because it has been fully tested by Felipe et al. (2010).

4.4.2 STS operator test

In order to test the implementation of the STS operator we use an experiment of Alfvén wave decay under the sole action of the ambipolar diffusion as it was proposed by Choi et al. (2009). This experiment is based on the analytical derivation of a dispersion relation characterizing the propagation of an Alfvén wave in a homogeneous partially ionized plasma permeated by a horizontal and homogeneous magnetic field done by Balsara (1996) when a strong coupling approximation is taken into account.

$$\omega^2 + ik^2\eta_A\omega - k^2c_A^2 = 0 \,, \tag{4.25}$$

In this relation, $c_A = B/\sqrt{\rho\mu_0}$ is the Alfvén speed, k is a real wavenumber and $\omega = \omega_R + i\omega_I$ is the complex angular frequency. It is known that the action of the ambipolar diffusion adds an imaginary term into the dispersion relation, which physically means that the Alfvén wave is unable to propagate when $k \geq 2c_A/\eta_A$ (Kulsrud & Pearce 1969). Under this strong coupling approximation and considering an ideal isothermal MHD system we can follow the evolution in time of a standing wave and compare the numerical results with the analytical solution of its first normal mode (Morse & Ingard 1968)

$$h(t) = h_0|\sin(\omega_R t)|\exp(\omega_I t) \,, \tag{4.26}$$

where h_0 is the initial wave amplitude.

For our experiments, we have considered an isothermal system in a 2.5D periodic domain in the plane $x - z$ of side L with a constant ambipolar coefficient and a constant magnetic field B_0 along the x coordinate, introducing a standing wave along the z coordinate with an initial velocity

$$\vec{\mathbf{v}} = \mathrm{v}_{\mathrm{amp}} c_A \sin(k_x x)\hat{\mathbf{k}} \,, \tag{4.27}$$

where $\mathrm{v}_{\mathrm{amp}}$ is a dimensionless initial peak amplitude. Taking $k = k_x$ in (4.25), it can be obtained that

$$\omega_R = \frac{k_x}{2}\sqrt{4c_A^2 - k_x^2\eta_A^2}, \quad \omega_I = -\frac{k_x^2\eta_A}{2} \,. \tag{4.28}$$

The analytical solution can be written as a superposition of two waves moving in opposite directions:

$$B_z(x,t) = A_0 \cos(k_x x)\sin(\omega_R t)\exp(\omega_I t) \,, \tag{4.29}$$

with

$$A_0 = \frac{\mathrm{v_{amp}} c_A k_x B_0}{\omega_R} \,, \tag{4.30}$$

and tracking the evolution of the root-mean-square (RMS) magnetic field $\left\langle B_z^2(t)\right\rangle^{1/2}$, the initial amplitude in (4.26) is $h_0 = A_0/\sqrt{2}$.

We set the parameters $\mathrm{v_{amp}} = 0.01$, $L = 1$ m, $B_0 = \mu_0^{1/2}$ T, $p = 1$ N/m, $\rho = 1$ kg/m^3, and $T = 1$ K for the initial condition and background. We considered four cases with different constant ambipolar coefficients $\eta_A = 0.01, 0.03, 0.1$, and 0.3 m^2 s^{-1}.

First, we used $N_{\mathrm{STS}} = 1$ and $\nu = 0$ for the STS scheme to test how the error changes by increasing the order when using the operator splitting. In Figure 4.5 we can see the results obtained in each case. In the upper panel of each subfigure we have the RMS evolution in time for the B_z component. In all cases the agreement between the analytical and numerical solutions is good, note we only plot the numerical solution when the order is set to two. In the middle panel the relative error in time for the numerical solution obtained with the RK scheme and the STS scheme and three different orders is plotted. If we focus in the solution at order two, we can see how the shape and values of each schemes are very similar in time. The same can be seen for the other orders. Besides, we see how the order three curve for the RK scheme overlaps with the order forth RK curve, and how the same thing happens with the orders three and forth of the STS curves. Because the relative error goes to infinity when $\left\langle B_z^2(t)\right\rangle^{1/2}$ drops to zero a good tool to see the time evolution of the error can be the cumulative root-mean-square error (CRMSE) in time define as

$$\mathrm{CRMSE}(t) = \sqrt{\frac{1}{n}\sum_{i=1}^{n}\left[f(t_i)_{\mathrm{Analytical}} - f(t_i)_{\mathrm{Numerical}}\right]^2} \,, \tag{4.31}$$

where n is the number of snapshots saved up to time t_n, t_i is the time of each output, and $f(t_i) = \left\langle B_z^2(x,t_i)\right\rangle^{1/2}$ (Wurster et al. 2014). This quantity represents the sample standard deviation of the differences between the RMS value from our numerical experiment and the analytical solution and, as Hyndman & Koehler (2006) point, it is a good measure of the accuracy between models at the same scale. This function is plotted in the lower panel of the subfigures of the Figure 4.5. When the rate at which the scheme adds error to the RMS is slower than the growth of the factor $\sqrt{n}$ for increasing time, the CRMSE will decrease slowly with time to an asymptotic value. This is clearly seen when the wave is damped quickly due to the high ambipolar diffusion. Furthermore, it is clearly seen how both schemes have a similar behaviour for all the ambipolar diffusivities tested.

Now we study how the pair (N_{STS}, ν) affects to the error, computational time and accuracy order of the STS scheme in comparison with the RK. To do this, we made a couple of simulations using different values of them. We took three values of ν $(0.1, 0.01$ and $0.001)$ and for each of them, N_{STS} was taken between one and six.

The results are shown in Figures 4.6 and 4.7 where in the upper panel we have plotted the CRMSE at a fixed time ($t = 5\tau$, with $\tau = L/c_A$) as function of (N_{STS}, ν). The time spent by each simulation to reach the same point in time (also at $t = 5\tau$) is plotted at the middle panel. At the lower panel we show the accuracy order measured at $t = 0.7\tau$. We chose this time to avoid values of the solutions close to zero (see vertical line marks in Fig. 4.5). All the tests where executed using a single node of the TeideHPC supercomputer (each TeideHPC node has 2 Intel Xeon E5-2670 processors, for a total of 16 cores per node).

In Figure 4.6a, upper panel, we observe how the accumulated error for STS at order two gives results very similar to the RK one. However, for higher orders, the error is slightly smaller than the one corresponding to the RK schemes (horizontal dashed-lines). We see how increasing N_{STS} (i.e.

increasing the number of times the STS operator will be called) introduces small extra errors. On the other hand we see how the CPU time increases linearly with $N_{\rm STS}$ due to these extra calls. Such behavior is expected because our system is outside of the STS regime due to the low ambipolar diffusion and in this case, performing STS involves unnecessary computational effort. In Fig. 4.6b the system gets into the STS regime only for $N_{\rm STS} = 2$, so for the rest of values we see the same behavior as before. In the other cases shown in Fig. 4.7, $\eta_A = 0.1$ or 0.3, we have that the accumulated error increases over the error obtained for the RK1. However, by using the STS technique we obtain a speed-up of between two and eight times depending on the RK order chosen to compare. For $N_{\rm STS} > 4$ the decreasing time tendency starts to invert, see Figure 4.7c. This happens because in this particular test, the STS jump reaches the size of the MHD jump and the code starts to spend time with extra iterations of the STS scheme as in the previous cases.

Finally, following LeVeque (2002), to measure the accuracy order for conservation laws, we computed the L_1-norm against the analytical solution given by Eq. (4.29) as

$$L_1(t_0) = \frac{1}{N_p}\sum_{i=1}^{N_p} |B_z(x_i,t_0)_{\rm Analytical} - B_z(x_i,t_0)_{\rm Numerical}| \,, \tag{4.32}$$

where the L_1-norm is calculated at $t_0 = 0.7\tau$ (see vertical dotted line in Fig. 4.5) and N_p is the number of points into the numerical domain. The results are in general consistent with the selected order of the schemes and limitation imposed by the Strang splitting. We notice nevertheless, that for this experiment, the rounding errors are affecting strongly the determination of the order because we quickly reach a precise solution, even when working with low orders. Thus, an increase of the order does not improve the solution, and therefore the value of the error calculated according to Eq. (4.32) is meaningless. This problem of the error evaluation can be seen clearly for the RK schemes with high ambipolar diffusion.

In the upper panel of Fig. 4.7c we observe how the CRMSE gets values close to one in some cases. These cases correspond to the lower value of ν, and illustrate how the solution is entering into a unstable region, that is, the sub-steps τ_j are giving unstable values and the solution would not converge at the super-step. Checking the lower panel of the same figure, one can see how these points also correspond to the accuracy order values with no meaning. We conclude that one needs to be very careful in choosing the value of this damping parameter to avoid numerical instabilities. As we have seen, good values for this parameter can be obtained using Eq. (4.21). Another thing we notice is that for $N_{\rm STS} = 1$ the behavior of the CRMSE, CPU time or order matches the RK scheme very well. This is because when $N_{\rm STS}$ is one, the damping parameter ν is zero and then, the STS acts as a MHD operator, (i.e. a RK scheme), and then only the Strang splitting is affecting the results. In this case in particular, the results can be seen in Fig. 4.5 and verify that, despite the wrong values obtained for the accuracy order, see for example the lower panel of Fig. 4.7c ($\eta_A = 0.1$ m^2 s^{-1}), the numerical solution matches very well the analytic one.

For the STS we observe how by increasing $N_{\rm STS}$ or decreasing ν the CRMSE is increasing and the computation time and the accuracy order are decreasing. On the other hand, we see that by increasing the ambipolar diffusion coefficient the accuracy order tends to decrease slightly and both the CRMSE and the computational time tend to increase.

Despite the fact that STS is limited to second order due to the Strang splitting, we observe that setting the order of each operator individually at three or more, makes the whole system more stable. This way, we could capture better stiff problems and/or force the values of $(N_{\rm STS}, \nu)$ to obtain a higher acceleration.

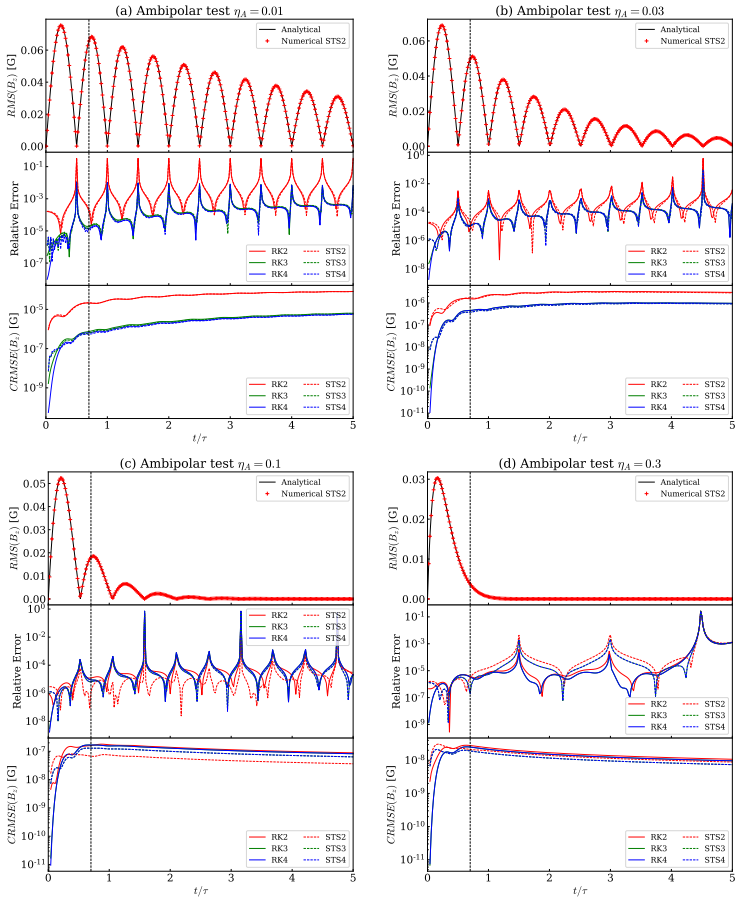

FIGURE 4.5— Upper panel: RMS value of the B_z component of the magnetic field produced by the Alfvén wave, as a function of time. The solid black line corresponds to the analytical solution and the crosses are the numerical solution obtained with the STS scheme at order two. It can be seen there is good agreement with the analytical solution for all the diffusivities tested. Middle panel: Relative error in time for the RMS value of B_z component. The red, green and blue lines are for the numerical solution given by the RK scheme working in the second, third and fourth order, respectively. The dashed lines corresponds to the solution obtained with the STS operator working also in second, third and fourth order. Green and blue lines are overlapped for most of the cases. Lower panel: CRMSE in time for both schemes defined by Eq. (4.31). As we expect, the behavior of both schemes is similar as it is shown by the CRMSE. The time axis is in the units of the crossing time $\tau = L/c_A$ and the dotted vertical lines mark the time where the L_1-norm is calculated, $t_0 = 0.7\tau$. All the experiments were done using $N_{\rm STS} = 1$ and $\nu = 0$.

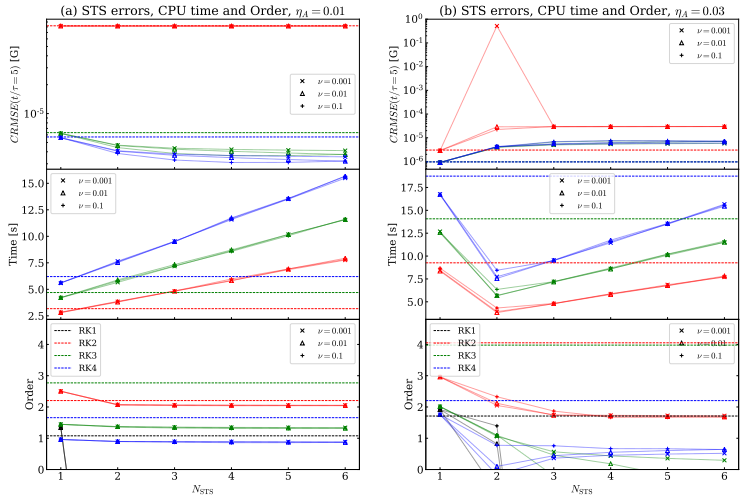

FIGURE 4.6— Upper panel: CRMSE values at $t = 5\tau$ s for different values of the pair (N_{STS}, ν). The horizontal dashed lines correspond to the RK scheme values. The symbols correspond to the STS scheme, each of them indicate a different value of ν. The black, red, green and blue colours indicate first, second, third and fourth order accuracy respectively. The dotted lines linking the symbols are drawn just to make the plot more readable. The middle panel shows the CPU time spend by the schemes to reach the same point in the simulations. The color and symbol code is the same as the upper panel. Lower panel: Order computed using the L_1-norm at $t_0 = 0.7\tau$, see the dotted vertical line in Fig.4.5; again, the color and symbol code is the same as the upper panel. In subfigure (a), we have a case with low ambipolar diffusion where the first order results unstable and the errors for the STS scheme are very close to the RK values. In this case, we have no acceleration because the system is out of the STS regime and the time increase linearly with N_{STS} as expected.

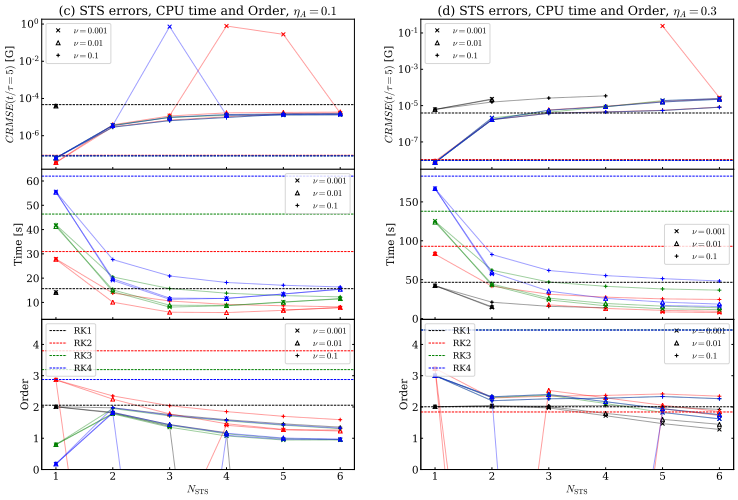

FIGURE 4.7— Same as Fig. 4.6, but showing a clear case inside the STS regime in subfigure (d). Here, the analytical solution is still well captured and the acceleration obtained is substantial. The errors, on the other hand, are limited, even though they are higher than in the RK1 case.

4.4.3 HDS operator test

In order to test the HDS operator we have considered an experiment with a plane-polarized Alfvén wave propagating into a partially ionized plasma under the presence of a guiding magnetic field as it is proposed by Cheung & Cameron (2012). For this experiment we have neglected all the induction terms except the Hall term.

The numerical set up for the test consists in a 2.5D periodical box with a constant hydrodynamic background and a pure Alfvén wave propagating along the x-axis. The transverse components are considered small compare with the guide field, B_x.

Under these conditions, the Hall coefficient, η_H can be considered constant and the analytical solution given by Equations (4.33a, 4.33b, and 4.33c), can be obtained after linearized the single-fluid equations. This solution describes the precession of the polarization plane of an Alfvén wave with a wavenumber k initially plane-polarized in the y-axis.

$$B_x(x,t) = B_0 \,, \tag{4.33a}$$
$$B_y(x,t) = b\cos(\sigma t)\cos(kx)\cos(\omega t) \,, \tag{4.33b}$$
$$B_z(x,t) = b\sin(\sigma t)\cos(kx)\cos(\omega t) \,, \tag{4.33c}$$

where ω is the angular frequency, B_0 is a constant uniform magnetic field, b is a small perturbation

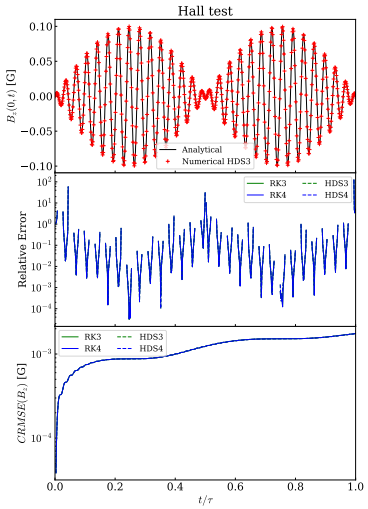

FIGURE 4.8— Hall test, showing in the upper panel the time evolution for the numerical and analytical solutions of the B_z components of the magnetic field fluctuations due to the precession of the plane-polarized Alfvén wave in a fixed spacial point ($x = 0$). The solid line represents the analytical solution and the red crosses are the numerical solution. In the middle panel it is plot the relative error of the numerical solution respect the analytical solution for both the RK and the HDS schemes, solid lines and dashed lines respectively. Lower panel shows the CRMSE in time for the B_z component. It can be seen how the two schemes have an almost identical behavior in time and with the order. This it is expected because the HDS operator works as a RK operator. Also this shows us how well performs the Strang splitting.

and σ is the precession rate of the polarization plane

$$\sigma = \frac{1}{2}\eta_H k^2 \,. \tag{4.34}$$

The relation between k and ω is obtained from the dispersion relation:

$$\left(\frac{\omega}{k}\right)^2 = c_A^2 + \frac{1}{4}\eta_H^2 \,. \tag{4.35}$$

For this experiment we select physical parameter to match those of the solar photosphere: $\eta_H = 10^6$ m^2 s^{-1}, $B_0 = 100$ G, $T = 6000$ K, $b = 0.1$ G, $p_{\rm gas} = 10^3$ N/m^2, $\rho = 10^{-4}$ kg/m^3, and $L = 100$ km so the domain covers one wavelength. For this set of parameters we have $k = 2\pi \times 10^{-5}$ m, $\sigma = 1.9 \times 10^{-3}$ Hz, $\omega = 5.6 \times 10^{-2}$ Hz, and the rotational period $\tau = 2\pi\sigma^{-1} = 3183$ s. For the initial conditions we set:

$$B_x(t=0) = B_0 \,, \tag{4.36a}$$
$$B_y(t=0) = b\cos(kx) \,, \tag{4.36b}$$
$$B_z(t=0) = 0 \,. \tag{4.36c}$$

In the upper panel of Figure (4.8) we can see the result of the simulations over the analytical solution given by Equations (4.33). In the middle panel we can see how the relative error is higher near the nodes and, in the lower panel, how the CRMSE increase in time as it is expected. We notice that simulations at first and second order are not plotted because they were not stable for the chosen CFL. However, at third and fourth order both schemes capture very well the analytical solution and they are very similar between them. Reducing the CFL slightly, the second order becomes stable.

4.4.4 MHDSTS scheme test

Finally, this section shows the results of testing simultaneously the MHD, HDS, and STS operators considering the effects of the Ohmic and ambipolar diffusion and the Hall term. For that, we used a shock-tube test with a magnetic precursor, or C-shocks (Draine 1980), under two different regimes depending of what term is dominating over the other non-ideal terms: a) Hall dominated and b) ambipolar dominated, see Falle (2003); O'Sullivan & Downes (2006, 2007).

To obtain the steady-state solution we consider our system isothermal with all the three diffusivity coefficients (η, η_A, and η_H) constants and no battery term. We also set all the time derivatives to zero, this is equivalent to transform the equations to a frame of reference where the shock is steady. With this, our MHD equations can be written as

$$\rho \mathrm{v}_z = C_0 \,, \tag{4.37a}$$

$$\rho \mathrm{v}_x \mathrm{v}_z - \frac{1}{\mu_0} B_x B_z = C_x \,, \tag{4.37b}$$

$$\rho \mathrm{v}_y \mathrm{v}_z - \frac{1}{\mu_0} B_y B_z = C_y \,, \tag{4.37c}$$

$$\rho \mathrm{v}_z^2 + c_s^2 \rho + \frac{1}{2\mu_0} B^2 - \frac{1}{\mu_0} B_z^2 = C_z \,, \tag{4.37d}$$

with the induction equation as

$$\left[\eta + \frac{\eta_A}{|B|^2}(B_x^2 + B_z^2)\right] \frac{\partial B_x}{\partial z} + \left[\frac{\eta_H}{|B|} B_z + \frac{\eta_A}{|B|^2} B_x B_y\right] \frac{\partial B_y}{\partial z} + \mathrm{v}_x B_z - \mathrm{v}_z B_x = C_1 \,, \tag{4.38a}$$

$$\left[\frac{\eta_A}{|B|^2} B_x B_y - \frac{\eta_H}{|B|} B_z\right] \frac{\partial B_x}{\partial z} + \left[\eta + \frac{\eta_A}{|B|^2}(B_y^2 + B_z^2)\right] \frac{\partial B_y}{\partial z} + \mathrm{v}_y B_z - \mathrm{v}_z B_x = C_2 \,, \tag{4.38b}$$

where C_0, C_x, C_y, and C_z are constants in time. C_1 and C_2 are constants of integration obtained from applying the pre-shock boundary condition.

The initial states for the pre-shock and post-shock plasma were obtained from the jump conditions of a front shock propagating into a magnetized fluid. The parameter for this initial state are given in Table 4.1.

Given the density and velocity at the post-shock side we can determine the magnetic field from the induction equation at each spatial position and then use the other four algebraical equations to obtain the rest of variables. To solve this ordinary differential system of equations with non-constant coefficients, we use a fourth order RK scheme implemented into a different code.

TABLE 4.1— Parameters for the MHDSTS test. The subscript 1 corresponds to the pre-shock side and the subscript 2 with the post-shock region. All parameters are in S.I.

Ini.	$\rho_1 = 1$	$\mathbf{v}_1 = (0, 0, -1.7)$	$\mathbf{B}_1 = (0.6, 0, 1)\mu_0^{1/2}$
Cond.	$\rho_2 = 1.8$	$\mathbf{v}_2 = (-0.6, 0, -1)$	$\mathbf{B}_2 = (1.7, 0, 1)\mu_0^{1/2}$
Case	$\eta = \mu_0$	$\eta_A = 25\mu_0/\lvert\mathbf{B}\rvert^2$	$\eta_H = 500\mu_0/\lvert\mathbf{B}\rvert$
(a)	$\nu = 0$	$N_{\mathrm{STS}} = 1$	$N_{\mathrm{HDS}} = 6$
Case	$\eta = \mu_0$	$\eta_A = 300\mu_0/\lvert\mathbf{B}\rvert^2$	$\eta_H = 750\mu_0/\lvert\mathbf{B}\rvert$
(b)	$\nu = 0.15$	$N_{\mathrm{STS}} = 2$	$N_{\mathrm{HDS}} = 8$

With these parameters, and avoiding the use of the artificial diffusion terms, the calculation is unstable for the RK scheme at all orders due to the high frequency oscillation (whistler waves) at the

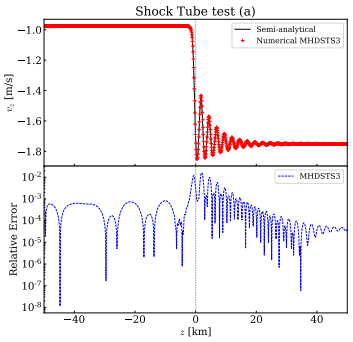

FIGURE 4.9— Hall dominated shock tube test. The upper panel shows the steady solution for the z-component of the velocity field. The left side corresponds to the post-shock side. The lower panel shows the relative error. The order obtained for this experiment is ~ 2.1.

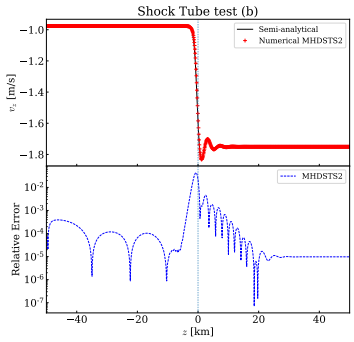

FIGURE 4.10— Shock tube test with high ambipolar diffusion and comparable with the Hall term. The upper panel shows the steady solution for the z-component of the velocity field. The left side corresponds to the post-shock side. The lower panel shows the relative error. The order obtain from this test is ~ 1.6 a slightly lower than the experiment (a) due to the STS contribution as mentioned in Subsection 4.4.2.

shock front introduced by the Hall term. The only way of solving this problem with the RK scheme without artificial diffusion is by forcing a reduced CFL condition and increasing the filtering cadence. Then, as a side effect we will spend more CPU time and tend to over-smooth the solution. The whistler waves can be seen clearly at the upper panel of Fig. 4.9, where we can also see how the analytical solution is very well captured by the MHDSTS scheme. In this case, if we choose order two without artificial diffusion, the experiment results unstable but choosing order three the experiment is stabilized due to the slightly higher numerical diffusivity introduced by the extra RK-step to reach order three. In the lower panel of the same figure we can see the relative error between both solutions. For this experiment, as we have obtained a semi-analytical solution, it is easy to compute the accuracy order by changing the mesh resolution. In this case the obtained order is ~ 2.1. In Fig. 4.10, we show a second experiment with a higher ambipolar diffusion to activate properly the STS operator but keeping also a high Hall term contribution. We see again the good agreement between both solutions and also how by increasing the ambipolar diffusion enough, the selected global order of the code needed to get the solution is lower. In this case, the calculated accuracy order is ~ 1.6, slightly smaller than the case (a) due to the action of the STS scheme.

4.5 Conclusions

In this Chapter we have seen that STS and HDS are numerical techniques easy to implement and also that they can work together using the Strang operator splitting formalism forming what we have called MHDSTS scheme. We also show how it is possible to increase the temporal order of accuracy using a RK formalism as a wrapper of each operator. However, MHDSTS is limited to second order by the Strang splitting, but setting the order of each operator individually at three or more makes the whole

system more stable.

So far, all the tests performed have shown a good agreement with the analytical solution. This makes us confident enough to use this new numerical scheme with MANCHA3D code in a production mode to investigate the effects of those diffusion terms with stiff problems.

We also check that the STS technique can speed up problematic simulations by overcoming the CFL condition imposed by the parabolic term corresponding to the ambipolar term. But as a note of alert, we have to be aware that we must choose carefully the pair ν and $N_{\rm STS}$ because, as Alexiades et al. (1996) mentions, and we show with a numerical test, the smaller ν and/or bigger $N_{\rm STS}$ means bigger the acceleration but also bigger errors and the increase of numerical instabilities, as well as a slight decrease of the accuracy order. These parameters should be maintained constant along the simulation to avoid numerical instabilities (private communication with Downes).

On the other hand, we also check that the HDS technique solves the problem with complex eigenvalues introduced by Hall term being more stable than our standard Runge-Kutta scheme and avoiding that our $dt_{\rm Hall}$ becomes very small, specially when the Hall term is dominating.

Working with the MHDSTS scheme, we have that the HDS time step is improved when the ambipolar or Ohmic diffusion are considered.

Finally, due to the whole scheme being explicit, even when HDS behaves as an implicit-like scheme, it is straightforward to use the other already implemented capabilities of the MANCHA3D code such as parallel scalability, the PML boundary condition, the AMR capability or the radiative transfer module.

5

Fast-to-Alfvén Mode Conversion Mediated by Hall Current. Application to the Solar Atmosphere.

If it disagrees with experiment, it's wrong. In that simple statement is the key to science. It doesn't make any difference how beautiful your guess is, it doesn't matter how smart you are who made the guess, or what his name is. If it disagrees with experiment, it's wrong. That's all there is to it.

- Richard P. Feynman lecture, 1960s

Coupling between fast magneto-acoustic and Alfvén waves can be observe in fully ionized plasmas mediated by stratification and 3D geometrical effects, as it was discussed in Chapter 2. However, Cally & Khomenko (2015) have shown that in a weakly ionized plasma, such as the solar photosphere and chromosphere, the Hall current introduces a new coupling mechanism. The content of this Chapter have been published and extends that result to the case of warm plasma using numerical experiments where mode transformation is studied using quasi-realistic stratification in thermodynamic parameters resembling the solar atmosphere (Gonzalez-Morales et al. 2019). This redresses the limitation of the cold plasma approximation assumed by Cally & Khomenko (2015), allowing to study the complete process of coupling between fast and slow magneto-acoustic modes and subsequent coupling of the fast mode to the Alfvén mode through the Hall current.

5.1 Introduction

In general, astrophysical plasmas are formed by electrons, ions, neutrals, and dust grains and all these particles interact with the magnetic field, either directly or via collisional coupling between charged particles and neutrals. When different inertia and collisional interactions produce a drift between electrons and ions, the ideal-MHD theory has to be modified to include the Hall effect. This introduces a Hall electric field proportional to the cross product of the current density and the magnetic field, which thereby contributes to a generalized Ohm's law, see Chapter 2. In order to treat the Hall effect, one has to apply so-called Hall-MHD theory.

Hall effect is originated by the different drift velocities of the charged particles in a magnetized plasma, it is then a non-ideal effect only related to the presence of ions and electrons in a classical

plasma. However the presence of other particles, like the neutrals in the partially ionized plasma, may increases its magnitude due to an incomplete ion-neutral collisional coupling. When the electron-cyclotron frequency ($\omega_{ce} = eB/m_e$) is high, the electrons can gyrate around the magnetic field lines freely between collisions. On the other hand, due to the larger ion mass, the ion-cyclotron frequency ($\omega_{ci} = eB/m_i$) results three order of magnitude smaller than ω_{ce} and then, for the same collisional frequency, the electrons remain attach to the magnetic field but the ions do not. Then the current density, $\mathbf{J}$, is no longer aligned to the electric field, $\mathbf{E}$. This incomplete coupling produce additional currents that may affect the evolution of magnetic structures. In partially ionized plasma, the Hall effect produces perturbations of the current in the direction perpendicular to plane formed by the magnetic field and the wave vector $\mathbf{k}$ (Cally & Khomenko 2015).

In the atmosphere of the Sun or solar-like stars, the plasma can be weakly ionized, reaching, for example, an ionization fraction as low as $\xi_i \sim 10^{-4}$ around the Sun's temperature minimum (Vernazza et al. 1981). Under these conditions, Cheung & Cameron (2012) investigated the effects of the Hall currents on the formation of structures in photospheric magneto-convection, showing how the Hall current can couple magneto-acoustic and Alfvén waves. Later on, Cally & Khomenko (2015) provided a corrected theory of Hall-current mediated coupling between the fast and Alfvén waves in cold (i.e., zero-β) plasmas. They demonstrated that coupling efficiency is proportional to the dimensionless Hall parameter $\epsilon_{\rm Hall} = \omega/\omega_{ci}\xi_i$, where ω is the wave frequency. Due to the smallness of the ionization fraction ξ_i, coupling can be produced even for relatively low-frequency waves. They show that the Hall effect produces an oscillation between the Alfvén and magneto-sonic states and the precession would be the beating between those modes. They found that this coupling occurs in places where the wave vector is nearly aligned with the magnetic field vector. It is also more efficient for relatively low magnetic field strengths, and for higher frequency waves. Cally & Khomenko (2015) speculated that such processes as reconnection, where high-frequency waves are produced, can be affected.

Unlike the geometrical mode conversion mentioned in Chapter 2 and studied by Cally & Goossens (2008), Khomenko & Cally (2012), or Felipe (2012) among others, Hall current makes possible the mode conversion to happen even if initially the wave vector and the magnetic field vector lie in the same two-dimensional plane. Moreover, once the transformation happens, the waves keep traveling long distance nearly aligned with the magnetic field so they could transfer energy to the surrounding plasma during the precession process.

The purpose of the current chapter is to advance the initial work done by Cally & Khomenko (2015), relaxing the approximation of cold plasmas. That approximation excludes acoustic modes. Nevertheless, the current schematic picture of mode generation, propagation and transformation in a stratified solar atmosphere suggests that acoustic waves play an important role in the chain of wave energy transmission to the corona. Acoustic p-modes propagating below the surface (and being fast modes there since $c_s > v_A$) reach the equipartition layer where they are partially transformed into fast magnetic waves. These subsequently refract and reflect back to the solar surface. As mentioned in Chapter 2, Alfvén waves are produced through a secondary transformation while the fast waves refract. By considering cold plasma, the first process (fast acoustic to fast magnetic transformation) is not considered, and, therefore, the efficiency of the production of Alfvén waves through the Hall current mechanism cannot be evaluated correctly for the solar case.

Here we perform simulations of the complete process beginning with imposed acoustic wave generation below the surface, and all subsequent transformations, including the Hall effect, are addressed on the way to the corona. We take account of realistic plasma stratification for the Sun, and realistic values of the magnetic field. In Section 5.2 we show the set of equations corresponding to a single fluid description with a generalized Ohm's law including the Hall term. In Section 5.3 we present the numerical setup. In Section 5.4 we show the results of the numerical experiments, while in Section 5.5 a brief summary is presented.

5.2 Equations

In this Chapter we adopt the Hall-MHD formulation for a partially ionized solar plasma. We neglect all other non-ideal effects (such as ambipolar diffusion and the battery effect) and consider only the non-ideal Hall term under the single-fluid approach seen in Chapter 2 and in more detail in Khomenko et al. (2014) and Ballester et al. (2018). In this approximation, the equations to be solved are the continuity equation,

$$\frac{\partial \rho}{\partial t} + \nabla \cdot (\rho \mathbf{v}) = 0 \,, \tag{5.1}$$

the momentum conservation equation,

$$\frac{\partial (\rho \mathbf{v})}{\partial t} + \nabla \cdot \left[\rho \mathbf{v}\mathbf{v} + \left(p + \frac{\mathbf{B}^2}{2\mu_0} \right) \mathbf{I} - \frac{\mathbf{B}\mathbf{B}}{\mu_0} \right] = \rho \mathbf{g} \,, \tag{5.2}$$

the induction equation,

$$\frac{\partial \mathbf{B}}{\partial t} = \nabla \times \left[(\mathbf{v} \times \mathbf{B}) - \eta_H \frac{\mu_0}{|B|} (\mathbf{J} \times \mathbf{B}) \right] \,, \tag{5.3}$$

where we retained the convective and Hall terms on the right-hand side. Here η_H is the Hall coefficient and is written in units of a diffusivity coefficient ($l^2 t^{-1}$, i.e. $m^2 s^{-1}$ in SI),

$$\eta_H = \frac{|B|}{e n_e \mu_0} \,. \tag{5.4}$$

The total energy conservation equation,

$$\frac{\partial e_{\rm tot}}{\partial t} + \nabla \cdot \left[\frac{\rho \mathbf{v}^2}{2} \mathbf{v} + \frac{\gamma p}{\gamma - 1} \mathbf{v} + \frac{1}{\mu_0} \nabla \cdot [\mathbf{B} \times (\mathbf{v} \times \mathbf{B})] \right] = \rho \mathbf{v} \cdot \mathbf{g} \,, \tag{5.5}$$

is written in terms of the total energy density per volume unit $e_{\rm tot}$, which is the sum of the kinetic, internal and magnetic energies,

$$e_{\rm tot} = \frac{1}{2} \rho \mathbf{v}^2 + \frac{p}{\gamma - 1} + \frac{\mathbf{B}^2}{2\mu_0} \,. \tag{5.6}$$

The electric current density $\mathbf{J}$ is defined through

$$\mu_0 \mathbf{J} = \nabla \times \mathbf{B} \,, \tag{5.7}$$

and Gauss's law for magnetism is

$$\nabla \cdot \mathbf{B} = 0 \,. \tag{5.8}$$

To close the system, the equation of state for an ideal gas is used. The equations above assume charge neutrality ($n_e = n_i$) and negligible electron mass ($m_e \ll m_i$).

5.3 Numerical setup

The numerical experiments described in this work are produced by the MANCHA3D code using numerical treatment of the Hall term, described in Chapters 3 and 4 (Gonzalez-Morales et al. 2018).

The modeled solar stratification is build using a 2.5D approximation, that is, vectors are three dimensional objects but the derivatives apply only in two directions, one horizontal and one vertical, taking those to be x and z. The model is horizontally homogeneous.

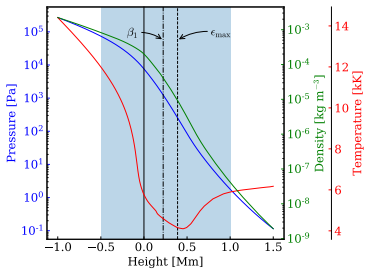

FIGURE 5.1— Pressure (blue), density (green), and temperature (red) as a function of vertical coordinate in the model atmosphere assumed in this study. The dot-dashed vertical line indicates the location of $\beta = 1$ layer. The dashed line corresponds to the location of the maximum of the Hall parameter ($\epsilon_{\max}$). The blue rectangle indicates the location of our numerical box.

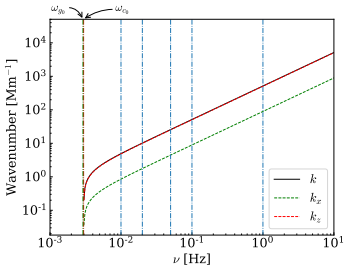

FIGURE 5.2— Modulus of the wave number k, as a function of the wave frequency at the bottom boundary of the numerical box, calculated according to Eq. (5.15). The blue vertical dot-dashed lines are the selected frequencies for the experiments. The red dot-dashed vertical line is acoustic cut-off frequency ω_{c_0} and the green one ω_{g_0}, both calculated at the bottom of the numerical domain.

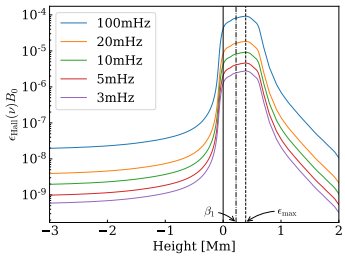

FIGURE 5.3— Hall parameter, in magnetic field units, as a function of height for different wave frequencies ν. The vertical line corresponds to the photospheric level, $z = 0$ km. The vertical dashed line shows where the Hall parameter has its maximum value, $z \approx 390$ km. The vertical dot-dashed line indicates the location of the equipartition layer ($\beta = 1$), $z \approx 228$ km.

The vertical stratification is build by merging the standard solar Model-S of Christensen-Dalsgaard et al. (1996) with the chromospheric model VAL-C of Vernazza et al. (1981) smoothly at height $z = 140$ km. Because the upper layers of the solar convection zone are super-adiabatic and unstable against convection, we modify the stratification in thermodynamic parameters to make it convectively stable and avoid the generation of modes that grow exponentially. To do this, we apply the procedure described by Schunker et al. (2011) solving the system iteratively and considering the hydrostatic equilibrium condition to the stratification with a constant value for the gravity $g_0 = 273.98$ m s^{-2} and a constant adiabatic coefficient $\gamma = 5/3$. The resulting stratification is illustrated in Figure 5.1. The numerical box is $L_z = 1.5$ Mm tall, extending from $z = -0.5$ Mm to $z = 1$ Mm.

Finally, a constant and uniform magnetic field $\mathbf{B}_0$ with adjustable inclination θ with respect to the vertical direction is included. The strength of the magnetic field is chosen based on the arguments explained below in this section.

To excite the waves in the simulation domain we impose an acoustic-gravity wave with a given

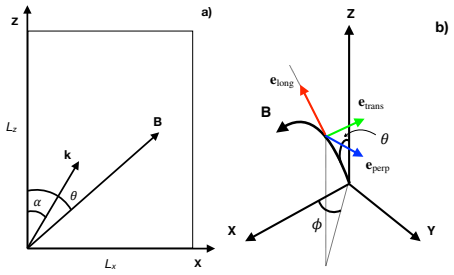

FIGURE 5.4— *Panel a)*: Schematic diagram illustrating the geometrical configuration of the numerical scenario. *Panel b)*: Schematic diagram to show the three characteristic directions.

frequency and horizontal wave number as a bottom boundary condition. This source introduces an acoustic-gravity wave of a given frequency ω and wavenumber k. The analytical solution for the perturbations in pressure, density, temperature, and velocity are calculated according to Mihalas & Mihalas (1984), providing a self-consistent solution. The magnetic field and temperature gradients are neglected in this formulation since the bottom boundary is located in the region where $v_A \ll c_s$ and they are unimportant at this depth. The analytical solutions applied are identical to those used by Khomenko & Cally (2012):

$$\delta V_z = V_0 \exp\left(\frac{z}{2H} + k_{zi} z\right) \sin\left(\omega t - k_{zr} z - k_x x\right) , \tag{5.9a}$$

$$\frac{\delta p}{p_0} = V_0 |P| \exp\left(\frac{z}{2H} + k_{zi} z\right) \sin\left(\omega t - k_{zr} z - k_x x + \phi_P\right) , \tag{5.9b}$$

$$\frac{\delta \rho}{\rho_0} = V_0 |R| \exp\left(\frac{z}{2H} + k_{zi} z\right) \sin\left(\omega t - k_{zr} z - k_x x + \phi_R\right) , \tag{5.9c}$$

$$\delta V_x = V_0 |U| \exp\left(\frac{z}{2H} + k_{zi} z\right) \sin\left(\omega t - k_{zr} z - k_x x + \phi_U\right) , \tag{5.9d}$$

where with the δ symbol we are indicating a perturbed quantity, p_0 and ρ_0 are the pressure and density at the bottom, V_0 is the initial amplitude for the imposed perturbation in velocity, $H = c_s^2/2g$ is the pressure scale height, k_x is the horizontal wavenumber, k_z is the vertical wavenumber made up of a real part k_{zr} and an imaginary part k_{zi}, and $\omega = 2\pi\nu$ is the angular frequency of the perturbation. $|P|$, $|R|$, and $|U|$ are the amplitudes given by

$$|P| = \frac{\gamma\omega}{\omega^2 - c_s^2 k_x^2} \sqrt{k_{zr}^2 + \left(k_{zi} + \frac{1}{2H}\frac{\gamma - 2}{\gamma}\right)^2} , \tag{5.10a}$$

$$|R| = \frac{\omega}{\omega^2 - c_s^2 k_x^2} \sqrt{k_{zr}^2 + \left(k_{zi} + \frac{\gamma - 1}{\gamma H}\frac{c_s^2 k_x^2}{\omega^2} - \frac{1}{2H}\right)^2} , \tag{5.10b}$$

$$|U| = \frac{c_s^2 k_x}{\gamma\omega} |P| , \tag{5.10c}$$

where γ is the adiabatic coefficient. The phases ϕ_P, ϕ_U, and ϕ_R are given by

$$\phi_P = \phi_U = \arctan\left(\frac{k_{zi}}{k_{zr}} + \frac{1}{2Hk_{zr}}\frac{\gamma - 2}{\gamma}\right) , \tag{5.11a}$$

$$\phi_R = \arctan\left(\frac{k_{zi}}{k_{zr}} + \frac{\gamma - 1}{\gamma H k_{zr}}\frac{c_S^2 k_x^2}{\omega^2} - \frac{1}{2Hk_{zr}}\right) . \tag{5.11b}$$

TABLE 5.1— Selected source frequency and relevant parameters for the numerical setups.

ν [Hz]	k_x [Mm^{-1}]	k_z [Mm^{-1}]	dx [km]	dz [km]	n_x	n_z
0.01	0.85	4.84	147.21	10	50	172
0.02	1.77	10.02	71.13	10	50	172
0.05	4.46	25.28	28.19	5	50	332
0.1	8.92	50.62	14.08	1	50	1612
1	89.29	506.40	1.41	0.05	50	32012

The vertical wave number is

$$k_z = k_{zr} + ik_{zi} = \sqrt{\frac{\omega^2 - \omega_c^2}{c_s^2} - k_x^2 \frac{\omega^2 - \omega_g^2}{\omega^2}}\,, \tag{5.12}$$

where the cut-off frequency is

$$\omega_c = \frac{\gamma g}{2c_s}\,, \tag{5.13}$$

and the Brunt-Väisälä frequency is

$$\omega_g = \frac{2\omega_c}{\gamma}\sqrt{\gamma - 1}\,. \tag{5.14}$$

The dispersion relation can be written in terms of the wavenumber modulus k and the propagation angle α as

$$k = \frac{\omega}{c_s}\sqrt{\frac{\omega_c^2 - \omega^2}{\omega_g^2 \sin^2\alpha - \omega^2}}\,. \tag{5.15}$$

To initiate the simulation it is necessary to specify the horizontal wave number, k_x, for the given frequency. Because we are interested in keeping the wave vector in the same direction for different source frequencies we calculate the components (k_x, k_z) for a given angle α by writing the dispersion relation in terms of the wave vector modulus as in Eq. (5.15). Figure 5.2 shows the behavior of k according this equation and the wave number vector components k_x, k_z as a function of the source frequency for a fixed angle $\alpha = 10°$.

For the top boundary we use a sponge-PML layer, defined in Chapter 3 (Section 3.10.1). The horizontal boundaries are set to periodic. The horizontal size of the domain, L_x, is determined by the value of k_x. Table 5.1 provides the details of the simulation runs. Our goal is to study how the efficiency of the transformation depends on the wave frequency. Therefore, the wave frequency is chosen to be a free parameter varying from simulation to simulation. We used frequencies from 0.01 to 1 Hz.

In order to select the background magnetic field strength B_0 for our experiments we consider the behavior of the Hall parameter $\epsilon_{\rm Hall}$, defined according to:

$$\epsilon_{\rm Hall}(\nu, B) = \frac{\omega}{\omega_{ci}\xi_i} = \frac{2\pi\rho_0}{q_e n_e}\frac{\nu}{B_0}\,, \tag{5.16}$$

where ρ_0 is the background density, q_e the electron charge, n_e the electron number density, ν is the wave source frequency, and B_0 is the background magnetic field. Figure 5.3 shows the Hall parameter, written in units of the background magnetic field, calculated for our stratification of thermodynamic parameters, as a function of height, for several wave frequencies. Independently of the frequency and

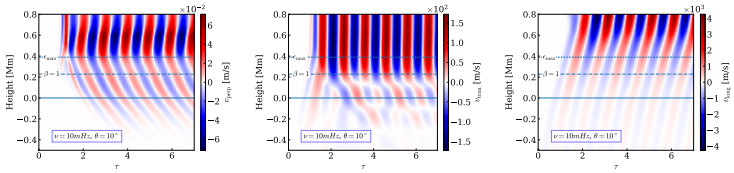

FIGURE 5.5— Time-height diagrams showing the velocity projections according to Eqs. 5.17 in the simulation with Hall term switched on. The background magnetic field was inclined by $\theta = 10°$, and a frequency was of $\nu = 10$ mHz. From left to right, velocity projections into $\mathbf{e}_{\rm perp}$ (Alfvén wave), $\mathbf{e}_{\rm tran}$ (fast wave), and $\mathbf{e}_{\rm long}$ (slow wave) directions. The units of the velocity color scale are m/s. The horizontal axis is dimensionless ($\tau = \nu t$). Horizontal lines indicate the photospheric level ($z = 0$), the equipartition layer ($\beta = 1$), and the maximum for the Hall parameter ($\epsilon_{\rm max}$). Notice that the v_y component is non-zero indicating the presence of the Alfvén wave, generated after the mode transformation.

the value of B_0, $\epsilon_{\rm Hall}$ has a maximum around $z \approx 390$ km. Therefore, we choose B_0 to place the equipartition layer below the height where $\epsilon_{\rm Hall}$ is maximum. This is because we wish to study the process of conversion between fast magnetic and Alfvén waves, and the fast magnetic waves are to be produced first through the primarily geometrical transformation at the region where $c_s = v_A$. To affect this compromise, we choose a magnetic field $B_0 = 500$ G, which locates the equipartition layer at $z \approx 228$ km, just below the maximum of the Hall parameter and inside the region where mode transformation can take place.

5.4 Alfvén wave production in the warm plasma

First we confirm that Hall-current mediated transformation is indeed taking place in our model. For that we separate the contribution of the three wave modes. This can be done relatively easily in our numerical experiment, given the 2.5D setup and the knowledge of the direction of the wave vector and the magnetic field vector direction. We calculated the projection of the velocity vector following Cally & Goossens (2008). This decomposition has been successfully used previously to identify the three wave modes propagating into a magnetized medium in similar models (e.g. Felipe et al. 2010; Khomenko & Cally 2011, 2012; Felipe 2012). Figure 5.4b shows a schematic diagram for the decomposition. The longitudinal component of the velocity given by $\mathbf{e}_{\rm long}$, the one parallel to the magnetic field, selects the slow magneto-acoustic wave in a low-β plasma. The other two components are perpendicular to the magnetic field. The component perpendicular to both $\mathbf{B}$ and ∇p (direction of the background pressure gradient, coinciding with the direction of gravitational stratification), given by $\mathbf{e}_{\rm perp}$, selects the Alfvén wave. Finally, the component perpendicular to the previous two, $\mathbf{e}_{\rm tran}$, selects the fast magneto-acoustic wave in the low-β plasma. Mathematically, this new basis can be written as:

$$\mathbf{e}_{\rm long} = (\cos\phi\sin\theta, \sin\phi\sin\theta, \cos\theta)\ , \tag{5.17a}$$
$$\mathbf{e}_{\rm perp} = (-\cos\phi\sin^2\theta\sin\phi, 1-\sin^2\phi\sin^2\theta, -\cos\theta\sin\theta\sin\phi)\ , \tag{5.17b}$$
$$\mathbf{e}_{\rm tran} = (-\cos\theta, 0, \cos\phi\sin\theta)\ , \tag{5.17c}$$

where θ is the magnetic field angle with the vertical z axis, and the ϕ the azimuth angle measured from the XZ-plane.

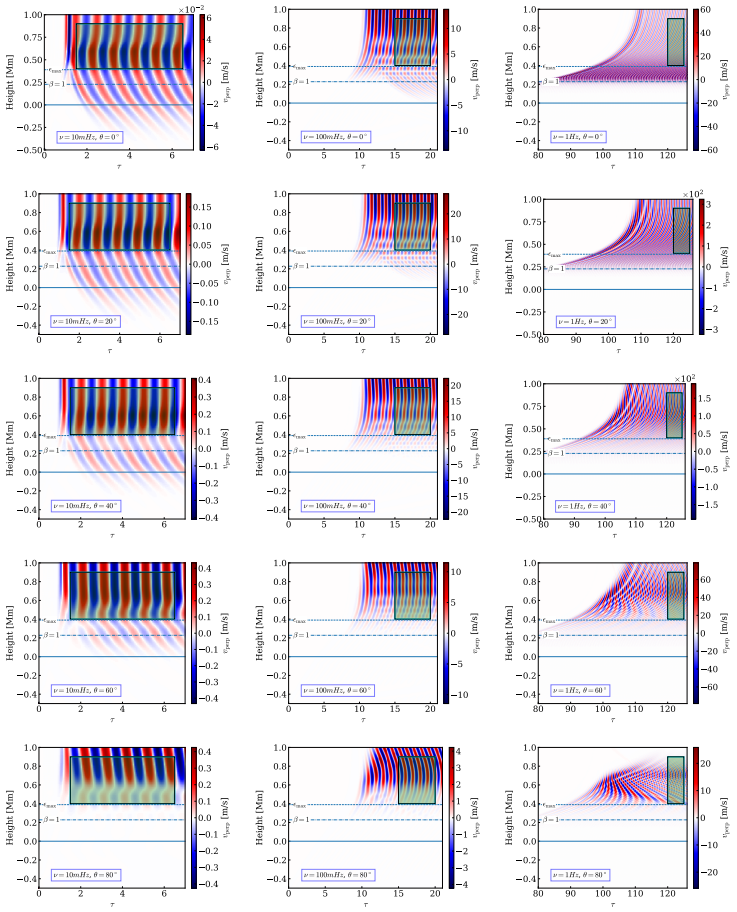

FIGURE 5.6— Time-height diagrams of the $v_{\rm perp} = v_y$ (Alfvén wave) velocity component in simulations with varying frequency (panels from left to right) and varying inclination angle of the magnetic field (panels from top to bottom). The Alfvén waves are generated through Hall mediated mode transformation. The values of the frequencies and inclination angles are indicated in each panel. The square box marks the region used to calculate the wave amplitudes in the stationary regime in the simulations summarized in Fig. 5.8.

In a 2.5D case, we set the azimuth $\phi = 0$, so the expressions for the components simplifies to:

$$\mathbf{e}_{\text{long}} = (\sin\theta, 0, \cos\theta)\,, \tag{5.18a}$$
$$\mathbf{e}_{\text{perp}} = (0, 1, 0)\,, \tag{5.18b}$$
$$\mathbf{e}_{\text{tran}} = (-\cos\theta, 0, \sin\theta)\,, \tag{5.18c}$$

this means that $v_{\text{perp}} = v_y$, so the v_y component of the velocity field is the one which selects Alfvén waves.

A note of caution must be taken regarding the above decomposition as is mentioned in the Section 2.5 of Chapter 2 since the component $\mathbf{e}_{\text{perp}}$ chooses the asymptotic polarization direction for the Alfvén mode in a plasma with any value of β but the two other directions, $\mathbf{e}_{\text{long}}$ and $\mathbf{e}_{\text{tran}}$ generally provide a mixture of the fast and slow magneto-acoustic modes. The particular contribution of each of the modes into $\mathbf{e}_{\text{long}}$ and $\mathbf{e}_{\text{tran}}$ depends on plasma β. In the limit of low-β, as mentioned above, most contribution to $\mathbf{e}_{\text{long}}$ comes from longitudinal slow magneto-acoustic mode, while the direction $\mathbf{e}_{\text{tran}}$ selects fast magneto-acoustic mode in this case.

As mentioned in Sec. 5.3, our source produces acoustic-gravity waves at the bottom of the numerical box. Since the plasma β is large there, the waves generated by the source are fast, essentially acoustic, waves. These waves propagate upwards and suffer a first mode transformation at the equipartition layer where the acoustic and Alfvén speeds coincide, splitting into the slow (essentially acoustic) wave component and fast (essentially magnetic) wave component in $v_A > c_s$. Due to the geometry of our numerical experiment setup, the wave vector $\mathbf{k}$ and the magnetic field vector lie in the same vertical plane (the x–z plane in Figure 5.4b). Therefore, in ideal MHD with the Hall term switched off, only fast and slow MHD waves can exist in our system, and no transformation to the Alfvén wave can take place. Mathematically, the velocity component v_y is exactly zero, since there is no coupling out of the x–z plane.

However, when the Hall term is switched on, a secondary mode transformation can take place. This transformation happens when the fast magnetic mode, generated by the primary mode transformation at $v_A = c_s$, enters into the region where the Hall parameter becomes important, see Figure 5.3. This way, Alfvén waves are produced from fast magnetic waves. This double mode transformation can be seen in Figure 5.5 [1].

In the first example, we see in the right panel of Figure 5.5 how the fast (acoustic) wave propagates with the acoustic speed upwards and how the fast and slow waves are generated after the primary mode transformation around 200 km height in the photosphere. The existence of both fast and slow components can be appreciated from different inclination of ridges in the middle and right panels. The fast (magnetic) mode ridges are much steeper above 200 km, indicating faster propagation speed. The fast magnetic mode can also be observed reflecting back to the sub-photosphere, which is seen as downward-inclined ridges and from the interference pattern below 200 km. The ridges become vertical above the reflection height, where the wave is evanescent. Such behavior is well known and has been observed before in many simulations (Khomenko & Collados 2009; Khomenko & Cally 2011; Felipe 2012; Khomenko & Cally 2012; Santamaria et al. 2015). The new feature one can observe in Figure 5.5 is the generation of the Alfvén mode, seen as a non-zero v_y component in the left panel. This component starts to appear at heights around 400 km in the photosphere, coinciding with heights where the Hall parameter is maximum; see the left panel Fig. 5.5. Nevertheless, the Hall-mediated transformation occurs throughout the height range. The amplitude of the Alfvén waves produced by this mechanism is highest immediately above the height where the Hall parameter is maximum.

Although the height of the numerical box is insufficient to completely encompass the region where the fast wave reflection takes place, part of the fast mode that is reflected downward again travels

[1] Fast-Alfvén coupling is also produced by 3D geometric effects, though these are absent in the 2.5D system.

through the region with high Hall parameter values. This way, downward propagating Alfvén waves are produced (ridges below $\epsilon_{\max}$ in the left panel of Fig. 5.5). A similar behavior was observed by Khomenko & Cally (2011, 2012) and Felipe (2012). However, in their simulations the Alfvén waves were produced through geometrical mode transformation, and not through Hall-mediated transformation.

One may notice that the amplitude of the Alfvén waves produced through the Hall-mediated transformation in Figure 5.5 is rather small, being about four orders of magnitude smaller than the amplitude of the slow acoustic mode at the equipartition layer. Nevertheless, the results of the theoretical investigation in cold plasma (Cally & Khomenko 2015) suggest that the amplitude of the Alfvén waves is a sensitive function of their frequency and of the inclination between the magnetic field and the wave vector. In order to study these dependencies in warm plasmas, we have repeated the simulations of Figure 5.5, but with different inclinations of magnetic field (from 0 to 90 degrees) and different wave frequencies (as indicated in Table 5.3).

Figure 5.6 shows the results of these experiments. It presents the time-height diagrams for the perpendicular component of the projected velocity ($v_{\rm perp} = v_y$) for three of the selected frequencies, $\nu = 0.01$, 0.1, and 1 Hz (columns) and five different inclination angles of the magnetic field, $\theta = 0$, 20, 40, 60, and 80 degrees (rows). All simulations share the same numerical setup including number of grid points per wavelength in the horizontal direction and the magnitude of the numerical diffusivity (necessary for the stability of the simulations). Nevertheless, it is unavoidable that higher frequency waves are affected more by numerical effects, and therefore their amplitude is inevitably lower than it should be. In order to account for these numerical effects and to standardize the experiments on the same scale, the velocities for a given frequency are scaled by setting the amplitude of the longitudinal component of the velocity $v_{\rm long}$ at the equipartition layer height in the simulation with $\theta = 10°$ to 500 m s^{-1}. The rest of amplitudes and perturbed quantities for this frequency are then scaled according to this factor.

We observe in Figure 5.6 that the amplitudes of both upward and downward propagating Alfvén waves depend on the inclination and frequency. In particular, the amplitude of the down-going wave becomes progressively smaller for larger magnetic field inclination angles. Similarly, simulations with higher frequencies show less down-going Alfvén wave, as measured by the amplitude. In all cases, the amplitudes of the down-going waves are smaller than of the up-going waves. The amplitudes of the up-going wave significantly increase with increasing frequency. The region where these amplitudes are maximal are located at or immediately above the height with maximum Hall parameter.

In order to confirm the visual impression about the presence of the Alfvén waves and their direction of propagation, and also in order to quantify our results in terms of energy supply to the upper layers, we computed the magnetic Poynting flux carried by waves:

$$\mathbf{F}_{\rm mag} = \langle \mathbf{B}_1 \times (\mathbf{v}_1 \times \mathbf{B}_0/\mu_0) \rangle \ , \tag{5.19}$$

and the acoustic flux

$$\mathbf{F}_{\rm acu} = \langle p_1 \mathbf{v}_1 \rangle \ , \tag{5.20}$$

where the subscript "1" denotes a small perturbation in velocity ($\mathbf{v}_1$), magnetic field ($\mathbf{B}_1$), and pressure (p_1). The angled brackets denote phase averages. Using Eqs. (5.17) together with Equation (5.19) we obtain the longitudinal component of the magnetic wave-energy flux. Considering only the perpendicular component of the velocity, we obtain a longitudinal magnetic flux associated exclusively with Alfvén waves:

$$\mathcal{F}_{\rm Alfvénic} = -B_1^{\rm perp} v_1^{\rm perp} B_0^{\rm long}/\mu_0 \ . \tag{5.21}$$

Figure 5.7 shows the Alfvénic flux in simulations with varying magnetic field inclination angle and frequency in the same format as Fig. 5.6. The amplitudes of the velocity and magnetic field oscillations were normalized for each frequency setting $v_{\rm long} = 500$ m s^{-1} at $\beta = 1$ height, in the simulation with

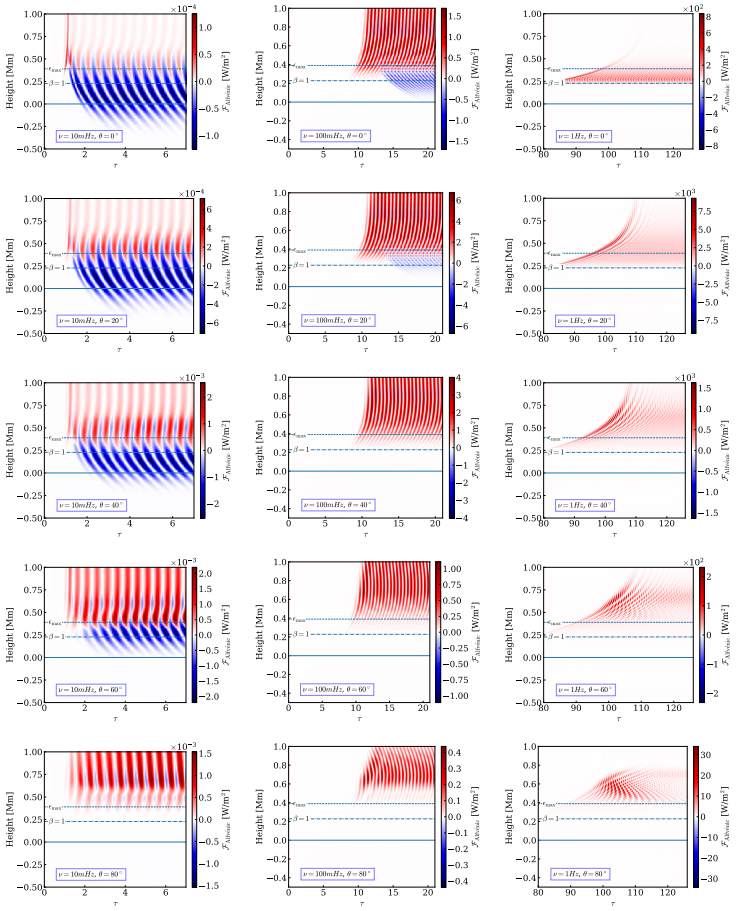

FIGURE 5.7— Time-height diagrams of $\mathcal{F}_{\text{Alfvénic}}$ in simulations with varying frequency (panels from left to right) and varying inclination angle of the magnetic field (panels from top to bottom). The values of the frequencies and inclination angles are indicated in each panel. Positive value of the magnetic flux (red colour) mean upward propagation.

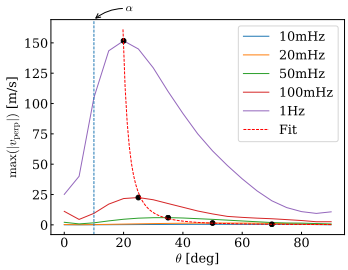

FIGURE 5.8— Velocity $v_{\text{perp}} = v_y$ of the Alfvén component as a function of magnetic field inclination angle. Different color lines present the results of the simulations with different frequencies, indicated in the figure. The maximum of each curve is marked with a black dot, the dotted vertical line corresponds to the wave vector angle (α). We observe how this maximum approaches to α for increasing frequencies.

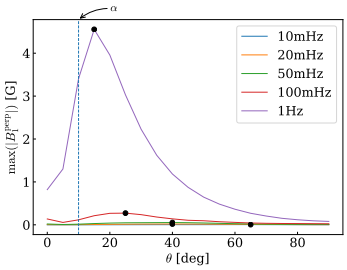

FIGURE 5.9— Perpendicular projection of the perturbed magnetic field as a function of the magnetic field inclination angle. Color lines correspond to results of the simulations with different frequencies. The maximum of each curve is marked with a black dot, the dotted vertical line corresponds to the wave vector angle (α). As in Fig. 5.8, we observe how this maximum approaches to α for increasing frequencies.

$\theta = 10$ degrees, as before. The results for the flux confirm that, indeed the ridges with the opposite inclination in Fig. 5.6 correspond to downward magnetic flux (blue color). They indeed vanish (in comparison to the upward fluxes) when the inclination angle and wave frequency are increased, though notice that the magnitude of the fluxes is orders of magnitude higher at 1 mHz than at the lower frequencies. Also, we observe how this flux increases up to a maximum value at a certain inclination angle, and then starts to decrease; see the column for $\nu = 100$ mHz for example. The magnetic flux for a given inclination angle increases with increasing frequency.

Finally, gathering together the results of all simulations, we have computed the amplitude of the perpendicular velocity once the system reaches a stationary regime. Figure 5.8 shows the results of this calculation as a function of inclination angle for all considered frequencies. This figure nicely summarizes the behavior mentioned above. Firstly, we see that the amplitude of Alfvén waves increases with increasing wave frequency. The maximum amplitude reached for waves of 1 Hz constitutes about 30% of the amplitude of the longitudinal wave component, which is significant. Next, for a given frequency, there is magnetic field inclination where the amplitude of the generated Alfvén waves reaches a maximum value. For low frequency waves this maximum falls at large inclination angles. But for progressively larger frequencies, the inclination with maximum amplitude approaches asymptotically the inclination of 10 degrees, i.e. $\theta = \alpha$, the inclination of the wave vector. In Figure 5.9 we can see similar behavior in the perpendicular projection of the perturbed magnetic field.

As mentioned previously, Hall-mediated transformation acts everywhere in the numerical domain and its efficiency increases with wave frequency. Because our numerical scheme contains numerical noise, it is important to carefully choose parameters such as the filtering cadence and the artificial diffusivity to keep this noise as low as possible to avoid its growth and the artificial Hall-mediated transformation that can be introduced into the simulations. Our chosen setup parameters made the simulations computationally very costly at progressively higher frequencies, so we had to truncate our numerical analysis at 1 Hz. Nevertheless, Figure 5.8 clearly suggests that for higher frequencies, the amplitudes would increase further. In order to quantify this increase we performed fitting to the

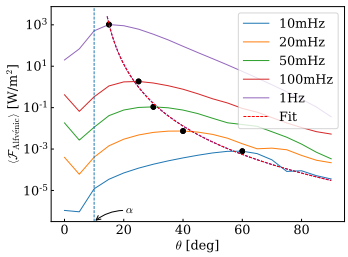

FIGURE 5.10— Temporal average of the Alfvénic flux at $z = 450$ km. Solid colored lines represents different frequencies, the dotted vertical line marks the wave vector angle α. The maximum of each curve is marked with a black dot. We observe a displacement toward the left of those maximum for increasing frequencies.

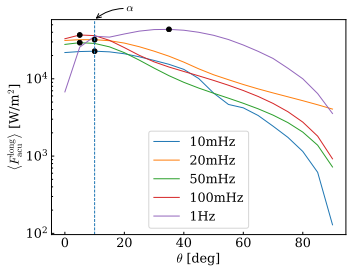

FIGURE 5.11— Temporal average of the longitudinal projection of the acoustic flux at the equipartition level. The dotted vertical line indicates the wave vector angle α. Solid curves correspond to different frequencies, and its maximum is marked with a black dot. We observe how the acoustic flux, for higher inclination angles of the magnetic field, increases with the wave frequency.

maximum values of velocity versus angle, using the following power law:

$$\max\left(|v_{\rm perp}|\right) = A\,(\theta - \theta_0)^m \ . \tag{5.22}$$

The best fit is for $A = 4475.88$ deg m s^{-1}, $m = -2.28$, $\theta_0 = 15.5°$. According to these parameters, an asymptotic angle with maximum velocity lies around 15.5 degrees. Nevertheless, this particular number should only be taken as an indication. Possibly, simulations with better sampling in θ would allow us to make a more precise fit. In addition, the amplitude of waves in numerical simulations is affected by numerical effects (such as numerical diffusivity). Although we kept the numerical parameters as similar as possible between all simulations, it is still possible that the numerical diffusivity affects the higher frequency waves (especially those at 1 Hz) more severely. Nevertheless, given all the uncertainties, we conclude that the amount of energy transferred from fast to Alfvén mode can be considerable. For a reference, Figure 5.9 provides the corresponding amplitudes of the magnetic field perturbation. For all the frequencies except 1 Hz, the amplitudes of B_1 do not reach above 1 G. This means that detecting such perturbations in observations would only be possible with the highest sensitivity polarimeters on the largest-aperture telescopes such as DKIST[2] or future EST[3]. In Figure 5.10 we collect the results for the average Alfvénic flux for all the inclinations and frequencies. This flux is calculated at $z = 450$ km, above the height with the maximum Hall parameter. This figure allows us to quantify the energy input by Alfvén waves into the higher layers. The Alfvénic flux reaches a maximum around 10^3 W m^{-2} at 15 degrees for the 1 Hz wave. The spatio-temporal root mean square (RMS) of the Alfvén flux, calculated for this frequency inside the green box marked in Fig. 5.8, is about 780 W m^{-2}. Making a similar fit to the Alfvénic flux as before, the asymptotic angle is $\theta_0 = 10.36°$, very close to the inclination angle of $\mathbf{k}$ with respect to the background magnetic field.

The values of the magnetic flux of Alfvén waves are to be compared to the available acoustic flux at some reference layer. We take for the reference the equipartition layer as the layer where the acoustic waves start to transform. Figure 5.11 shows the mean value of the longitudinal acoustic flux

[2]Daniel K. Inouye Solar Telescope, formerly the Advanced Technology Solar Telescope (ATST).
[3]European Solar Telescope

at the equipartition level. We observe that, in general, the acoustic flux pumped into the corona and then available to be transformed into Alfvénic flux slightly increases with frequency. The behavior of the curve for 1 Hz is slightly different from the others, probably due to numerical effects on this simulation. The values of the acoustic flux vary in the range of 10^2–10^4 W m^{-2} for all the frequencies. One can conclude that only for the highest frequency of 1 Hz does the Alfvén flux shown in Figure 5.10 contribute a significant fraction of the available acoustic flux.

On the other hand, in the full non-linear regime, which is not explored here, acoustic waves are much more subject to attenuation (by shocking for example) in the chromosphere than are Alfvén waves. Our results might therefore be expected to overestimate the acoustic wave flux reaching higher levels.

5.5 Discussion and Conclusions

In this Chapter, simulations are performed of Hall current mediated mode conversion to Alfvén waves for plasma parameters approximating the solar atmosphere. Numerical solution allow us to relax the cold plasma approximation assumed in the initial analytic study done by Cally & Khomenko (2015). We consider an acoustic-gravity wave with various frequencies propagating upwards from the lower boundary of our simulation domain located in the high plasma β region below the photosphere. Our simulations indeed show the presence of Alfvén waves when the Hall effect is acting. Therefore we confirm that this effect can be responsible for coupling fast magneto-acoustic and Alfvén waves even when there is no cross-field wave propagation (the usual coupling mechanism).

Cally & Khomenko (2015) concluded that the transformation is more efficient for vertical fields and wave propagation aligned with the field. The efficiency is also a sensitive function of the Hall parameter, and therefore it increases for increasing wave frequency ν and decreasing ionization fraction ξ_i. Our numerical experiments in warm plasma have partially confirmed this picture, but also shown a more nuanced behavior. We conclude that the efficiency of the transformation for low-frequency waves is maximal for strongly inclined fields (50–70 degrees). However, for waves at higher frequencies, the maximum becomes progressively aligned with the field. The asymptotic fit for the perpendicular velocity shows that the alignment between the directions of $\mathbf{k}$ and $\mathbf{B}$ is within 5.5 degrees for waves with frequencies above 1 Hz. A similar fit to the Alfvénic flux curves results in a difference between $\mathbf{k}$ and $\mathbf{B}$ of just 0.36 degrees.

A further conclusion concerns the absolute value of the effect. As discussed in the Chapter 2, in warm plasmas the transformation is a two-step process. First acoustic fast waves are partially transformed into magnetic fast waves at the $v_A = c_s$ equipartition layer, and then the latter are transformed into Alfvén waves progressively where Hall coupling operates. For that to happen there should be a specific relation between the location of the equipartition layer and the level with maximum Hall parameter $\epsilon_{\rm Hall}$. While the latter depends exclusively on the temperature structure of the atmosphere, the former is a function of the magnetic field. For the Hall-mediated transformation to be efficient one needs to satisfy simultaneously both conditions: (1) that the layer with $v_A = c_s$ is located below the layer with maximum $\epsilon_{\rm Hall}$, therefore B_0 has to be sufficiently large to have $v_A = c_s$ located deep enough; (2) that B is sufficiently small to maximize the value of $\epsilon_{\rm Hall}$. In our simulations we set $B_0 = 500$ G to satisfy both conditions. We reach the maximum amplitudes of Hall-excited Alfvén waves, about 30% of $v_{\rm long}$, for waves of the highest studied frequency, i.e., 1 Hz.

In practice,the process of Hall-mediated transformation acts in addition to the geometrical mode transformation to Alfvén waves suggested by Cally & Goossens (2008). It does not need any particular relation between the wave vector and the orientation of the magnetic field, and, our simulations suggest that the maximum transformation can occur for a broad range of magnetic field inclinations, depending on the wave frequency. Also, the considerations above suggest that the process would be efficient for intermediate field strengths of the order of hG, comparable to those existing in solar network and quiet

areas. Therefore, this process could provide a constant energy supply be means of Alfvén waves to the solar corona.

The 3D geometric fast/Alfvén coupling mechanism occurs near the fast wave reflection height, where the horizontal phase speed ω/k_h equals the Alfvén speed (in a low β plasma), and $k_h = (k_x^2 + k_y^2)^{1/2}$ is the horizontal wavenumber. At frequencies of a few mHz this may occur somewhere in the low-to-mid chromosphere, depending on magnetic field strength and k_h. However, at the high frequencies considered above (1 Hz etc), reflection may not occur till the transition region (TR) is reached. In that case, the two coupling regions (Hall and geometric) are spatially separated and would operate independently: Hall coupling would operate in the weakly ionized low chromosphere, and geometric coupling would set in once the TR is reached.

In our modeling, for waves of 1 Hz, the average Alfvénic energy flux we obtain at 450 km height (above the height of peak Hall coupling) is about 10^3 W m^{-2} with a RMS of 780 W m^{-2}. These numbers are bigger than what is required for heating the corona above quiet Sun regions, which is about 100–300 W m^{-2}, but are of the order of what is needed for heating the corona above active regions (Withbroe & Noyes 1977). The numbers we provide were obtained after normalizing the wave amplitude of $v_{\rm long}$ to be 500 m s^{-1} at $\beta = 1$ which, using Eq. (5.20), corresponds to an average acoustic wave energy flux of $\sim 3.8 \times 10^4$ W m^{-2} and a spatio-temporal RMS value of about 368 W m^{-2}. These values depend of the adopted base amplitude, which is probably overestimated at this frequency.

Theoretical estimates and measurements of the wave energy flux for such high frequency waves are uncertain (Fossum & Carlsson 2006). These authors provide measurements of the acoustic energy flux from TRACE[4] observations for frequencies up to a few hundred mHz, showing an exponential decrease of flux with frequency. The flux measured at largest frequencies by these authors makes 0.1–1 W m^{-2}. Simulations of acoustic wave generation by turbulence show a maximum wave energy at frequencies around 0.1 Hz with a strong decrease toward the higher frequencies (Musielak et al. 1994). The acoustic energy flux at 1 Hz reported by Musielak et al. (1994) makes 10^3 W m^{-2}. Assuming we can convert 1% of this acoustic flux into Alfvén waves and bring it to the solar corona, a good fraction of the energy needed to compensate its losses would be provided by Hall coupling. Although this flux is small compared to the peak acoustic flux at the same height, the Alfvén flux is far more able to penetrate to the corona, and so is more relevant to coronal heating.

Whilst fast modes refract and reflect in low-β regions and slow modes rapidly shock and damp, Alfvén waves can reach upper regions of the solar atmosphere due to their incompressible nature ($\nabla \cdot \mathbf{v} = 0$), making them an attractive mechanism to transport energy up to the corona. It is then a challenge to find mechanisms to dissipate Alfvén energy there.

Recently, simulations from Santamaria et al. (2017) have shown that slow magneto-acoustic shock waves coming from the chromosphere can trigger a jet-like structure of slow magneto-acoustic waves with frequencies up to 80 mHz around null points. These shock waves could be converted into fast modes around $\beta = 1$ regions with complex topology, and then they can be converted into Alfvén waves via the Hall term. Because the presence of null points is theoretically predicted almost everywhere, this double transformation could be an important source of production of Alfvén waves in complex magnetic topologies.

Possibly, Hall-mediated conversion can be important for other astrophysical scenarios, e.g. in star formation regions or reconnection events as well as in other cooler stars. Further investigations of 3D effects via the azimuth (ϕ) and stratification dependence, and taking into account other scenarios may also be interesting.

[4]Transition Region and Coronal Explorer

6

Effects of Hall Term in Solar Magneto-convection

There is a theory which states that if ever anyone discovers exactly what the Universe is for and why it is here, it will instantly disappear and be replaced by something even more bizarre and inexplicable. There is another theory which states that this has already happened.

- Douglas Adams, The Hitchhiker's Guide to the Galaxy, 1979.

As it was discussed in the previous chapters, partial ionization of solar plasma is an important phenomena that can potentially produce significant effects into the energy balance of the solar atmosphere. This chapter presents realistic three-dimensional simulations of solar dynamo where the magnetic field is seeded by the battery effect and then amplified to solar values by the local dynamo. ambipolar effect allows to dissipate incompressible perturbations associated to magnetic waves removing the magnetic Poynting flux and converting the magnetic energy into the thermal energy. Hall term introduces a new fast-to-Alfvén mode transformation mechanism and helps generating currents. The Alfvén wave generated in convection could travel to the upper layers and the currents could be dissipated by the ambipolar diffusion, closing the cycle. Then, the action of all three effects can be considered as an attractive mechanism of energy generation, transport, and chromospheric heating.

6.1 Introduction

To understand the connections established by the magnetic field between the weakly ionized photosphere and the partially ionized chromosphere, a non-ideal treatment of the plasma behavior due to the presence of neutrals is required as many works have demonstrated during the last years (De Pontieu & Haerendel 1998; Goodman 2000, 2011; Judge 2008; Krasnoselskikh et al. 2010; Martínez-Sykora et al. 2012; Khomenko & Collados 2012; Shelyag et al. 2016, among others).

The convective motions shake the photospheric magnetic field releasing energy which is in great part transported into the upper layers by waves. These waves are refracted, reflected and can be transformed into other type of waves, specially Alfvén waves, which are able to reach the upper layers of the atmosphere easily and could then produce perturbations of currents. The Ohmic and ambipolar diffusion effects can dissipate these currents, being the last one related to the presence of neutrals. In the chromosphere, collisions between ions and neutrals weaken, and their velocities can became different.

This difference in velocities generate a friction between these components, creating a situation where neutrals are pushing the ions across the magnetic field lines, resulting in a magnetic energy dissipation and a transformation of this energy into heat as Khomenko & Collados (2012) and Khomenko et al. (2014) had shown.

Realistic two-dimensional simulations show, for example, that the temperature inside cold chromospheric bubbles, generated by a nearly adiabatic expansion, is higher when the ambipolar diffusion is considered (Martínez-Sykora et al. 2012). It was also suggested that ambipolar diffusion could induce the generation of spicules by letting the field lines to reach higher layers, resulting in a misalignment between the chromospheric fibrils and the magnetic field (Martínez-Sykora et al. 2016, 2017). Recently, Khomenko et al. (2018), performed the first three-dimensional realistic magneto-convection simulations taking into account the ambipolar diffusion, and identified the observed chromospheric heating with the damping of incompressible magnetic waves and currents, pointing out that mechanisms associated to ambipolar diffusion can play an important role in the chromospheric heating.

Recent studies of the chromosphere are showing that the single-fluid formulation considering a strong coupling trough collisions may not be suitable in these region and a two-fluid or multi-fluid modeling should be applied. Recently, Popescu Braileanu et al. (2019a,b) have shown using a two-fluid modeling the importance of the ion-neutral decoupling in the omnipresent shocks. Unfortunately, realistic multi-fluid simulations remains as a challenge due to its complexity, see the work done by Maneva et al. (2017) or Kuźma et al. (2019) as an example.

Going back to the single-fluid approach, another important effect present in any plasma to take into account is the Hall effect. In partially ionized plasma the Hall effect is acting at scales factor $1/\xi_i$ larger, as was shown in Chapter 5. Thus it could be important in certain locations in the chromosphere and the transition region. It is known from the work done by Cally & Khomenko (2015) and the one presented in Chapter 5 that this term generates Alfvén waves by mean of coupling the fast magneto-acoustic and Alfvén modes in the low-β plasmas around the so-called Hall region, where $\beta \approx 1$ and $\epsilon_{\rm Hall}$ is large.

Only a few 2.5D realistic magneto-convection simulations have been done taking into consideration this non-ideal effect, see Martínez-Sykora et al. (2012) and Cheung & Cameron (2012). They shown the creation of a weak and out of plane current but as we know from Chapter 5, only a full three-dimension treatment is capable of fully describing the Hall effect.

In this Chapter we have performed 3D realistic simulations of the battery-excited small scale dynamo in the solar atmosphere including both, ambipolar diffusion and Hall effects, using the generalized Ohm's law in a single-fluid framework. In Section 6.2 we set non-ideal MHD equations taking into account the three non-ideal effects of study. In Section 6.3 we present the initial condition, the numerical setup and the boundary conditions used in the simulations. In Section 6.4 we present the results from the simulations and the discussion. Finally in Section 6.5 a brief summary an conclusion is presented.

6.2 Equations

For these numerical experiments we consider the non-ideal effects introduced by ambipolar, Hall, and Battery terms assuming a strong collisional coupling. Under this approximation it is feasible to use the equations of Section 2.2 and neglect the Ohmic term of both, the induction and energy equations.

$$\frac{\partial \mathbf{B}}{\partial t} = \nabla \times \left[(\mathbf{v} \times \mathbf{B}) - \eta_H \frac{\mu_0}{|B|} (\mathbf{J} \times \mathbf{B}) + \eta_A \frac{\mu_0}{|B|^2} [(\mathbf{J} \times \mathbf{B}) \times \mathbf{B}] + \eta_B \frac{\mu_0}{|B|} \nabla p_e \right], \tag{6.1}$$

$$\frac{\partial e}{\partial t} + \nabla \cdot \left[\frac{\rho \mathbf{v}^2}{2}\mathbf{v} + \frac{\gamma p}{\gamma - 1}\mathbf{v} + \frac{1}{\mu_0}\nabla \cdot [\mathbf{B} \times (\mathbf{v} \times \mathbf{B})] \right] = \rho \mathbf{v} \cdot \mathbf{g} + \\ + \nabla \cdot [\mathbf{B} \times (\eta_A \mathbf{J}_\perp)] + \nabla \cdot \left[\eta_B \frac{\nabla p_e \times \mathbf{B}}{|B|} \right] + Q_{\rm rad} \, . \tag{6.2}$$

This approximation is possible because for the quiet Sun, the Hall term becomes important at heights above 200 km and the ambipolar term at heights above 1 Mm, being both more important than the Ohmic term along those heights (Khomenko et al. 2014). To justify the removal of the Ohmic term, it is possible to compare the temporal scales of the non-ideal terms against the convective term. If the plasma velocity $\mathbf{v}$ is comparable to the Alfvén speed, then the temporal scales results in $\tau = \eta_{\{\rm Ohmic,Ambi,Hall\}}/v_A^2$. Using the expressions (2.30), (2.38), and (2.31) respectively the temporal scales result in

$$\tau_{\rm Ohmic} \sim \frac{\nu_{ei} + \nu_{en}}{\omega_{ce}^2} \, , \tag{6.3a}$$

$$\tau_{\rm Ambi} \sim \frac{\xi_n^2}{\xi_i \nu_{in} + \xi_e \nu_{en}} \, , \tag{6.3b}$$

$$\tau_{\rm Hall} \sim \frac{1}{\omega_{ce}} \, , \tag{6.3c}$$

with these expression the Ohmic term becomes important on scales given by the ratio of the electron collisional frequency and the square of the electron cyclotron frequency, ambipolar term becomes important on scales proportional to ion-neutral collisional time, and finally Hall term will be important on scales close to the ion cyclotron period. In Figure 6.1 those scales are shown for the quiet Sun using the VAL-C model and a magnetic field profile typical for a flux tube. Ohmic term is then important close to the photospheric level where the collisions are important, meanwhile the ambipolar term is important above the temperature minimum, while the Hall term is more important than the Ohmic term all over the photosphere.

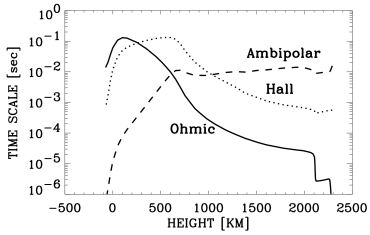

FIGURE 6.1— Temporal scales for the quiet Sun (VAL-C) where Ohmic, ambipolar, and Hall terms become important relative to the convection term in the generalized Ohm's equation. Extracted from Khomenko et al. (2014).

6.3 Numerical Setup

To initiate the magneto convection simulation Khomenko et al. (2018) started from a purly hydrodynamic setup and when it is stabilized, the magnetic field was introduced through the Battery term. The initial atmosphere was a plane-parallel stratification which combines the subphotospheric convective solar model of Spruit (1974) with the Harvard Smithsonian reference atmosphere (HSRA) model by Gingerich et al. (1971). The HSRA model combines EUV observations with a quiet lower chromosphere model based in observations of the Lyman continuum, infrared observations and the observed electron density during a solar eclipse. The model by Spruit (1974) is based on the mixing length formalism and has four free parameters to match the empirical model HSRA and a solar interior model to get a good mean temperature-pressure relation for the convection zone. The numerical box had $288 \times 288 \times 168$ points distributed forming a uniform grid. The horizontal sampling was 20 km and the vertical one was

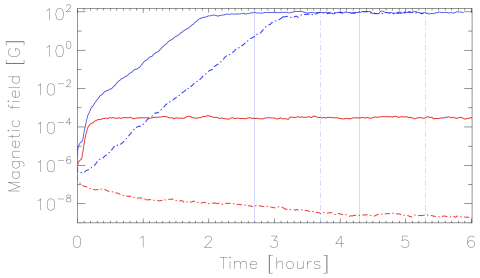

FIGURE 6.2— Mean value of the magnetic field module at the photospheric level ($\tau_{500} = 1$) as a function of time after turning on the battery term. Solid blue line: run with battery seed. Dashed blue line: run with random seed. Solid red line: run with battery term and numerical diffusion for magnetic field (constant and hyper-diffusion). Dashed red line: run with random seed and numerical diffusion for **B**. Extracted from Khomenko et al. (2017).

14 km, giving a box size of $5.8 \times 5.8 \times 2.35$ Mm^3. About 0.95 Mm in the vertical direction correspond to the upper layers of the convective zone bellow the photospheric level, and about 1.4 Mm extend from here to the lower chromosphere layers. The horizontal boundary condition were set periodic. The upper and bottom boundary conditions were set up following the Subsection 3.10.2. Upper boundary is closed to mass flows having zero gradient in density and internal energy; the temperature is computed using the tabulated EOS and because it has no further restriction imposed, the atmosphere is structured by shock viscous dissipation, magnetic field dissipation and radiative losses. Bottom boundary is closed to mass flows, keeping an approximately constant value for the mass inside the domain by controlling its global fluctuations and the total radiative output with a zero magnetic field inflow.

The initial snapshots used here come from the D and D-AD runs done by Khomenko et al. (2018), see Fig. 6.3. The beginning of their simulation is purely hydrodynamic and 2D. The simulation runs approximately for 20 min of solar time until the outgoing flux recovers its initial value due to the development of convective motions and then it keeps running another 3.4h to be sure the convection reaches a stationary regime. At this point the battery term is switch on, seeding fields of around 10^{-6} G as a consequence of the existing misalignment between the pressure and density gradients. This magnetic field is amplified by local dynamo effects as it was confirmed by Vögler et al. (2005) or Vögler & Schüssler (2007) among others. After approximately 2h of switching on the battery term the dynamo provides a mean magnetic field strength of $\sim 10^2$ G at photospheric level, see the solid blue line of Fig. 6.2. After 2.2h more into the saturated dynamo regime a snapshot is saved and two branches are created, the first one continues only with the battery term (D), the second one adds the ambipolar diffusion term (D-AD). From this moment, both branches run during another 150 min of solar time until D-AD reaches a new stationary regimen.

For our experiments the branches D and D-AD are used as initial condition restarting the simulations at $t_{\rm ini}$ and using the version of MANCHA3D code explained in Chapters 3 and 4. From experiment D a new branch labeled BATT it is obtained, and from experiment D-AD the branches labeled AMBI and AMBIHALL, where the last one has activated the Hall term, are obtained. All these experiments are kept running until they reach a new stationary regime with the non-ideal terms. The three branches reach the same solar time ($t_{\rm fin}$) giving about 4.13 h of data. Each of the branches is saved using a high cadence of 10 s to reach high frequencies with the Fourier analysis, see Fig. 6.3. As Khomenko et al. (2018) pointed out, the approximations underlying radiative transfer do not allow us to make conclusions about the absolute value of temperature in the chromosphere. Therefor, we

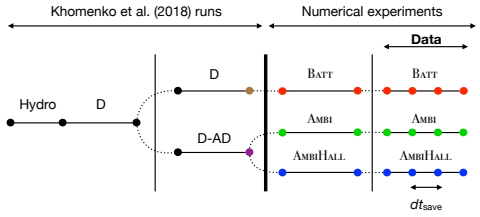

FIGURE 6.3— Schematic evolution of the numerical experiments and the origin of branches. The Batt simulation has its origin in the D run of Khomenko et al. (2018). The simulations Ambi and AmbiHall have their origin in the simulation D-AD of Khomenko et al. (2018). The analyzed data in this work correspond to the last 2h of each branch using a saving cadence of 10s.

perform a statistical comparison between different simulations, with or without specific effects.

6.4 Results and dicussion

Since the contribution introduced by each of the non-ideal terms modifies the convection a bit, the convective pattern and the magnetic field distribution of each simulation start to differ more and more in time and hence only a statistical analysis between the results would be appropiate.

We are interested in the properties of the waves generated in the models and in the effects introduced by the Hall term and the ambipolar term in comparison to the previous results obtained by Khomenko et al. (2018) considering only the ambipolar term. Therefore here we follow a similar procedure to analyze the data sets. Our higher cadence and longer length of the saved series not only allow us to compare our simulations with them, but also to reach a higher frequency range as well as to check the modifications introduced into the numerical code, see Chapter 3.

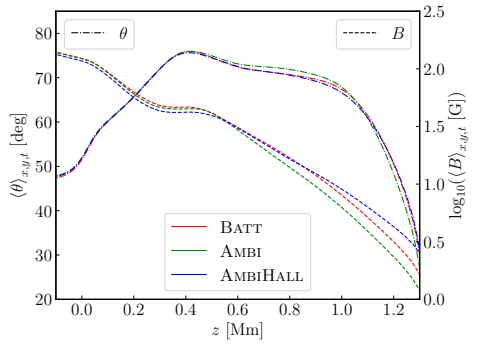

FIGURE 6.4— Horizontal–time averaged magnetic field inclination on the left axis, dot-dashed curves and horizontal–time averaged magnetic field strength on the right axis, dashed curves. Colors correspond to the three runs, red Batt, green Ambi, and blue AmbiHall respectively. The averaged inclination angles are very similar for the three simulations, however the averaged magnetic field strength at layers above 0.6 Mm differs between the runs, being higher when the Hall term is considered (blue dashed line).

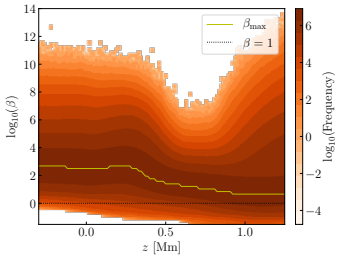

FIGURE 6.5— Two-dimensional histogram showing the frequency of occurrence of a given value of plasma β as a function of height for the AMBIHALL run. The solid curve marks the locus for the maximum value of the frequency. The horizontal dotted line corresponds to $\beta = 1$ layer.

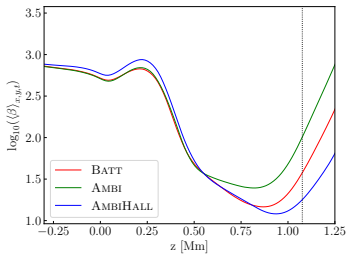

FIGURE 6.6— Average profiles for the plasma β of each run as function of height. The vertical dotted line corresponds to the height where the $\beta = 1$ layer has a maximum in frequency of occurrence for the AMBIHALL run.

6.4.1 Averaged parameters

Before starting with the wave analysis, we first characterize the average magnetic field configuration along the simulations by calculating different quantities. The first one is the distribution of the horizontal–time averaged magnetic field strength and inclination as a function of height for the three runs, both shown in Fig. 6.4. As expected, the curves are very similar in shape and magnitude to the ones shown in the Fig. 1 of Khomenko et al. (2018) (orange solid lines in their figure). The averaged magnetic field decreases with height from hG bellow the photosphere to a few tens of Gauss at the chromosphere. These curves have a secondary maximum around the temperature minimum height which are related to the high inclination of the magnetic field lines in that region ($\sim$ 75 degrees). Those field lines are connecting complex bipolar structures corresponding to the small-scale canopies or HIFs (B mark in Fig. 1.5). Next, we study the distribution of β plasma in our numerical box. Because of the large point to point variation, in the simulations, it is convenient to plot the two-dimensional histogram as shown in Figure 6.5. This histogram includes all the spatio-temporal points for the AMBIHALL run along the 2h of simulation under study, showing only the heights of interest for simplicity. From the averaged values of β shown in Figure 6.6, we see that the flow happens mainly under the high-β conditions. Around 1.1 Mm (vertical dotted line) the probability of having $\beta < 1$ in maximum, for all three runs, see in Figure 6.7. The activation of the Hall term not only induces fast-to-Alfvén mode transformation as we saw in Chapter 5 but also induces a higher number of spatial points belonging to the equipartition layer, where the mode transformation may occurs.
As in Chapter 5, here it is interesting to consider the Hall parameter ($\epsilon_{\rm Hall}$) for our stratification

$$\epsilon_{\rm Hall} = \frac{2\pi\rho}{q_e n_e}\frac{\nu}{|\mathbf{B}|}\,. \tag{6.4}$$

Figure 6.8 shows the Hall parameter computed point to point for the stratification, and averaged in the horizontal direction and time. As in Figure 5.3, the solid colored curves are calculated in magnetic field units for different constant wave frequencies ν, $\epsilon_{\rm Hall}(\nu)|\mathbf{B}|$. Those curves manifest similar shape and values near the geometrical photospheric level compared to the simpler stratification used in Chapter 5. Above the photospheric height, instead of decreasing with height, $\epsilon_{\rm Hall}$ remains almost constant showing a small depression around the height where there is a higher probability of finding the equipartition

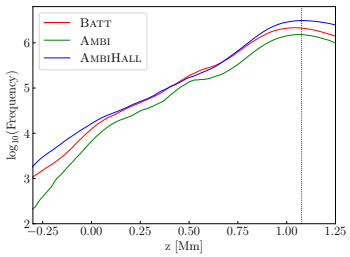

FIGURE 6.7— Horizontal cut of the two-dimensional histogram from Figure 6.5 for $\beta = 1$ (dotted line in Figure 6.5), showing the frequency of occurrence of points with $\beta = 1$ for the three runs. Black dotted line shows the height of maximum frequency of occurrence ($z = 1.1$ Mm) for the AmbiHall run. The addition of Hall term introduces a slightly higher amount of points with $\beta = 1$.

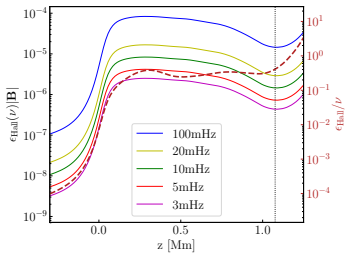

FIGURE 6.8— Hall parameter profile computed as Eq. 6.4 and normalized by the wave frequency ν (red dashed curve). The same quantity but normalized by $|\mathbf{B}|^{-1}$ is presented in solid lines for different frequencies. Vertical dotted line shows the position of the maximum occurrences of $\beta = 1$ for the AmbiHall run, this point coincides with an increase in the Hall parameter, and so with a possible increase of fast-to-Alfvén mode transformation via Hall term above this height.

level (see dotted vertical line). This behavior is different to the one modeled in Chapter 5, and is due to the particular field distribution in our model of convection. From the experiments performed in the Chapter 5 we know that the fast-to-Alfvén mode transformation due to Hall effect is a continuous process, which is enhanced where ϵ_{Hall} has large values, and whenever there are fast waves exist. Then, in AmbiHall run it is expected to show a more efficient mode transformation than in the simpler experiments done in the previous chapter. If we take into account the magnetic field of the stratification and calculate the Hall parameter in the frequency units, $\epsilon_{\text{Hall}}/\nu$, the small bump around the $\beta = 1$ locus disappears and the curve starts to grow indicating a higher mode transformation probability, see red dashed curve in Figure 6.8.

Another interesting quantity to analyze is the probability density function (PDF) for the magnetic field strength, as shown in Figure 6.9. This function has a connection to observational studies and represents the probability of, choosing a random point into the stratification at any time, to obtain what magnetic strength B_z it has. Our PDF functions display a similar shape and values to those obtained from similar simulations (Vögler & Schüssler 2007; Rempel 2014; Khomenko et al. 2017) or derived from observations, see Fig. 7b of Domínguez Cerdeña et al. (2006) as an example. It is interesting how the magnetic field strength distribution narrows when adding the ambipolar effect (middle panel) and becomes wider when adding it together with the Hall effect (right panel). This means that the Hall term increases the probability of stronger magnetic fields. Figure 6.10 shows a comparison between magnetic field PDF in the three runs at different geometrical heights, at $z = 0.5$ Mm on the right panel, and at photospheric level on the left panel. We see how adding ambipolar diffusion it decreases the probability for fields with $|\mathbf{B}| \gtrsim 1$ kG and how the incorporation of Hall effect does the opposite by increasing the probability of fields $|\mathbf{B}| \gtrsim 1$ kG, above the values given by those in the simulation without these effects.

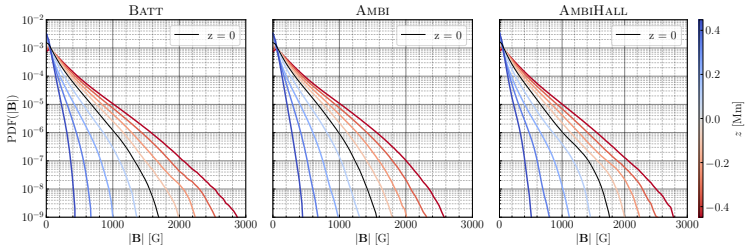

Figure 6.9— Probability density function (PDF) for the magnetic field at different geometrical heights for each simulation run. Red curves correspond to layers below the surface and blue curves above the surface. Black curve indicates the geometrical surface. The ambipolar term narrows the distribution (center panel). Adding the Hall term makes the PDF wider (right panel). Each curve is computed as an average of 60 km around its height.

6.4.2 Power maps

As we know from Chapters 2 and 4 the properties of the waves are conditioned by the medium where they propagate, and by the magnetic field topology. To study the wave behavior in an uniform medium, under the cool plasma approximation (zero-β plasma), and to separate the modes, Cally (2017) applies a Helmholtz decomposition of the displacement into irrotational and incompressive contributions using potential functions to represent the fast and Alfvén waves. Here we apply the same strategy having in mind that this decomposition can only distinguish between fast and slow magneto-acoustic waves when the plasma β is below 1. Alfvén waves can always be set apart, and this suits the purposes of our study. Therefore, by applying the above strategy to the velocity field, we compute the following quantities:

$$f_{\rm alfv} = \mathbf{e}_\parallel \cdot \nabla \times \mathbf{v} \,, \tag{6.5a}$$
$$f_{\rm fast} = \nabla \cdot \left(\mathbf{v} - \mathbf{e}_\parallel v_\parallel\right) = \nabla \cdot \mathbf{v}_\perp \,, \tag{6.5b}$$
$$f_{\rm long} = \mathbf{e}_\parallel \cdot \nabla \left(\mathbf{v} \cdot \mathbf{e}_\parallel\right) = \nabla_\parallel v_\parallel \,, \tag{6.5c}$$

where $v_\parallel$ is the velocity component parallel to the magnetic field, $\mathbf{v}_\perp$ the perpendicular one, and $\mathbf{e}_\parallel$ is a unit vector parallel to the magnetic field. These expressions can be written using the basis given by Equations (5.17) as

$$f_{\rm alfv} = \cos\phi \sin\theta \left(\frac{\partial v_z}{\partial y} - \frac{\partial v_y}{\partial z}\right) + \sin\phi \sin\theta \left(\frac{\partial v_x}{\partial z} - \frac{\partial v_z}{\partial x}\right) + \cos\theta \left(\frac{\partial v_y}{\partial x} - \frac{\partial v_x}{\partial y}\right) \,, \tag{6.6a}$$
$$f_{\rm fast} = \frac{\partial}{\partial x}\left(v_x - v_{\rm long}\cos\phi\sin\theta\right) + \frac{\partial}{\partial y}\left(v_y - v_{\rm long}\sin\phi\sin\theta\right) + \frac{\partial}{\partial z}\left(v_z - v_{\rm long}\cos\theta\right) \,, \tag{6.6b}$$
$$f_{\rm long} = \nabla \cdot \mathbf{v} - f_{\rm fast} \,, \tag{6.6c}$$

where $\mathbf{e}_\parallel = \mathbf{e}_{\rm long}$ and $v_{\rm long} = v_x \cos\phi \sin\theta + v_y \sin\phi \cos\theta + v_z \cos\theta$. These expressions are derivatives of the velocity and can help us to separate different wave modes. Taking into account the discussion from Section 2.5, $f_{\rm alfv}$ selects an incompressible perturbation along the magnetic field lines under any value of β and can be identified with Alfvén waves. $f_{\rm fast}$ selects a compressible perturbation perpendicular to the field lines, separating fast magneto-acoustic (mainly magnetic) mode in regions with low-β

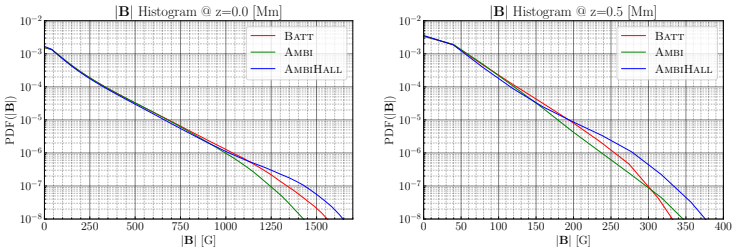

FIGURE 6.10— PDF comparison of the magnetic field. Left panel corresponds to geometrical photospheric level histogram for each simulation, see black curves of Figure 6.9. Right panel shows the curves at 0.5 Mm height. Ambipolar term reduces the probability of magnetic field respect to the single action of the Battery term, meanwhile adding the Hall term produces the opposite effect, see the curve bumps of both panels.

($\beta < 1$). $f_{\rm long}$ selects a compressible perturbation propagating along the field lines separating slow magneto-acoustic mode (mainly acoustic) in regions where $\beta < 1$.

We computed the quantities given by Eqs. (6.6) for all temporal instances in our models, and calculated their temporal Fourier transform to create a power as a function of frequency and three spatial coordinates for each of them. Next, we computed the spatial average of the power in the horizontal direction and obtain a two-dimensional power map as a function of height and frequency (z, ν). Finally to compare the simulations between them, we defined the function $F_i(z, \nu)$ as the ratio between the averaged power map of two different simulations

$$F_i(z,\nu) = \frac{\left\langle |\mathrm{FFT}\,(f_i)_{\rm R1}|^2 \right\rangle_{x,y}}{\left\langle |\mathrm{FFT}\,(f_i)_{\rm R2}|^2 \right\rangle_{x,y}}\,, \tag{6.7}$$

where the subscript i = {long, fast, alfv} indicates the projection and the superscripts (R1,R2) = {Batt, Ambi, AmbiHall} indicate the simulation. Of all the possible ratios we are interested in Ambi/Batt (AB), AmbiHall/Batt (AHB), and AmbiHall/Ambi (AHA). The first ratio (AB) allows to isolate the ambipolar effect, the second one (AHB) allows to study the joint action of the ambipolar and Hall terms, and finally the last ratio (AHA) allows to highlight the Hall effect. The saving cadence of 10 s allows us to resolve waves at high frequencies, up to 50 Hz, as we can see in the power map ratios shown in Fig. 6.11.

Figure 6.11 shows the power maps ratios defined by Eq. (6.7) from heights below the photospheric level to the lower chromosphere. Each column corresponds to a different power ratio, and each row corresponds to power ratios computed for a different quantity, see Eqs. (6.6). These power ratios give information about the amount of energy available at a given height and frequency depending of the action or not of the non-ideal terms. Regardless of the selected ratio, the power maps of $F_{\rm long}$ and $F_{\rm fast}$ are very similar since both quantities are related to compressible waves and the anisotropies along and across the magnetic field lines for these waves are not big enough to be noticeable due to the high plasma β values.

The left column of Fig. 6.11 shows the ratio AB. The values in the three panels are close to one for heights below 0.5 Mm, meaning the absence of energy imbalance. Above this height there is a clear dependence on frequency. As can be seen in panels (a) and (d) there is more contribution to the power

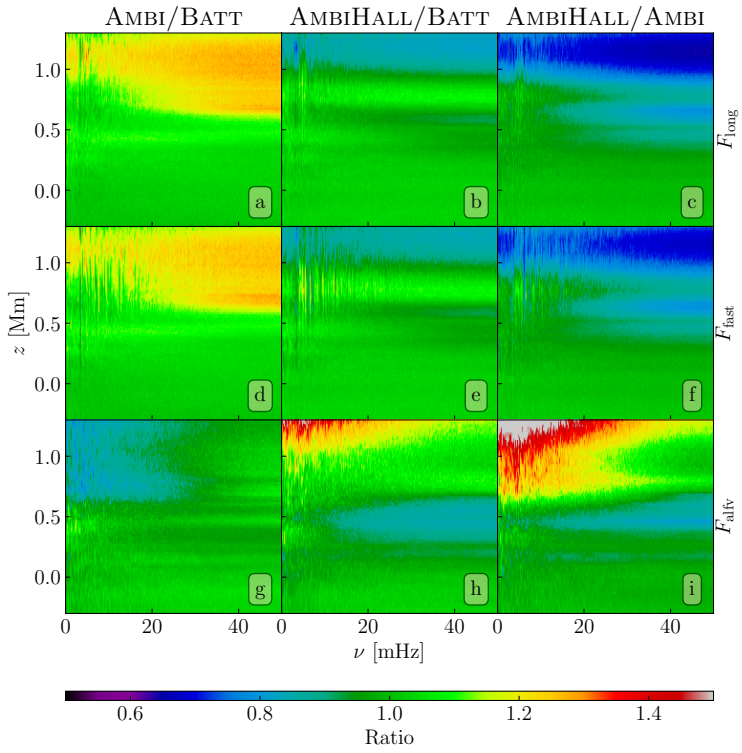

FIGURE 6.11— Power map ratios obtained with Eq. (6.7). Rows correspond to the projections and columns select the ratio between simulations.

coming from the ambipolar effect above 1 Mm at low frequency. As we move towards higher frequencies this imbalance extends to lower layers increasing slightly its magnitude. In the panel (g) the situation is the opposite, there is a lack of energy in the region above 0.5 Mm at all frequencies between 0 and ∼20 mHz, and at higher frequencies the imbalance disappears. This can be interpreted as a hint that ambipolar diffusion not only changes the configuration of the magnetic field as Leake & Arber (2006) or Arber et al. (2007) found in a 2.5D first and 3D magnetic flux emergence simulations later, but also changes the efficiency of mode transformation as it were found by Cally & Khomenko (2018), reducing in this case the Alfvén wave generation bellow 20 mHz. When the Hall term is switched on, see middle column of Fig. 6.11, we see a clear depression of energy in panels (b) and (e) above 1 Mm with a slight increase between 0.5 and 1 Mm at all frequencies. Panel (h) on the other hand, shows an energy increase at low frequencies ($\nu \lesssim 20$ mHz) above 1 Mm and a depression around 0.5 Mm for frequencies bigger than 10 mHz. To see the effects introduced by the Hall term, we show on the right column the ratio AHA, here it is more pronounced the lack of energy above a 1 Mm in $F_{\rm long}$ and $F_{\rm fast}$ and the excess in $F_{\rm alfv}$.

Another interesting quantity to study is the electromagnetic Poynting flux, which is defined as:

$$\mathbf{S} = \frac{\mathbf{E}\times\mathbf{B}}{\mu_0} = -\frac{(\mathbf{v}\times\mathbf{B})\times\mathbf{B}}{\mu_0} - \frac{\mathbf{B}\times(\eta_A\mathbf{J}_\perp)}{\mu_0} - \frac{|\mathbf{B}|^2\mathbf{J}_\perp}{en_e\mu_0} - \frac{\nabla p_e\times\mathbf{B}}{en_e\mu_0}\,. \tag{6.8}$$

From left to right, the contributions are coming from the ideal term ($\mathbf{S}_{\rm I}$), the ambipolar diffusion term ($\mathbf{S}_{\rm A}$), the Hall term ($\mathbf{S}_{\rm H}$), and the Battery term ($\mathbf{S}_{\rm B}$). The contribution from the Battery term to the Poynting flux is expected to be small. The difference between simulations with or without the other two non-ideal effects will be therefore conteined into $\mathbf{S}_{\rm A}$ and $\mathbf{S}_{\rm H}$ and will affect the values of $\mathbf{S}_{\rm I}$. For these reasons we neglect the battery contributions and focus into comparing the ideal contribution to the Poynting flux in different simulations.

This ideal contribution can be split into a horizontal and vertical components. We are interested in the vertical component of the ideal Poynting flux vector $S_z^{\rm ideal}$ which is defined as:

$$S^{\rm ideal}_{z,\rm total} = \frac{v_z(B_x^2+B_y^2) - B_z(v_xB_x+v_yB_y)}{\mu_0} = \frac{v_zB_h^2}{\mu_0} - \frac{B_z(\mathbf{v}_h\cdot\mathbf{B}_h)}{\mu_0} = S^{\rm ideal}_{z,\rm emerg} + S^{\rm ideal}_{z,\rm shear}\,, \tag{6.9}$$

and has two contributions, the first one $S^{\rm ideal}_{z,\rm emerg}$ represents the transport of horizontal magnetic field variations due to the vertical velocity, and the other one, $S^{\rm ideal}_{z,\rm shear}$ is due to the horizontal shear motions of the magnetized plasma along vertical flux tubes. It is now possible to construct the power map ratio between simulations for these two quantities, as it was done previously with the proxies given by Eqs. (6.6). Expression (6.10) summarizes the calculation:

$$G_j(z,\nu) = \frac{\left\langle \left|{\rm FFT}\left(S^{\rm ideal}_{z,j}\right)_{\rm R1}\right|^2\right\rangle_{x,y}}{\left\langle \left|{\rm FFT}\left(S^{\rm ideal}_{z,j}\right)_{\rm R2}\right|^2\right\rangle_{x,y}}\,, \tag{6.10}$$

where subscript $j = \{\rm total, emerg, shear\}$ indicates the projection and again, the superscripts (R1,R2) = {Batt, Ambi, AmbiHall} denote the simulation. The results are shown in Fig. 6.12.

Figure 6.12 shows the power maps ratios defined by expression (6.10) from just below the photospheric level to the lower chromosphere, columns correspond to the ratio between different simulation, first row corresponds to the ratio associated to the quantity defined by expression (6.9) and the other two rows are for $S^{\rm ideal}_{z,\rm emerg}$ and $S^{\rm ideal}_{z,\rm shear}$. These power maps tell us not only about the amount of energy

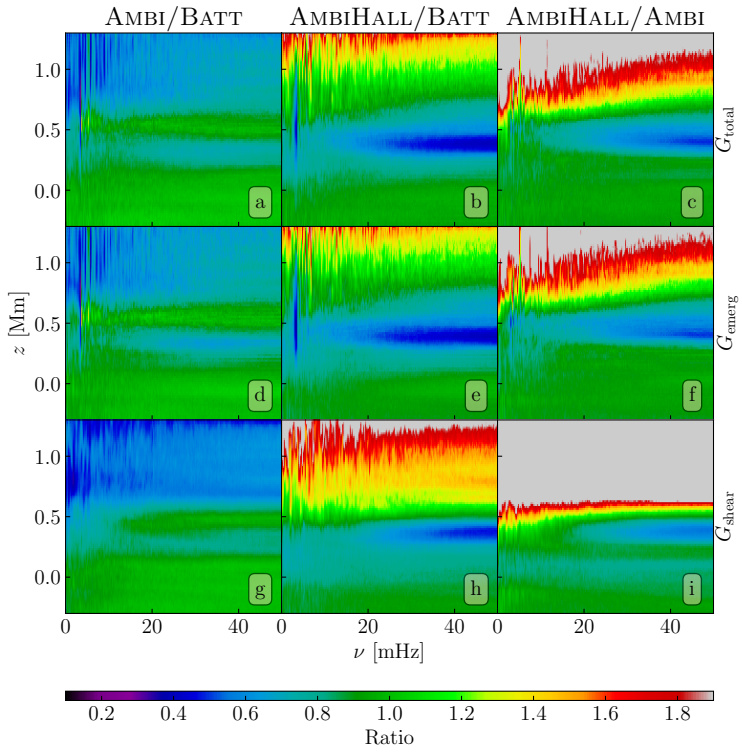

FIGURE 6.12— Power map ratios obtained with Eq. (6.10). Rows, from top to bottom correspond to the total Poynting flux and its two contributions, emergent and shear ones. Columns provide the ratio of the fluxes between three pair of simulations.

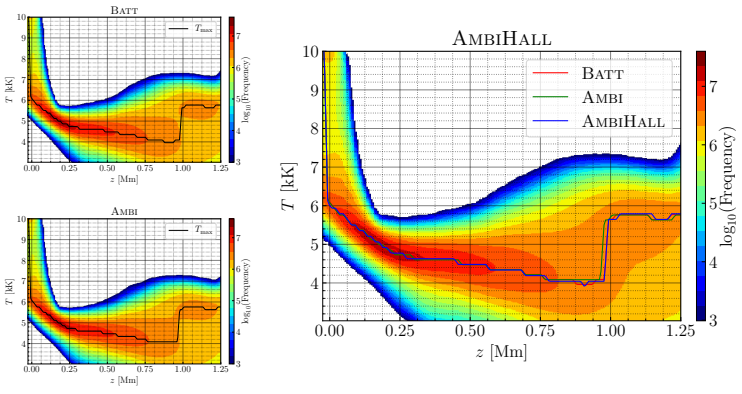

Figure 6.13— Two-dimensional histograms showing the number of points with a given value of temperature at certain height. Solid curves indicates the maximum of the frequency of occurrence for each run. The addition of the ambipolar term increases the amount of locations with higher temperature (light orange) at $z \sim 1$ Mm. Adding the Hall term increases even more the area cover by higher temperature values, also produces a slightly upward displacement of the maximum frequency curve respect to the Ambi run values just below 1 Mm height, see panel on the right.

but also how the energy is propagating at given frequencies and heights. Same as before, the stratification is cut below the photosphere since all the ratios are close to one and do not show a significant structure. Left column shows the ratio AB. The most significant feature here is the lack of energy of the Ambi run respect the Batt run in the upper layers of the atmosphere, being more prominent at low frequencies ($\nu \lesssim 10$ mHz). In panel (g) this energy depression is bigger than in panel (a) and (d), and the depression extends to higher frequencies. The flux absorption agrees with the results found by Shelyag et al. (2016), causing the heating of those layers. The middle column shows the ratio AHB and manifests an opposite behavior due to the addition of the Hall term. Then, Hall term helps to increase the amount of magnetic energy in the chromosphere, working against the ambipolar diffusion which is still dissipating that energy flux and then heating those layers. The column on the right separates the Hall effect from both ambipolar and Battery effects, showing saturated values in all three panels and, especially prominent for the shear flux ratio, shown in the panel (i), at heights as low as 0.5 Mm.

6.4.3 Heating properties

The lack of Poynting flux could mean that some amount of energy has been converted into internal energy increase. In order to check if this heat results in a temperature increase, we plot the two-dimensional histograms of the temperature distribution with height, see Figure 6.13. The heating term due to the ambipolar diffusion, $\eta_A J_\perp^2$, is given in Figure 6.14. The histograms include all spatial points of the complete temporal series of each run. The shape of the histograms are very similar, but there are some differences. Adding the ambipolar term produces a heating around 0.8–0.9 Mm and a displacement towards deeper layers of the temperature jump around 1 Mm similarly to Khomenko et al. (2018). Though, adding the Hall term induces a slightly cooling around 0.8 Mm and a appreciable displacement upward of the temperature jump around 1 Mm respect the Ambi run. This heating due

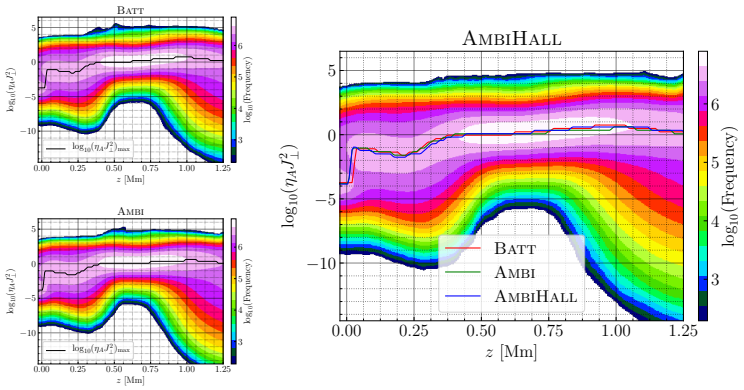

Figure 6.14— Two-dimensional histograms showing the number of points with a given value of the heating term as a function of height. Solid curves indicate the location of the maximum of the frequency of occurrence for each run. The addition of the ambipolar term increases the width of histogram above $z \sim 1$ Mm. Adding the Hall term increases the area cover by values around 6.5 (light purple and white areas), see plot on the right.

to the ambipolar and Hall terms can be see in Figure 6.14. This Figure shows the histograms for the three runs. The left column gives the results for the Batt and Ambi runs. It can be seen how the addition of the ambipolar term increases the width of the colored area, specially for heights above 1 Mm. When adding the Hall term, the width of the histogram is reduced slightly but the area covered by values over 6 (purple region) increases, see the light purple area corresponding to the AmbiHall run. This heating due to ambipolar diffusion arises as an increase of temperature, see the orange areas for each run in Figure 6.13.

Doing the horizontal average of the vertical magnetic field at each time step and height it is easy to see how the addition of ambipolar diffusion changes the structure and strength of the magnetic field with respect to the Batt run, see the middle and the left panels in Figure 6.15. The ambipolar term dissipates magnetic energy, which produces a general reduction of B_z component in the numerical box, see middle panel in Figure 6.15, the yellow regions are less decrease and the blue ones even more frequent. On the other hand, the Hall term is a dispersive term so it does not heat the atmosphere, however, it can change the structure of the magnetic field by generating additional currents. These currents then can contribute to the heating by its dissipation through the ambipolar term. The right panel of Fig. 6.15 shows how the Hall term increases the average vertical magnetic field in the numerical box above 0.5 Mm compared to the Ambi run, see the the greater area cover by green color on the right panel. If we suppose that the change in temperature and density are small between the runs, then it is possible to explain the increment of the ambipolar and battery coefficients above 0.5 Mm in the AmbiHall run by an increment, in average, of the magnetic field strength at these heights, see Figures 6.16 and 6.17. The Ambi run shows the opposite behavior.

Going back to the spatio-temporal average of the magnetic field, Figure 6.18 shows again that above 0.5 Mm, the average of magnetic field for AmbiHall run is higher than that for the Ambi run

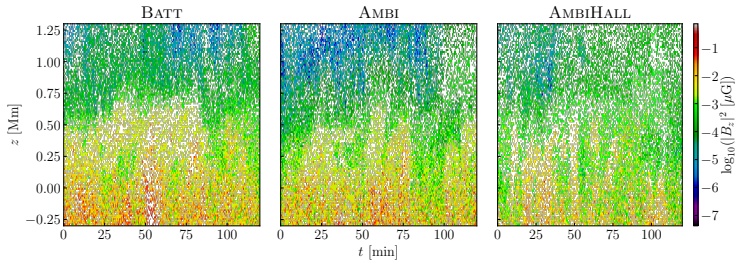

Figure 6.15— Vertical magnetic field averaged in the horizontal plane as function of height and time. Adding the Hall term results in stronger magnetic fields reaching higher heights of the atmosphere, see the greater area covers by green values in the right panel.

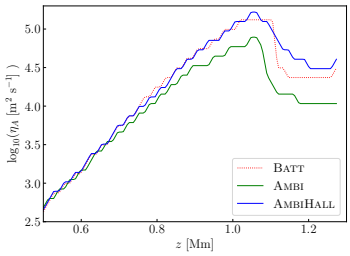

Figure 6.16— Ambipolar diffusion coefficient profiles calculated as the maximum frequency of occurrence at each height. The red dotted line indicates that the Batt run has no ambipolar diffusion activated but it is possible to calculate using the stratification parameters.

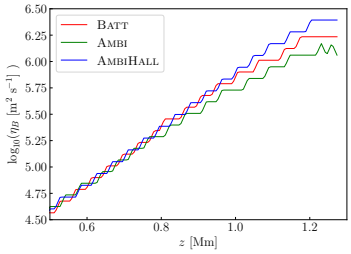

Figure 6.17— Battery coefficient profiles calculated as the maximum frequency of occurrence at each height.

or that for the Batt run in higher heights. If the average is done only for the fields which have an absolute value for the vertical component, B_z, above 1 hG, 5 hG, or 1 kG correspondingly, we see how adding the ambipolar term makes that the magnetic field with $|B_z| \geq 1$ hG reaches lower heights than when no ambipolar term is considered. However, taking into account also the Hall term, this behavior is inverted and stronger magnetic fields reach higher heights. Doing the same analysis with the magnetic field inclination, Figure 6.19, we can see that when the Hall term is switched on, not only stronger magnetic fields reach higher layers, but also that those fields are less inclined (the field is more vertical). This will affect the propagation of waves and energy to the upper layers.

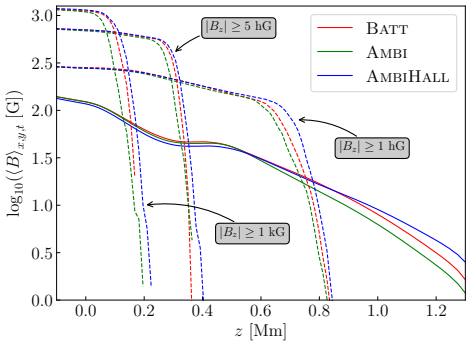

FIGURE 6.18— Magnetic field averaged in the horizontal plane and time as function of height (solid curves). Red color correspond to the simulations considering only the Battery term, green curves to the simulations adding the ambipolar term, and blue curves to the simulations including also the Hall term. Dashed curves shows the average calculated taking into account those magnetic field with a condition over the vertical component of the magnetic field, see the boxes for details. Hall term increases the magnetic field strength at higher layers respect the Battery and/or ambipolar term simulations.

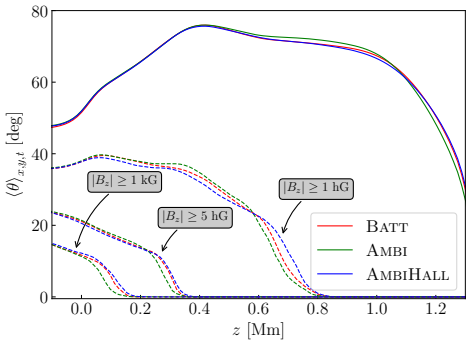

FIGURE 6.19— Inclination angle averaged in the horizontal plane and time as function of height (solid curves). Red color correspond to the simulations considering only the Battery term, green curves to the simulations adding the ambipolar term, and blue curves to the simulations including also the Hall term. Dashed curves shows the average calculated taking into account the angles which satisfy the condition over the vertical component of the magnetic field indicated into the boxes. The main contribution to horizontal magnetic fields came from weak magnetic fields ($|B_z| <$ 100 G). Hall term increases the height at which the vertical magnetic field reach respect the Battery and/or ambipolar term simulations.

6.4.4 High frequency oscillation

After exploring the energy flux and how the magnetic field structure is affected by both ambipolar and Hall terms we can calculate the power spectrum map for both, the velocity projections and the vertical Poynting flux to study correlations between those power maps and other quantities. Since the granulation pattern is changing in time scales of a few minutes it is not possible to make correlations using the whole temporal series. Thus, we have computed the one minute average power maps of the velocity projections and the vertical Poynting flux and study high frequencies. For each run, we have chosen the snapshot at $t' \sim 4.11$ h after $t_{\rm ini}$, which corresponds to ~ 246 min after switching on the Hall term in the AmbiHall run. We have chosen this time to be sure of being in a saturation regime for the Hall term and make comparisons with the other two runs. For the average we have used seven

points, this is, the average is computed taking three snapshots after and before the chosen time t' (30 s before and 30 s after the selected snapshot). For the velocities projections the average is computed as

$$\mathcal{P}_i(x,y,z) = \sum_\nu \left| \mathrm{FFT}\Big[f_i(x,y,z,t_n) \Big] \right|^2 , \tag{6.11}$$

and for the Poynting flux is computed as

$$\mathcal{P}_j(x,y,z) = \sum_\nu \left| \mathrm{FFT}\left[S^{\mathrm{ideal}}_{z,j}(x,y,z,t_n) \right] \right|^2 , \tag{6.12}$$

where i = {long, fast, alfv}, j = {total, emerg, shear}, and n={-3,-2,-1,0,1,2,3}.

Figure 6.20 shows a horizontal cut at three different geometrical heights of the one minute averaged power spectrum for the velocity projections f_{fast} (left column) and f_{alfv} (right column), given by Equations (6.5a) and (6.5b). These panels correspond to the AmbiHall simulation. At photospheric level, see bottom row, the observed pattern is clearly granular. High power regions (red-white colors) are associated to strong magnetic fields, regions in black) with a magnetic field intensity between 200 G and 1 kG. These regions are located in the intergranular lanes, where the magnetic field is advected and compressed by convective motions. Notice that those black regions, for $\mathcal{P}_{\mathrm{fast}}$ coincide with regions with power $\mathcal{P}_{\mathrm{fast}} \sim 10^{-2}$ (yellow). For $\mathcal{P}_{\mathrm{alfv}}$, stronger magnetic field regions coincide with regions with higher power, $\mathcal{P}_{\mathrm{alfv}} \sim 1$ (red-white colors). The intergranular regions have less power of $\mathcal{P}_{\mathrm{fast}}$ associated. Moving upwards to the temperature minimum height, $z = 0.5$ Mm, middle row, the granulation pattern vanish and the regions with magnetic field between 50 and 200 G are related to low $\mathcal{P}_{\mathrm{fast}}$ power regions (blue) and high $\mathcal{P}_{\mathrm{alfv}}$ power regions (red). Similar behavior is found at 1 Mm, top row, for regions with a magnetic field between 15 and 50 G.

Figure 6.21 shows horizontal cuts of the one minute averaged power spectrum for the vertical Poynting flux contributions, $\mathcal{P}_{\mathrm{emerg}}$ on the left column and $\mathcal{P}_{\mathrm{shear}}$ on the right one, see Equation (6.9). Each row corresponds to a different height as in the previous figure. The time average was computed as previously, ~ 246 min after switching on the Hall term. At photospheric level (bottom row) $\mathcal{P}_{\mathrm{emerg}}$ shows a slightly higher power than $\mathcal{P}_{\mathrm{shear}}$ but both contributions show the characteristic granulation pattern and the concentrations of magnetic field with intensities between 200 G and 1 kG are associated to the intergranular lanes. At 0.5 Mm (middle row) the granulation pattern vanishes in both contributions but the regions with magnetic field between 50 and 200 G are still related to the high power regions. Despite $\mathcal{P}_{\mathrm{emerg}}$ distribution correlates better with high power distributions, the peaks of power are stronger in $\mathcal{P}_{\mathrm{shear}}$, see for example the coordinates $(x, y) \sim (2.8, 4.7)$ Mm and $\sim (5, 2.9)$ Mm. Higher up in the atmosphere, at 1 Mm (top row), we still have associated the high power regions with high magnetic fields as it is shown by the black areas.

With this information it is possible to plot some dispersion diagrams to search for correlations and to have a better understanding about the effect of introducing the Hall term. Figure 6.22 shows the averaged power spectrum of f_{alfv} correlated to the magnetic field at three different heights, $z = 0, 0.5$, and 1 Mm. At the photospheric level and at $z = 0.5$ Mm, the three runs are very similar, but at 1 Mm the Batt run has a peak in occurrence frequency located around 10–50 G. By adding ambipolar diffusion, this peak is smoothed, the Hall term increases slightly this frequency between $z = 0.5$ and 1 Mm. It means that f_{alfv} component can be more frequently found over fields of 10–50 G. The behavior is similar in Figure 6.23, but the Hall term adds a small linear tendency to the data when the height increases: the bigger the magnetic field is, the smaller is the power. Figure 6.24 corresponds to the averaged power spectrum for the shear contribution to the Poynting flux correlated to the magnetic field intensity at the three different heights. This figure shows a linear correlation with the magnetic

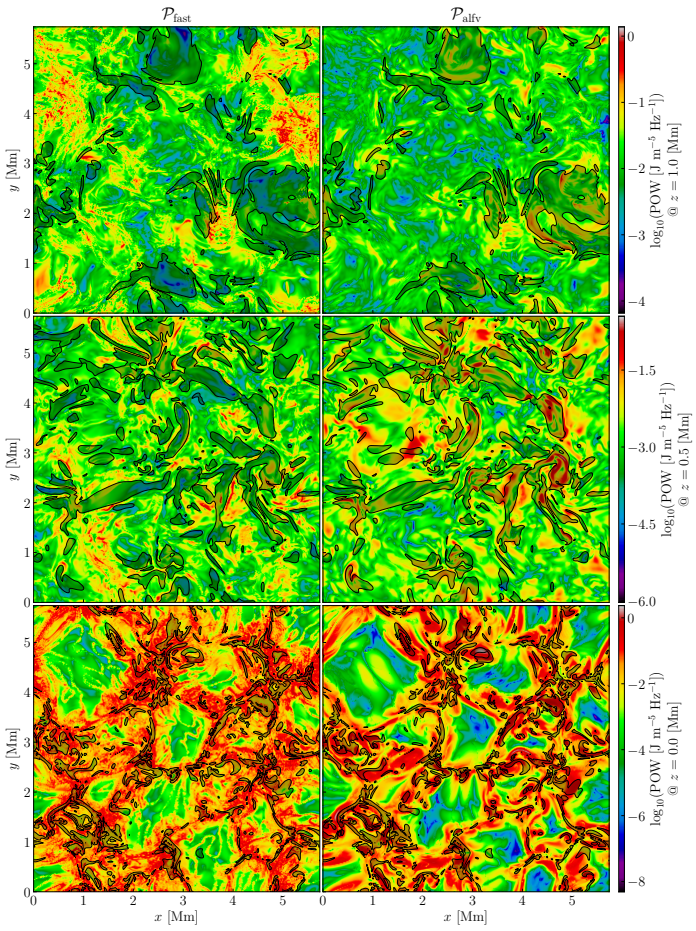

FIGURE 6.20— Horizontal cuts of the one minute averaged power spectrum for the velocity projections $f_{\rm fast}$, left panel, and $f_{\rm alfv}$, right panel, in the AMBIHALL run. The black area indicates regions with magnetic field intensity between 200 and 10^3 G at $z = 0$ Mm, between 50 and 200 G at $z = 0.5$ Mm, and between 15 and 50 G at $z = 1$ Mm. The magnetic field intensity is computed at t'.

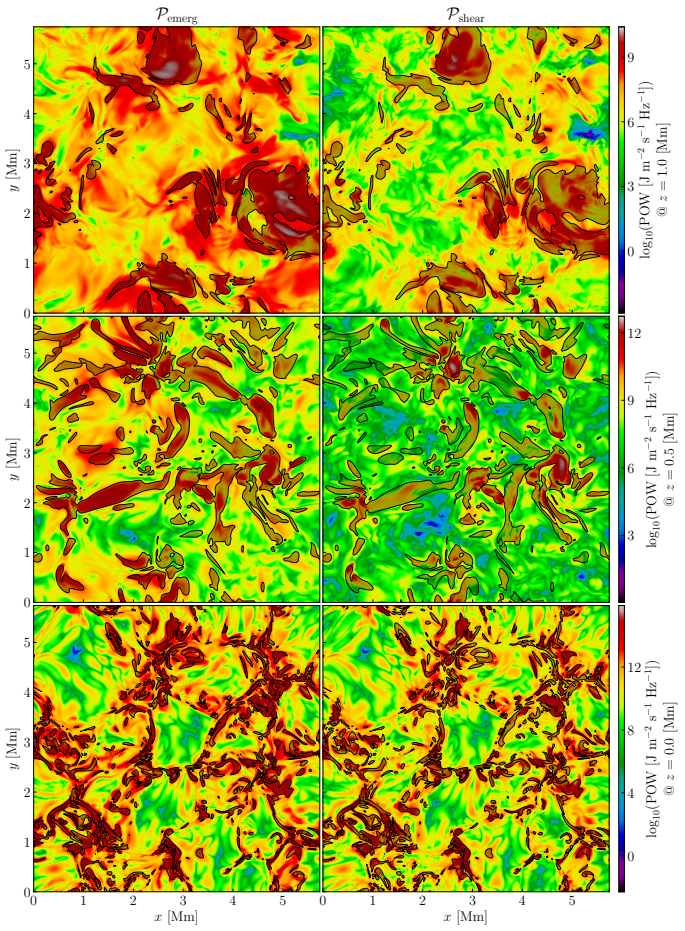

FIGURE 6.21— Horizontal cuts of the one minute averaged power spectrum for the emergent part of the Poynting flux, $S_{\rm emerg}$, left panel, and the shear part, $S_{\rm shear}$, right panel in the AMBIHALL run. The black area indicates regions with magnetic field intensity between 200 and 10^3 G at $z = 0$ Mm, between 50 and 200 G at $z = 0.5$ Mm, and between 15 and 50 G at $z = 1$ Mm. The magnetic field intensity is computed at t'.

field: the bigger the magnetic field is, the bigger is the power. It is interesting how Hall term adds shear power at all cuts, specially at the photospheric level and, above all, to the higher layers ($z = 1$ Mm). This means that the Hall term induces horizontal shear movements of the plasma along the vertical flux tubes.

To investigate a bit further the heating properties of the simulations, Figures 6.25 and 6.26 shown the correlation between the heating term $\eta_A J_\perp^2$, which appears in the internal energy equation (2.56), and the averaged power spectrum of both contributions, $\mathcal{P}_{\rm emerg}$ and $\mathcal{P}_{\rm shear}$, to the vertical component of the Poynting flux at three different heights. As can be seen from Eqs. (2.38), (2.48), and (2.49) the ambipolar coefficient gets larger in regions where the density and temperature are low, and the magnetic field is large. Meanwhile, from Eqs. (2.45) and (2.46), the perpendicular currents depend on the magnetic field complexity, getting larger when it increases. This heating term then gives a conversion efficiency between magnetic energy and thermal energy through the dissipation of perpendicular currents (Khomenko & Collados 2012; Khomenko et al. 2018). Comparing the three columns in Figure 6.25, at 1 Mm it is clear that the ambipolar term increases the number of points in the domain for a certain emergence contribution to the Poynting flux and heat, see blue points in panel (b). Meanwhile, adding the Hall term decreases slightly this frequency but also assembles and shifts to the right the distribution, see panel (c). This effect can also be seen at 0.5 Mm, panel (f). In Figure 6.26 we observe how adding the Hall term the contribution to the Poynting flux to the heat is coming from the shear term, see panels (c) and (f). Thus, the main contribution to the power when adding the ambipolar term, comes from the emergent part of the Poynting flux, and when adding the Hall term, it comes from shear part. Finally, Figure 6.27 shows that adding the ambipolar term, the number of points with temperatures around 5600 K at $z = 1$ Mm increases and, adding also the Hall term this frequency increases even more meaning that this term also contributes to the chromospheric heating despite it is a dispersive term. It can be seen that this heating does not contribute as much to a net increase of the average temperature, but instead to the increase the probability of having points with high temperature at different times.

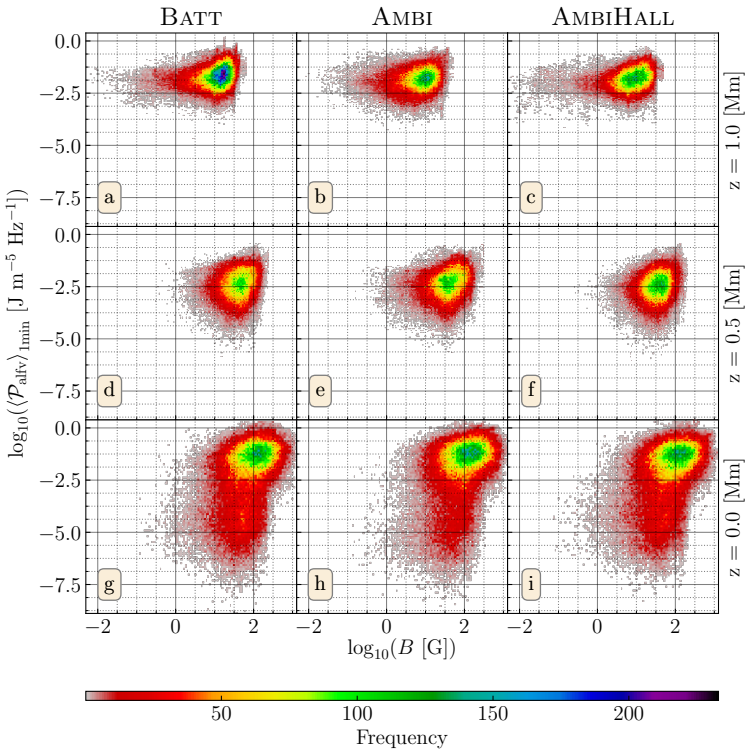

Figure 6.22— Two-dimensional histograms showing correlation between magnetic field and the one minute average power for the Alfvénic projection for the velocity field. Hall term produces a slight grouping of the high intensity magnetic fields at higher layers.

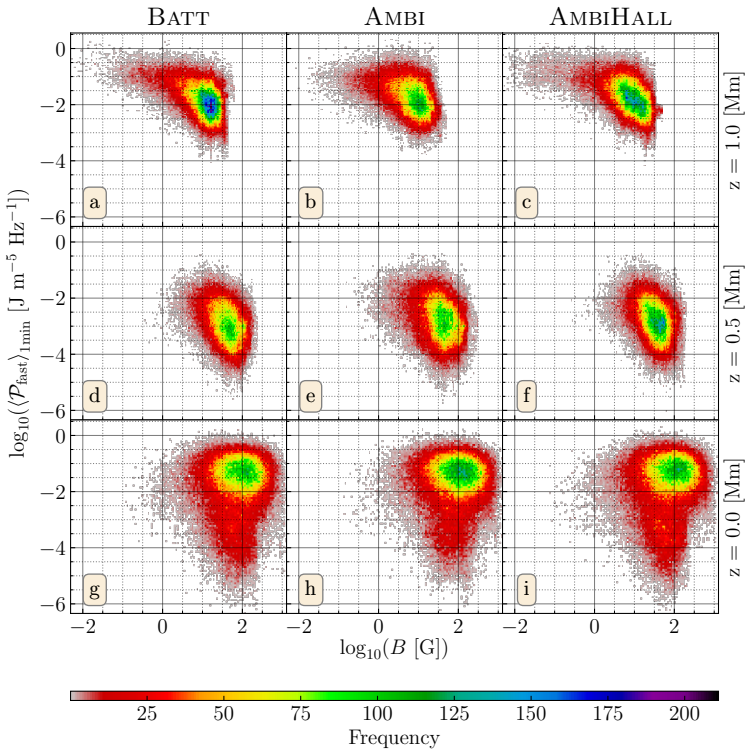

FIGURE 6.23— Two-dimensional histograms showing correlation between magnetic field and the one minute average power for the fast projection for the velocity field.

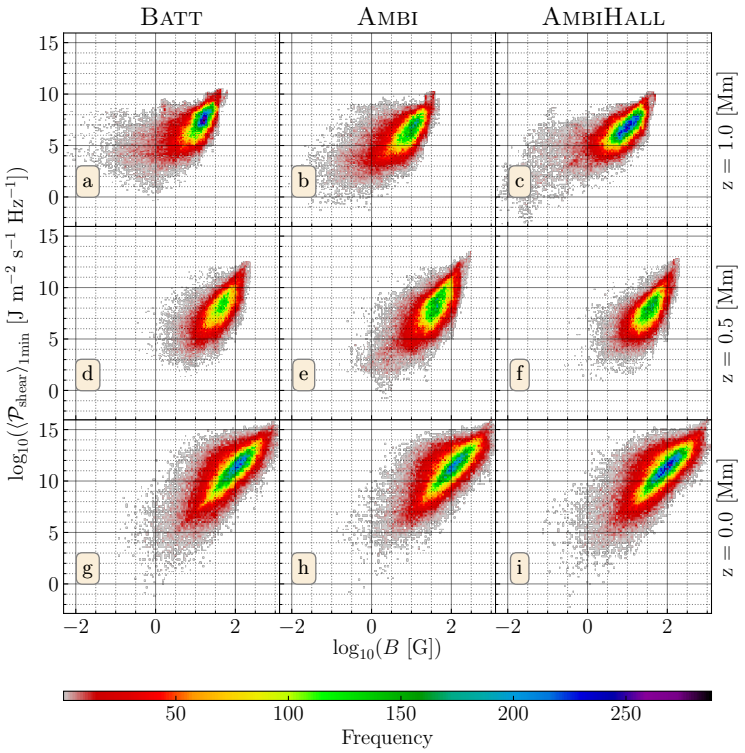

FIGURE 6.24— Two-dimensional histograms showing correlation between the magnetic field and the one minute average power for the shear part of the Poynting flux. It shows a linear correlation between them: the bigger the magnetic field is, the bigger the shear part is.

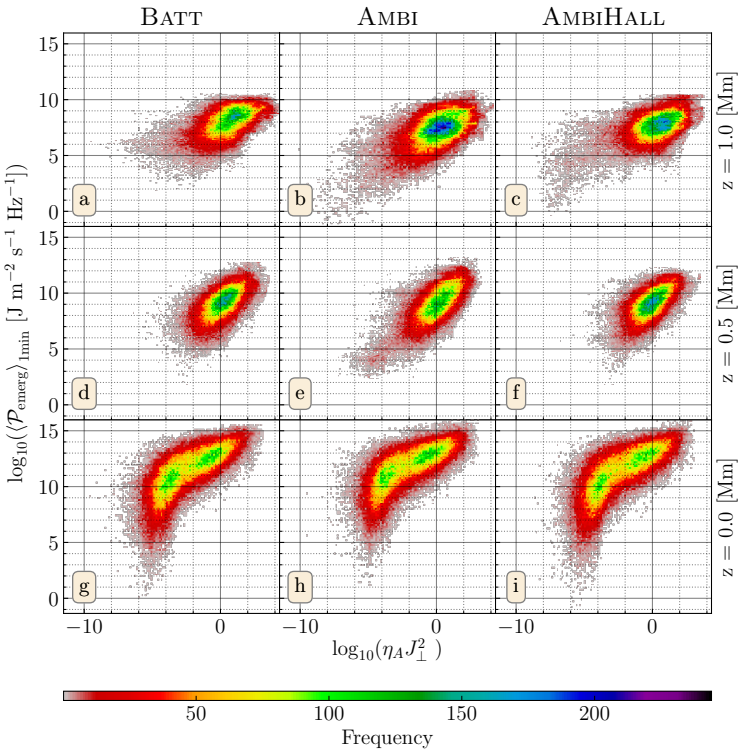

FIGURE 6.25— Two-dimensional histograms showing correlation between heat ($\eta_A J_\perp^2$) and the one minute average power for the emergent part of the Poynting flux. Hall term increases the frequency of occurrence above the photospheric level (right row).

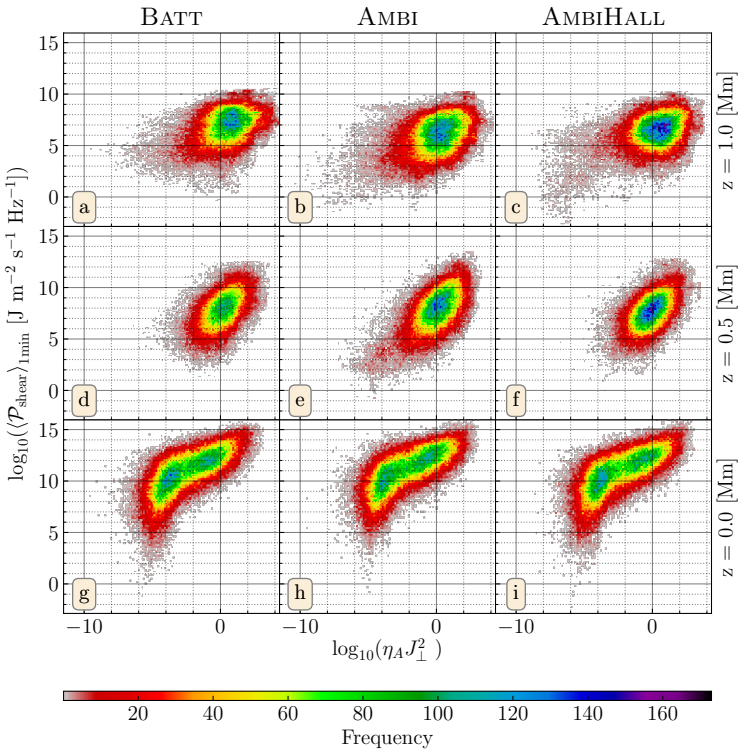

FIGURE 6.26— Two-dimensional histograms showing correlation between heat ($\eta_A J_\perp^2$) and the one minute average power for the shear part of the Poynting vector. Hall term increases the frequency of occurrence above the photospheric level, blue points in the right row, panels (c) and (f).

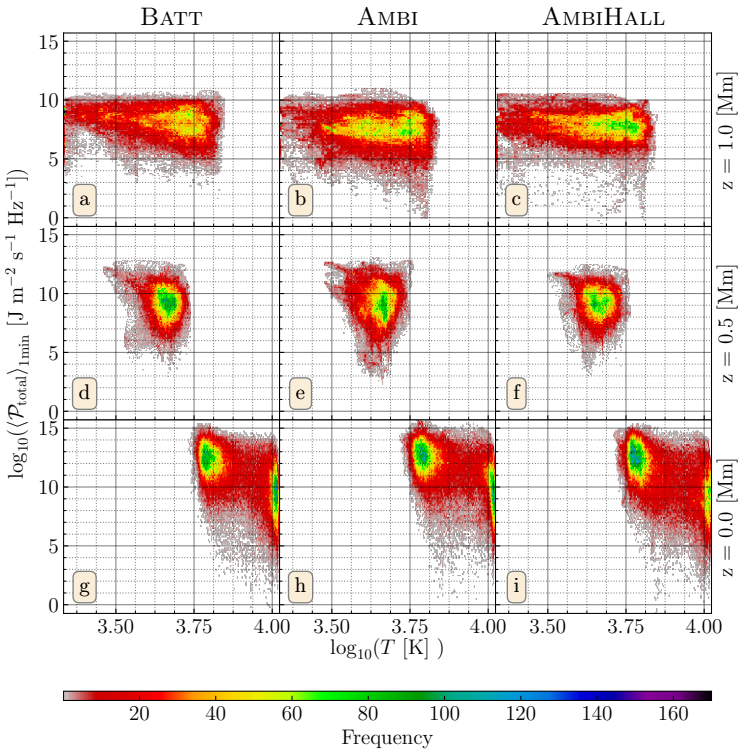

FIGURE 6.27— Two-dimensional histograms showing correlation between temperature and the one minute average power for the vertical component of the Poynting flux. Hall term produces a slightly increase of the temperature occurrences at higher layers, see panel (c).

6.5 Conclusions

In this Chapter, we have presented three dimensional simulations of solar magneto convection spanning from the upper convection zone up to the low chromospheric layers including non-ideal effects due to the presence of neutrals in the solar plasma. These are the first realistic three-dimensional magneto convection simulation taking into account the Hall effect. All simulations where done by keeping the same numerical setup except for the non-ideal terms, which were included/removed to make statistical comparisons between them.

Once the convection is established and Battery term is switched on, due to the misalignment between the pressure and density gradients, a small magnetic field appears in the stratification. Then due to a local dynamo effect it grows and saturates to solar values. The convective motions are generating magneto-acoustic waves which propagate into the plasma. Those waves are refracted, reflected, and transform while they spread. Into the stratification the geometrical mode transformation occurs around the equipartition layer. This region is changing its position and shape constantly due to the dynamic motions of the plasma and magnetic field. As a consequences this mode transformation is happening in several places and not in a static layer as the VAL-C model suggests. Because the plasma is partially ionized non-ideal effects as ambipolar diffusion or Hall effect arise and their action change the atmospheric structure creating a magnetic canopy very similar to the observed HIFs. Ambipolar diffusion dissipates Alfvénic waves and the magnetic Poynting flux decreases, thus the magnetic energy is converted into thermal energy. Meanwhile, the Hall term introduces a fast-to-Alfvén mode transformation coupling fast magneto-acoustic waves and Alfvén waves. This coupling occurs where the wave vector is nearly aligned to the magnetic wave vector and its efficiency increases around places where the Hall parameter ϵ_{Hall} and the amount of fast magneto-acoustic waves are high, this is, in regions with low magnetic field strength, $\beta \approx 1$, and for high frequency waves. In average this happens into our stratification around 1 Mm and above, however in other atmospheric configuration will be different. Slow magneto-acoustic modes rapidly shock and mitigate, fast modes refract and reflect but Alfvén waves can reach upper layers due to their incompressible nature. If we also consider that the Hall term not only generates currents, which can be dissipated by the ambipolar diffusion, but also increases the number of magnetic vortices, which can act as waveguides, we have an attractive mechanism formed by a closed cycle capable to transport and dissipate energy along the chromosphere and up to the solar corona, contributing this way to the atmospheric heating.

In summary:

In our experiments, the convective motions excite waves which propagate through the stratification reaching chromospheric layers confirming the results obtained by Khomenko et al. (2018) concerning the action of the ambipolar diffusion, this is, the ambipolar diffusion affect significantly the wave amplitudes and the wave modes, depending on height and frequency. When the Hall term is included in the simulations, it plays an important role by changing the magnetic field structure allowing the existence of stronger and more vertical fields at higher layers. It also introduces a non-geometrical way to transform fast magneto-acoustic waves into Alfvén waves increasing the currents variations. These currents are dissipated by the ambipolar term with the consequent heating of the atmosphere and also on the increase of the probability of finding more points with high temperature at chromospheric layers over the simulation time.

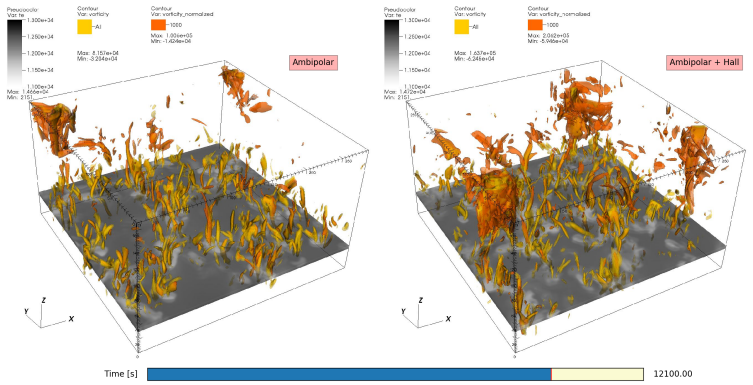

FIGURE 6.28— Plasma regions identified as vortices for AMBI run (left panel) and AMBIHALL run (right panel). Yellow iso-contours correspond to regions where $Q > 0$, orange correspond to iso-contours which satisfy the magnetic Q-criterion, $Q_\beta > 0$. The snapshots show the regions defined as vortices ~ 3.36 h after the addition of the Hall term. The AMBIHALL run shows a larger number of vortices regions, which can be working as waveguides for Alfvén waves and then making easier for them to reach upper layers of the solar atmosphere.

6.6 Outlook

Vortex detection

To continue the analysis of the consequences of adding the Hall term we are looking for vortex structures using pure hydrodynamic tools. In a fluid it is possible to calculate the stress tensor $D_{ij} = \partial v_{ij}/\partial x_{ij}$ and as any second order tensor, it can be decomposed into a symmetric S_{ij} and skew-symmetric Ω_{ij} parts where

$$D_{ij} = S_{ij} + \Omega_{ij} \,, \tag{6.13}$$

and

$$S_{ij} = \frac{1}{2}\left(\frac{\partial v_i}{\partial x_j} + \frac{\partial v_j}{\partial x_i}\right) \,, \tag{6.14}$$

$$\Omega_{ij} = \frac{1}{2}\left(\frac{\partial v_i}{\partial x_j} - \frac{\partial v_j}{\partial x_i}\right) \,. \tag{6.15}$$

The symmetric part is known as the strain-rate tensor and tells us about the rate of change of the deformation which is experienced by a material around a spatio-temporal point $\mathbf{p} = (\mathbf{r}, t)$. The skew-symmetric part is the vorticity vector and tells us about the rigid-like rotation experienced by the material at the point $\mathbf{p}$. From the characteristic equation for $\nabla\mathbf{u}$, given by

$$\lambda^3 + P\lambda^2 + Q\lambda + R = 0 \,, \tag{6.16}$$

it is possible to calculate the three invariant quantities P, Q, and R as follows.

$$P = -\operatorname{tr}(\nabla \mathbf{v}) \,, \tag{6.17a}$$

$$Q = \frac{1}{2}\left[\operatorname{tr}(\nabla \mathbf{v})^2 - \operatorname{tr}\left((\nabla \mathbf{v})^2\right)\right] = \frac{1}{2}\left(\|\overline{\Omega}\|^2 - \|\overline{S}\|^2\right) \,, \tag{6.17b}$$

$$R = -\det(\nabla \mathbf{v}) \,. \tag{6.17c}$$

Q_β-criterion

Based on these equations, Hunt et al. (1988) identify a vortex in an incompressible flow as an adjoined fluid region with a positive second invariant of the velocity gradient tensor ($Q > 0$). That is, as the regions where the vorticity tensor norm predominates over the strain-rate tensor norm. In addition it, is required that inside the vortex region the pressure to be less than the pressure outside (Kolář 2007). Because our fluid is a partially ionized magnetized plasma we normalize the second invariant of $\nabla \mathbf{v}$ by the plasma beta, highlighting in this way the magnetic regions and defining the magnetic Q-criterion as

$$Q_\beta = \frac{Q}{\beta} > 0 \,. \tag{6.18}$$

These magnetized vortices could be working as waveguides for the Alfvén waves, generated through the mode transformation, both the geometrical and non-geometrical. Then these waves can transport energy easier to upper chromospheric and coronal layers.

Extra comments

Another interesting improvement that can be introduced into the simulations is the consideration of a larger number of frequency bins to solve the radiative transfer equations or extent the high frequency analysis making several one minute average to see the effects of switching on the Hall term in time. We leave this study to the future.

In this work, it was not necessary to use the new MHDSTS scheme, as neither ambipolar, nor Hall term introduce severe restrictions on the time step. However, if we consider a constant vertical unipolar magnetic field for the initialization instead of a battery-seeded magnetic field, the ambipolar diffusion will introduce a time step limitation and the new scheme will be worth it to use.

7

Conclusions

In this thesis we have extended the numerical capabilities of the code Mancha3D to solve the non-ideal MHD equations when considering partially ionized plasmas under certain physical conditions. These physical conditions can establish highly demanding numerical requirements via the ambipolar diffusion term and/or the Hall term. In Chapters 2 and 3 we have introduced the theoretical concepts and Mancha3D code respectively.

The conclusion from Chapter 4 can be summarized as:

- The STS and HDS schemes are easy to implement and can also work together using the Strang operator splitting formalism.
- The accuracy order of the MHDSTS scheme is kept and limited to second order by the Strang operator splitting, but the stability of the scheme can be increased using a RK wrapper with each operator.
- The numerical experiments used as tests, show a good agreement with the analytical solution, making us confident enough to use the MHDSTS scheme to investigate stiff problems.
- The STS technique speeds up problematic simulations due to the restrictions imposed by the ambipolar/Ohmic diffusive terms.
- We must choose carefully ν and N_{STS} parameters because the smaller ν and/or bigger N_{STS} are, the bigger acceleration, errors and numerical instabilities as well as a slight decrease of accuracy order.
- The HDS technique solves the problem with complex eigenvalues introduced by the Hall term and is more stable than our standard RK scheme, specially when the Hall term is dominating.
- The HDS time step is improved when the ambipolar or ohmic diffusion are considered.
- Due to the whole scheme is explicit, it is straightforward to use the other capabilities already implemented in Mancha3D code (PML, AMR, radiative transfer, etc.).

The results from Chapter 5 can be summarized as:

- Numerical experiments allow us to relax the cold plasma approximation, done by Cally & Khomenko (2015), to study the coupling between fast magneto-acoustic and Alfvén waves even when there is no cross-field wave propagation. Our experiments indeed confirm this effect.
- The Hall-mediated conversion in warm plasma shows frequency and magnetic field dependence. The efficiency is also a sensitive function of the Hall parameter, and therefore it increases for increasing wave frequency ν and decreasing ionization fraction ξ_i. Our experiments show the transformation is more efficient for low frequencies and fields of the order of hG. The efficiency of the transformation for low-frequency waves is maximal for strongly inclined fields (50–70 degrees). However, for waves at higher frequencies, the maximum becomes progressively aligned with the field.
- In warm plasmas the transformation is a two-step process. First acoustic fast waves are partially transformed into magnetic fast waves at the equipartition layer ($v_A = c_s$), and then the latter are transformed into Alfvén waves progressively where Hall coupling operates.
- For the Hall-mediated transformation to be efficient one needs to satisfy simultaneously two conditions: (1) that the layer with $v_A = c_s$ is located below the layer with maximum $\epsilon_{\rm Hall}$, therefore B_0 has to be sufficiently large to have $v_A = c_s$ located deep enough; (2) that B is sufficiently small to maximize the value of $\epsilon_{\rm Hall}$.
- Hall-mediated transformation acts in addition to the geometrical mode transformation to Alfvén waves suggested by Cally & Goossens (2008). It does not need any particular relation between the wave vector and the orientation of the magnetic field. Our simulations suggest that the maximum transformation can occur for a broad range of magnetic field inclinations, depending on the wave frequency. Also, the considerations above suggest that the process would be efficient for intermediate field strengths of the order of hG, comparable to those existing in solar network and quiet areas. Therefore, this process could provide a constant energy supply by means of Alfvén waves to the solar corona.
- After normalizing the wave amplitude of $v_{\rm long}$ to be 500 m s^{-1} at $\beta = 1$, using Eq. (5.20), corresponds to an average acoustic wave energy flux of $\sim 3.8 \times 10^4$ W m^{-2} and a spatio-temporal RMS value of about 368 W m^{-2}. For waves of 1 Hz, the average Alfvénic energy flux we obtain at 450 km height (above the height of peak Hall coupling) is about 10^3 W m^{-2} with a RMS of 780 W m^{-2}. These numbers are bigger than what is required for heating the corona above quiet Sun regions, which is about 100–300 W m^{-2}, but are of the order of what is needed for heating the corona above active regions (Withbroe & Noyes 1977). However, because these values depend of the adopted base amplitude, it is probably overestimated at this frequency.
- Assuming we can convert 1% of the generated acoustic flux into Alfvén waves and bring it to the solar corona, a good fraction of the energy needed to compensate its losses would be provided by Hall coupling. Although this flux is small compared to the peak acoustic flux at the same height, the Alfvén flux is far more able to penetrate to the corona, and so is more relevant to coronal heating.
- Possibly, Hall-mediated conversion can be important for other astrophysical scenarios, e.g. in star formation regions or reconnection events as well as in other cooler stars.

The results from Chapter 6 can be summarized as:

- When the Hall term is included in the simulations, it plays an important role by changing the magnetic field structure by allowing the existence of stronger and more vertical fields at the higher layers. It also introduces a non-geometrical way to transform fast magneto-acoustic waves into Alfvén waves increasing the currents variations. These currents are dissipated by the ambipolar term with the consequent heating of the atmosphere and also on the increase of the probability of finding more points with high temperature at chromospheric layers over the simulation time.
- With the Hall term included, it increases the shear contribution of the Poynting flux, in contrast with the case when only ambipolar diffusion is taking into account.
- When the Hall term is considered, it increases the number of vortices, which can work as waveguide for Alfvén waves making a way for them to reach upper layers easily.

Acknowledgments

En primer lugar me gustaría agrader a mi directora Elena Khomenko y mi, primero codirector y luego tutor, Manolo Collados por todos los consejos, ayuda y soporte que me han ofrecido a lo largo de todo este tiempo de tesis y máster. Muchas gracias por haberme guiado a través de las distintas capas del intricando mundo de la investigación así como de la Física Solar. También quiero agradecer a Ángel de Vicente su inestimable ayuda durante el desarrollo y depuración del código, a sus consejos de programación, atajos del emacs o tuneles ssh sin los cuales todo hubiera sido mucho más complicado. Ha sido un placer no solo trabajar con ustedes durante todos estos años sino también poder hacer alguna escapada al Teide o un "pateillo" por la sierra de Madrid.

I also would like to thank Dr. Turlough Downes and Dr. Paul Cally for their invaluable advise and help with the work carried out with Chapters 4 and 5 respectively. I also would like to especially thank Dr. Nikola Vitas because without him and his contribution to MANCHA3D code this work would be not possible. I would like to thank Dr. Juan Martínez-Sykora and Dr. Sergiy Shelyag to accept the hard work of being referee of this thesis. Their comments and advise have been very fruitful to shape this work.

Sin duda, muchas gracias a toda la gente que me ha rodeado a lo largo de estos años en el IAC y en la Facultad, ya que sin ellos este periplo hubira sido muy aburrido. En especial y desordenadamente, me gustaría agradecer el haber estado ahí a Vane, Jorge (japp), Prysia, Ray, Tobías, Juan, Manuel Luna, Alex Ozcos, Manu, Pío, Ramón, Edgar, Sergio, Cristina Protasio. También me gustaría agradecer a profesores/mentores como Fernando Moreno, Basilio, Inés, Franz Kneer o Mike Thompson gracias a los cuales terminé decantándome por la Física Solar.

Por último, quiero darle las gracias a mis padres y hermana por su apoyo incondicional durante esta aventura. Gracias por toda la ayuda, cariño y educación recibida sin la cual esto no hubiera sido posible. También quiero extender este agradecimiento al resto de mi familia, incluyendo a los que se han marchado y a los que han llegado con alegría. De una forma especial, quiero darle las gracias a Laura, por aparecer cuando uno menos se lo espera, coincidiendo en el espacio y el tiempo para, de repente, pasar a compartir lugares y momentos. Espero que esta nueva etapa continúe.

Peter

This work is supported by the Ministerio de Economía y Competitividad through project AYA2014-55078-P and the predoctoral training grants in Centres/Units of Excellence 'Severo Ochoa' with reference SEV-2011-0187. It contributes to the deliverable identified in FP7 European Research Council grant agreement 277829, 'Magnetic connectivity through the Solar Partially Ionized Atmosphere'. We also wish to acknowledge the contribution of Teide High-Performance Computing facilities to the results of this research. TeideHPC facilities are provided by the Instituto Tecnológico y de Energías Renovables (ITER, SA). URL: http://teidehpc.iter.es. We thankfully acknowledges the technical expertise and assistance provided by the Spanish Supercomputing Network (Red Española de Supercomputación), as well as the computer resource LaPalma Supercomputer, located at the Instituto de Astrofísica de Canarias and MareNostrum (BSC/CNS/RES/PRACE), based in Barcelona/Spain.

Bibliography

Abbett, W. P., Fisher, G. H., & Fan, Y. 2000, The Astrophysical Journal, 540, 548, doi: 10.1086/309316 1

Alexiades, V. 1995, in 2nd International Conference on Dynamic Systems and Applications, Atlanta. http://citeseerx.ist.psu.edu/viewdoc/download?doi=10.1.1.123.5458&rep=rep1&type=pdf 4.3.2

Alexiades, V., Amiez, G., & Gremaud, P. A. 1996, Com. Num. Meth. Eng., 12, 31 4.3.2, 4.3.2, 4.3.2, 4.5

Alfvén, H. 1942, Nature, 150, 405, doi: 10.1038/150405d0 2.3.3

—. 1943, Arkiv f. Mat., 29B(2), 1 1

Anders, E., & Grevesse, N. 1989, Geochimica et Cosmochimica Acta, 53, 197, doi: 10.1016/0016-7037(89)90286-X 3.8

Arber, T. D., Haynes, M., & Leake, J. E. 2007, The Astrophysical Journal, 666, 541, doi: 10.1086/520046 6.4.2

Asplund, M., Nordlund, Å., Trampedach, R., Allende Prieto, C., & Stein, R. F. 2000, Astronomy and Astrophysics, 359, 729 1

Ballester, J. L., Alexeev, I., Collados, M., et al. 2018, Space Science Reviews, 214, #58, doi: 10.1007/s11214-018-0485-6 1, 1, 4.1, 5.2

Balsara, D. S. 1996, Astrophysical Journal v.465, 465, 775, doi: 10.1086/177462 4.4.2

Berenger, J.-P. 1994, Journal of Computational Physics, 114, 185, doi: 10.1006/jcph.1994.1159 3.1, 3.10.1

—. 1996, Journal of Computational Physics, 127, 363, doi: DOI:10.1006/jcph.1996.0181 3.1, 3.10.1

Berger, M. J., & Colella, P. 1989, Journal of Computational Physics (ISSN 0021-9991), 82, 64, doi: 10.1016/0021-9991(89)90035-1 3.1

Bittencourt, J. A. 2004, Fundamentals of Plasma Physics, 3rd edn. (New York, NY: Springer New York), doi: 10.1007/978-1-4757-4030-1. http://link.springer.com/10.1007/978-1-4757-4030-1 2.1, 2.1.2

Braginskii, S. I. 1965, Reviews of Plasma Physics, 1, 205 2.1.2, 2.2

Bushby, P. J., Houghton, S. M., Proctor, M. R. E., & Weiss, N. O. 2008, Monthly Notices of the Royal Astronomical Society, 387, 698, doi: 10.1111/j.1365-2966.2008.13276.x 1

Cally, P. S. 2006, Royal Society of London Philosophical Transactions Series A, 364, 333, doi: 10.1098/rsta.2005.1702 1, 2.4, 2.4

—. 2007, Astronomische Nachrichten, 328, 286, doi: 10.1002/asna.200610731 1, 2.4

—. 2009, Monthly Notices of the Royal Astronomical Society, 395, 1309, doi: 10.1111/j.1365-2966.2009.14708.x 2.4

—. 2017, Monthly Notices of the Royal Astronomical Society, 466, 413, doi: 10.1093/mnras/stw3215 6.4.2

Cally, P. S., & Goossens, M. 2008, Solar Physics, 251, 251, doi: 10.1007/s11207-007-9086-3 2.4, 2.5, 5.1, 5.4, 5.5, 7

Cally, P. S., & Hansen, S. C. 2011, The Astrophysical Journal, 738, 119, doi: 10.1088/0004-637X/738/2/119 2.4

Cally, P. S., & Khomenko, E. 2015, The Astrophysical Journal, 814, 106, doi: 10.1088/0004-637X/814/2/106 1, 5, 5.1, 5.4, 5.5, 6.1, 7

—. 2018, The Astrophysical Journal, 856, 20, doi: 10.3847/1538-4357/aaaf6a 3.1, 6.4.2

Carlsson, M., & Leenaarts, J. 2012, Astronomy and Astrophysics, 539, A39, doi: 10.1051/0004-6361/201118366 1

Carroll, B. W., & Ostlie, D. A. 1996, An Introduction to Modern Astrophysics 2.6

Cattaneo, F. 1999, The Astrophysical Journal, 515, L39, doi: 10.1086/311962 1

Cattaneo, F., Emonet, T., & Weiss, N. 2003, The Astrophysical Journal, 588, 1183, doi: 10.1086/374313 1

Chandrasekhar, S. 1961, Hydrodynamic and hydromagnetic stability (Oxford University Press). http://books.google.es/books?id=XsppugEACAAJ&dq=intitle:Hydrodynamic+and+hydromagnetic+stability&hl=&cd=4&source=gbs_api 1

Cheung, M. C. M., & Cameron, R. H. 2012, The Astrophysical Journal, 750, 6, doi: 10.1088/0004-637X/750/1/6 4.4.3, 5.1, 6.1

Choi, E., Kim, J., & Wiita, P. J. 2009, The Astrophysical Journal Supplement, 181, 413, doi: 10.1088/0067-0049/181/2/413 4.3.2, 4.4.2

Christensen-Dalsgaard, J. 2014, Lecture Notes on Stellar Oscillations, 5th edn. (Online Notes). http://www.phys.au.dk/~jcd/oscilnotes/ 2.3.2

Christensen-Dalsgaard, J., Dappen, W., Ajukov, S. V., et al. 1996, Science, 272, 1286, doi: 10.1126/science.272.5266.1286 5.3

Courant, R., Friedrichs, K., & Lewy, H. 1928, Mathematische Annalen, 100, 32, doi: 10.1007/BF01448839 3.4

Cowling, T. G. 1957, Magnetohydrodynamics (Interscience). http://cds.cern.ch/record/108571 4.1

Dawes, W. R. 1864, American Journal of Science, 38, 203, doi: 10.2475/ajs.s2-38.113.203 1

De Pontieu, B., Erdélyi, R., & James, S. P. 2004, Nature, 430, 536, doi: 10.1038/nature02749 1

De Pontieu, B., & Haerendel, G. 1998, Astronomy and Astrophysics, 338, 729 6.1

De Pontieu, B., McIntosh, S., Hansteen, V. H., et al. 2007a, Publications of the Astronomical Society of Japan, 59, S655, doi: 10.1093/pasj/59.sp3.S655 1

De Pontieu, B., McIntosh, S. W., Carlsson, M., et al. 2007b, Science, 318, 1574, doi: 10.1126/science.1151747 1

—. 2007c, Science, 318, 1574, doi: 10.1126/science.1151747 2.4

DeRosa, M. L., & Toomre, J. 2004, The Astrophysical Journal, 616, 1242, doi: 10.1086/424920 1

Domínguez Cerdeña, I., Sánchez Almeida, J., & Kneer, F. 2006, The Astrophysical Journal, 636, 496, doi: 10.1086/497955 6.4.1

Draine, B. T. 1980, Astrophysical Journal, 241, 1021, doi: 10.1086/158416 4.4.4

Falle, S. A. E. G. 2003, Monthly Notices of the Royal Astronomical Society, 344, 1210, doi: 10.1046/j.1365-8711.2003.06908.x 4.4.4

Felipe, T. 2012, The Astrophysical Journal, 758, 96, doi: 10.1088/0004-637X/758/2/96 2.4, 5.1, 5.4, 5.4

Felipe, T., Braun, D. C., Crouch, A. D., & Birch, A. C. 2016, The Astrophysical Journal, 829, 67, doi: 10.3847/0004-637X/829/2/67 3.1

Felipe, T., Crouch, A., & Birch, A. 2013, The Astrophysical Journal, 775, 74, doi: 10.1088/0004-637x/775/1/74 3.1

Felipe, T., Khomenko, E., & Collados, M. 2010, The Astrophysical Journal, 719, 357, doi: 10.1088/0004-637X/719/1/357 3, 3.1, 3.4, 4.1, 4.3.2, 4.4, 4.4.1, 5.4

Ferraro, C. A., & Plumpton, C. 1958, The Astrophysical Journal, 127, 459, doi: 10.1086/146474 2.3.4

Forteza, P., Oliver, R., Ballester, J. L., & Khodachenko, M. L. 2007, Astronomy and Astrophysics, 461, 731, doi: 10.1051/0004-6361:20065900 1

Fossum, A., & Carlsson, M. 2006, The Astrophysical Journal, 646, 579, doi: 10.1086/504887 5.5

Galloway, D. J., Proctor, M. R. E., & Weiss, N. O. 1977, Nature, 266, 686, doi: 10.1038/266686a0 1

Gentzsch, W. 1980, in Proceedings of the Third GAMM—Conference on ... (Wiesbaden: Vieweg+Teubner Verlag), 109–117. http://link.springer.com/10.1007/978-3-322-86146-7_11 4.3.2

Gingerich, O., Noyes, R. W., Kalkofen, W., & Cuny, Y. 1971, Solar Physics, 18, 347, doi: 10.1007/BF00149057 6.3

Goedbloed, J. P., Keppens, R., & Poedts, S. 2010, Advanced Magnetohydrodynamics, With Applications to Laboratory and Astrophysical Plasmas (Cambridge University Press). http://adsabs.harvard.edu/abs/2010adma.book.....G 2.5

Gonzalez-Morales, P. A., Khomenko, E., & Cally, P. S. 2019, The Astrophysical Journal, 870, 94, doi: 10.3847/1538-4357/aaf1a9 5

Gonzalez-Morales, P. A., Khomenko, E., Downes, T. P., & de Vicente, A. 2018, Astronomy and Astrophysics, 615, A67, doi: 10.1051/0004-6361/201731916 4, 5.3

Goodman, M. L. 2000, The Astrophysical Journal, 533, 501, doi: 10.1086/308635 6.1

—. 2011, The Astrophysical Journal, 735, 45, doi: 10.1088/0004-637X/735/1/45 6.1

Goossens, M. 2003, Astrophysics and Space Science Library, Vol. 294, An introduction to plasma astrophysics and magnetohydrodynamics (Dordrecht: Springer, Dordrecht), doi: 10.1007/978-94-007-1076-4. http://adsabs.harvard.edu/cgi-bin/nph-data_query?bibcode=2003ASSL..294.....G&link_type=EJOURNAL 2.5

Grewenig, S., Weickert, J., & Bruhn, A. 2010, in Pattern Recognition (Berlin, Heidelberg: Springer, Berlin, Heidelberg), 533–542. https://link.springer.com/chapter/10.1007/978-3-642-15986-2_54 4.3.2

Gudiksen, B. V., Carlsson, M., Hansteen, V. H., et al. 2011, Astronomy and Astrophysics, 531, A154, doi: 10.1051/0004-6361/201116520 1, 4.1

Gurski, K., & O'Sullivan, S. 2011, SIAM Journal on Numerical Analysis, 49, 368, doi: 10.1137/090775804 4.3.2, 4.3.2

Hansteen, V. H., De Pontieu, B., Rouppe van der Voort, L., van Noort, M., & Carlsson, M. 2006, The Astrophysical Journal, 647, L73, doi: 10.1086/507452 1

Hayek, W., Asplund, M., Carlsson, M., et al. 2010, Astronomy and Astrophysics, 517, A49, doi: 10.1051/0004-6361/201014210 1

Herschel, W. 1801, Philosophical Transactions of the Royal Society of London, 91, 265, doi: 10.2307/107097 1

Hesthaven, J. S. 1998, Journal of Computational Physics, 142, 129, doi: 10.1006/jcph.1998.5938 3.1, 3.7

Hu, F. Q. 1996, Journal of Computational Physics, 129, 201, doi: 10.1006/jcph.1996.0244 3.1, 3.10.1

—. 2001, Journal of Computational Physics, 173, 455, doi: 10.1006/jcph.2001.6887 3.1, 3.10.1

Huba, J. L. 2016, Plasma Physics Division (Naval Research Laboratory). http://scholar.google.com/scholar?q=related:sc_wmLeSBIYJ:scholar.google.com/&hl=en&num=20&as_sdt=0,5 2.2

Hunt, J. C. R., Wray, A. A., & Moin, P. 1988, In its Studying Turbulence Using Numerical Simulation Databases 6.6

Hurlburt, N. E., & Rucklidge, A. M. 2000, Monthly Notices of the Royal Astronomical Society, 314, 793, doi: 10.1046/j.1365-8711.2000.03407.x 1

Hurlburt, N. E., & Toomre, J. 1988, Astrophysical Journal, 327, 920, doi: 10.1086/166250 1

Hyndman, R. J., & Koehler, A. B. 2006, International journal of forecasting, 22, 679, doi: 10.1016/j.ijforecast.2006.03.001 4.4.2

Janssen, J. 1896, Annales de l'Observatoire d'astronomie physique de Paris sis Parc de Meudon, ed. J. Janssen, Vol. 1 (Gauthier-Villars (Paris)). https://gallica.bnf.fr/ark:/12148/bpt6k6537478r/ 1, 1.4

Jess, D. B., Mathioudakis, M., Erdélyi, R., et al. 2009, Science, 323, 1582, doi: 10.1126/science.1168680 2.4

Jess, D. B., Pascoe, D. J., Christian, D. J., et al. 2012, The Astrophysical Journal Letters, 744, L5, doi: 10.1088/2041-8205/744/1/L5 2.4

Judge, P. 2008, The Astrophysical Journal Letters, 683, L87, doi: 10.1086/591470 6.1

Khodachenko, M. L., Arber, T. D., Rucker, H. O., & Hanslmeier, A. 2004, Astronomy and Astrophysics, 422, 1073, doi: 10.1051/0004-6361:20034207 1

Khomenko, E., & Cally, P. S. 2011, Journal of Physics Conference Series, 271, 012042, doi: 10.1088/1742-6596/271/1/012042 2.4, 5.4, 5.4

—. 2012, The Astrophysical Journal, 746, 68, doi: 10.1088/0004-637X/746/1/68 2.4, 2.4, 5.1, 5.3, 5.4, 5.4

Khomenko, E., & Collados, M. 2006, The Astrophysical Journal, 653, 739, doi: 10.1086/507760 1, 3.1, 3.4, 4.1

—. 2009, Astronomy and Astrophysics, 506, L5, doi: 10.1051/0004-6361/200913030 5.4

—. 2012, The Astrophysical Journal, 747, 87, doi: 10.1088/0004-637X/747/2/87 1, 3.1, 4.1, 6.1, 6.4.4

Khomenko, E., Collados, M., Díaz, A., & Vitas, N. 2014, Physics of Plasmas, 21, 092901, doi: 10.1063/1.4894106 1, 2.1, 2.1, 2.1.2, 2.1, 2.2, 4.1, 4.2, 4.3.2, 4.3.2, 5.2, 6.1, 6.2, 6.1

Khomenko, E., Vitas, N., Collados, M., & de Vicente, A. 2017, Astronomy and Astrophysics, 604, A66, doi: 10.1051/0004-6361/201630291 1, 1, 2.2.1, 3.1, 4.1, 6.2, 6.4.1

—. 2018, Astronomy and Astrophysics, 618, A87, doi: 10.1051/0004-6361/201833048 1, 1, 3.1, 3.9, 6.1, 6.3, 6.3, 6.3, 6.4, 6.4.1, 6.4.3, 6.4.4, 6.5

Kigure, H., Takahashi, K., Shibata, K., Yokoyama, T., & Nozawa, S. 2010, Publications of the Astronomical Society of Japan, 62, 993, doi: 10.1093/pasj/62.4.993 2.4

Kolář, V. 2007, International Journal of Heat and Fluid Flow, 28, 638, doi: 10.1016/j.ijheatfluidflow.2007.03.004 6.6

Krasnoselskikh, V., Vekstein, G., Hudson, H. S., Bale, S. D., & Abbett, W. P. 2010, The Astrophysical Journal, 724, 1542, doi: 10.1088/0004-637X/724/2/1542 6.1

Kudoh, T., & Shibata, K. 1999, The Astrophysical Journal, 514, 493, doi: 10.1086/306930 2.4

Kulsrud, R., & Pearce, W. P. 1969, Astrophysical Journal, 156, 445, doi: 10.1086/149981 4.4.2

Kulsrud, R. M., & Zweibel, E. G. 2008, Reports on Progress in Physics, 71, 046901, doi: 10.1088/0034-4885/71/4/046901 2.2.1

Kumar, N., & Roberts, B. 2003, Solar Physics, 214, 241, doi: 10.1023/A:1024299029918 1

Kurucz, R. 1993, ATLAS9 Stellar Atmosphere Programs and 2 km/s grid. Kurucz CD-ROM No. 13. Cambridge, 13 3.9

Kuźma, B., Wójcik, D., & Murawski, K. 2019, The Astrophysical Journal, 878, 81, doi: 10.3847/1538-4357/ab1b4a 6.1

Langangen, Ø., De Pontieu, B., Carlsson, M., et al. 2008, The Astrophysical Journal Letters, 679, L167, doi: 10.1086/589442 1

Leake, J. E., & Arber, T. D. 2006, Astronomy and Astrophysics, 450, 805, doi: 10.1051/0004-6361:20054099 6.4.2

Leake, J. E., DeVore, C. R., Thayer, J. P., et al. 2014, Space Science Reviews, 184, 107, doi: 10.1007/s11214-014-0103-1 1

Leenaarts, J., Carlsson, M., Hansteen, V., & Gudiksen, B. V. 2011, Astronomy and Astrophysics, 530, A124, doi: 10.1051/0004-6361/201016392 1

Lemen, J. R., Title, A. M., Akin, D. J., et al. 2012, Solar Physics, 275, 17, doi: 10.1007/s11207-011-9776-8 1.3

LeVeque, R. J. 2002, Finite Volume Methods for Hyperbolic Problems (Cambridge Texts in Applied Mathematics) (CUP). http://libgen.io/ads.php?md5=1A50F82DCDC6701FD5B50ED46C4BCD1A 4.3.2, 4.4.2

Lodato, G., & Price, D. 2010, arXiv.org, 1212, doi: 10.1111/j.1365-2966.2010.16526.x 4.3.2

Luna, M., Terradas, J., Khomenko, E., Collados, M., & de Vicente, A. 2016, The Astrophysical Journal, 817, 157, doi: 10.3847/0004-637X/817/2/157 3.1

Maneva, Y. G., Alvarez Laguna, A., Lani, A., & Poedts, S. 2017, The Astrophysical Journal, 836, 197, doi: 10.3847/1538-4357/aa5b83 6.1

Martínez-Sykora, J., De Pontieu, B., Carlsson, M., & Hansteen, V. 2016, The Astrophysical Journal Letters, 831, L1, doi: 10.3847/2041-8205/831/1/L1 6.1

Martínez-Sykora, J., De Pontieu, B., Carlsson, M., et al. 2017, The Astrophysical Journal, 847, 36, doi: 10.3847/1538-4357/aa8866 1, 6.1

Martínez-Sykora, J., De Pontieu, B., De Moortel, I., Hansteen, V. H., & Carlsson, M. 2018, The Astrophysical Journal, 860, 116, doi: 10.3847/1538-4357/aac2ca 1

Martínez-Sykora, J., De Pontieu, B., & Hansteen, V. 2012, The Astrophysical Journal, 753, 161, doi: 10.1088/0004-637X/753/2/161 1, 1, 4.1, 6.1

McIntosh, S. W., De Pontieu, B., Carlsson, M., et al. 2011, Nature, 475, 477, doi: 10.1038/nature10235 2.4

Meier, E. T., & Shumlak, U. 2012, Physics of Plasmas, 19, 072508, doi: 10.1063/1.4736975 4.1

Meyer, C. D., Balsara, D. S., & Aslam, T. D. 2012, Monthly Notices of the Royal Astronomical Society, 422, 2102, doi: 10.1111/j.1365-2966.2012.20744.x 4.3.2

—. 2014, Journal of Computational Physics, 257, 594, doi: 10.1016/j.jcp.2013.08.021 4.3.2

Mihalas, D. 1967, Methods in Computational Physics, 7, 1 3.8

—. 1978, Stellar atmospheres /2nd edition/ (San Francisco, W. H. Freeman and Co., 1978. 650 p.). http://adsabs.harvard.edu/abs/1978stat.book.....M 2.1

Mihalas, D., & Mihalas, B. W. 1984, Foundations of radiation hydrodynamics (New York: Oxford University Press). http://adsabs.harvard.edu/abs/1984oup..book.....M 5.3

Morse, P., & Ingard, K. U. 1968, Theoretical acoustics, 1st edn. (McGraw-Hill), doi: 10.1119/1.1976432. http://books.google.com/books?hl=en&lr=&id=KIL4MV9IE5kC&oi=fnd&pg=PR7&dq=Theoretical+Acoustics+morse&ots=hkRdC6ViM3&sig=qsoOqhW1wI49wr5-kCkqm4NdB2k 4.4.2

Musielak, Z. E., Rosner, R., Stein, R. F., & Ulmschneider, P. 1994, The Astrophysical Journal, 423, 474, doi: 10.1086/173825 5.5

Nasmyth, J. 1865, Astronomical Register, 3, 223 1

Nóbrega-Siverio, D., Martínez-Sykora, J., Moreno-Insertis, F., & Rouppe van der Voort, L. 2017, The Astrophysical Journal, 850, 153, doi: 10.3847/1538-4357/aa956c 1

Nóbrega-Siverio, D., Moreno-Insertis, F., & Martínez-Sykora, J. 2016, The Astrophysical Journal, 822, 18, doi: 10.3847/0004-637X/822/1/18 1

—. 2018, The Astrophysical Journal, 858, 8, doi: 10.3847/1538-4357/aab9b9 1

Nordlund, Å. 1982, Astronomy and Astrophysics, 107, 1 1, 3.9

Nordlund, Å. 1983, in IN: Solar and stellar magnetic fields: Origins and coronal effects; Proceedings of the Symposium, Copenhagen University Observatory, Copenhagen, Denmark, 79–83. https://ui.adsabs.harvard.edu/abs/1983IAUS..102...79N/abstract 1

Nordlund, Å., & Galsgaard, K. 1995, A 3D MHD code for Parallel Computers (NBIfAFG, Astronomical Observatory). http://www.uio.no/studier/emner/matnat/astro/AST5110/h09/undervisningsmateriale/mhd.pdf 3.1, 3.3

Nordlund, Å., Stein, R. F., & Asplund, M. 2009, Living Reviews in Solar Physics, 6, 2, doi: 10.12942/lrsp-2009-2 1, 1, 2.5

Olson, G. L., & Kunasz, P. B. 1987, Journal of Quantitative Spectroscopy and Radiative Transfer, 38, 325, doi: 10.1016/0022-4073(87)90027-6 3.9

O'Sullivan, S., & Downes, T. P. 2006, Monthly Notices of the Royal Astronomical Society, 366, 1329, doi: 10.1111/j.1365-2966.2005.09898.x 4.3.2, 4.3.2, 4.3.2, 4.3.2, 4.4.4

—. 2007, Monthly Notices of the Royal Astronomical Society, 376, 1648, doi: 10.1111/j.1365-2966.2007.11429.x 4.3.2, 4.3.2, 4.4.4

Pandey, B. P., & Wardle, M. 2008, Monthly Notices of the Royal Astronomical Society, 385, 2269, doi: 10.1111/j.1365-2966.2008.12998.x 1, 4.1

Parchevsky, K. V., & Kosovichev, A. G. 2007, The Astrophysical Journal, 666, 547, doi: 10.1086/520108 3.1, 3.7

—. 2009, The Astrophysical Journal, 694, 573, doi: 10.1088/0004-637X/694/1/573 3.1, 3.10.1

Parker, E. N. 2007, Conversations on Electric and Magnetic Fields in the Cosmos, by Eugene N. Parker. ISBN-10 0-691-12840-5 (HB); ISBN-13 978-0-691-12840-5 (HB). Published by Princeton University Press, Princeton, NJ USA, 2007. 4.1

Pereira, T. M. D., De Pontieu, B., Carlsson, M., et al. 2014, The Astrophysical Journal Letters, 792, L15, doi: 10.1088/2041-8205/792/1/L15 1

Pesnell, W. D., Thompson, B. J., & Chamberlin, P. C. 2012, Solar Physics, 275, 3, doi: 10.1007/s11207-011-9841-3 1, 1.3

Popescu Braileanu, B., Lukin, V. S., Khomenko, E., & de Vicente, A. 2019a, Astronomy and Astrophysics, 627, A25, doi: 10.1051/0004-6361/201834154 1, 6.1

—. 2019b, Astronomy and Astrophysics, 630, A79, doi: 10.1051/0004-6361/201935844 6.1

Price, D. J., & Federrath, C. 2010a, Monthly Notices of the Royal Astronomical Society, 406, 1659, doi: 10.1111/j.1365-2966.2010.16810.x 4.3.2

—. 2010b, Numerical Modeling of Space Plasma Flows, 429, 274 4.3.2

Price, D. J., Wurster, J., Tricco, T. S., et al. 2018, Publications of the Astronomical Society of Australia, 35, e031, doi: 10.1017/pasa.2018.25 4.3.2

Priest, E. 2014, Magnetohydrodynamics of the Sun (Cambridge: Cambridge University Press), doi: 10.1017/CBO9781139020732. http://adsabs.harvard.edu/cgi-bin/nph-data_query?bibcode=2014masu.book.....P&link_type=EJOURNAL 1.1, 2.3.2, 4.1

Rempel, M. 2014, The Astrophysical Journal, 789, 132, doi: 10.1088/0004-637X/789/2/132 6.4.1

—. 2017, The Astrophysical Journal, 834, 10, doi: 10.3847/1538-4357/834/1/10 1.6, 1, 4.3.2

Richardson, L. F. 1911, Philosophical Transactions of the Royal Society of London. Series A, 210, 307 4.3.2

Richardson, L. F., & Gaunt, J. A. 1927, Philosophical Transactions of the Royal Society of London. Series A, 226, 299, doi: 10.1098/rsta.1927.0008 4.3.2

Rouppe van der Voort, L. H. M., De Pontieu, B., Hansteen, V. H., Carlsson, M., & van Noort, M. 2007, The Astrophysical Journal, 660, L169, doi: 10.1086/518246 1

Rutten, R. J. 1995, Helioseismology. ESA SP, 376, 151 1

—. 2007, The Physics of Chromospheric Plasmas ASP Conference Series, 368, Heinzel 1

Santamaria, I. C., Khomenko, E., & Collados, M. 2015, Astronomy and Astrophysics, 577, A70, doi: 10.1051/0004-6361/201424701 5.4

Santamaria, I. C., Khomenko, E., Collados, M., & de Vicente, A. 2016, Astronomy and Astrophysics, 590, L3, doi: 10.1051/0004-6361/201628515 3.1

—. 2017, Astronomy and Astrophysics, 602, A43, doi: 10.1051/0004-6361/201629729 5.5

Santamaria, I. C., & Van Doorsselaere, T. 2018, Astronomy and Astrophysics, 611, A10, doi: 10.1051/0004-6361/201731016 1.7, 1

Schaffenberger, W., Wedemeyer-Böhm, S., Steiner, O., & Freytag, B. 2005, in Proceedings of the International Scientific Conference on Chromospheric and Coronal Magnetic Fields (ESA SP-596). 30 August - 2 September 2005, 65.1. http://adsabs.harvard.edu/abs/2005ESASP.596E..65S 1

Scherrer, P. H., Schou, J., Bush, R. I., et al. 2012, Solar Physics, 275, 207, doi: 10.1007/s11207-011-9834-2 1.3

Schrijver, C. J., & Title, A. M. 2003, The Astrophysical Journal, 597, L165, doi: 10.1086/379870 1

Schrijver, C. J., & van Ballegooijen, A. A. 2005, The Astrophysical Journal, 630, 552, doi: 10.1086/431754 1

Schunker, H., & Cally, P. S. 2006, Monthly Notices of the Royal Astronomical Society, 372, 551, doi: 10.1111/j.1365-2966.2006.10855.x 2.4

Schunker, H., Cameron, R. H., Gizon, L., & Moradi, H. 2011, Solar Physics, 271, 1, doi: 10.1007/s11207-011-9790-x 5.3

Schüssler, M. 2001, Advanced Solar Polarimetry – Theory, 236, 343 1

Schüssler, M., & Vögler, A. 2008, Astronomy and Astrophysics, 481, L5, doi: 10.1051/0004-6361:20078998 1

Shelyag, S., Khomenko, E., de Vicente, A., & Przybylski, D. 2016, The Astrophysical Journal, 819, L11, doi: 10.3847/2041-8205/819/1/L11 1, 6.1, 6.4.2

Skartlien, R., Stein, R. F., & Nordlund, Å. 2000, The Astrophysical Journal, 541, 468, doi: 10.1086/309414 1

Skogsrud, H., Rouppe van der Voort, L., & De Pontieu, B. 2016, The Astrophysical Journal, 817, 124, doi: 10.3847/0004-637X/817/2/124 1

Soler, R., Oliver, R., & Ballester, J. L. 2009, The Astrophysical Journal, 699, 1553, doi: 10.1088/0004-637X/699/2/1553 1

—. 2010, Astronomy and Astrophysics, 512, A28, doi: 10.1051/0004-6361/200913478 1

Spiegel, E. A., & Zahn, J. P. 1992, Astronomy and Astrophysics (ISSN 0004-6361), 265, 106 1

Spitzer, L. 1956, Physics of Fully Ionized Gases (New York: Interscience Publishers, Inc.). http://adsabs.harvard.edu/abs/1956pfig.book.....S 2.2

Spruit, H. C. 1974, Solar Physics, 34, 277, doi: 10.1007/BF00153665 3.10.2, 6.3

Srivastava, A. K., Shetye, J., Murawski, K., et al. 2017, Scientific Reports, 7, 43147, doi: 10.1038/srep43147 2.4

Stein, R. F. 2012, Living Reviews in Solar Physics, 9, 4, doi: 10.12942/lrsp-2012-4 1

Stein, R. F., & Nordlund, Å. 2006, The Astrophysical Journal, 642, 1246, doi: 10.1086/501445 1

Strang, G. 1968, SIAM Journal on Numerical Analysis, 5, 506, doi: 10.1137/0705041 4.3.2

Tomczyk, S., McIntosh, S. W., Keil, S. L., et al. 2007, Science, 317, 1192, doi: 10.1126/science.1143304 2.4

Tomida, K., Tomisaka, K., Matsumoto, T., et al. 2013, The Astrophysical Journal, 763, 6, doi: 10.1088/0004-637X/763/1/6 4.3.2

Tóth, G., van der Holst, B., Sokolov, I. V., et al. 2012, Journal of Computational Physics, 231, 870, doi: 10.1016/j.jcp.2011.02.006 4.4.1

Tracy, E. R., Kaufman, A. N., & Brizard, A. J. 2003, Physics of Plasmas, 10, 2147, doi: 10.1063/1.1543579 2.4

Trujillo Bueno, J., Shchukina, N., & Asensio Ramos, A. 2004, Nature, 430, 326, doi: 10.1038/nature02669 1

Tsukamoto, Y., Iwasaki, K., & Inutsuka, S.-i. 2013, Monthly Notices of the Royal Astronomical Society, 434, 2593, doi: 10.1093/mnras/stt1205 4.3.2

van Leer, B., Tai, C.-H., & Powel, K. G. 1989, in 9th Computational Fluid Dynamics Conference (American Institute of Aeronautics and Astronautics). http://arc.aiaa.org/doi/10.2514/6.1989-1933 4.3.1

Vernazza, J. E., Avrett, E. H., & Loeser, R. 1981, The Astrophysical Journal Supplement Series, 45, 635, doi: 10.1086/190731 1.2, 1, 1, 5.1, 5.3

Vögler, A., Bruls, J. H. M. J., & Schüssler, M. 2004, Astronomy and Astrophysics, 421, 741, doi: 10.1051/0004-6361:20047043 3.9

Vögler, A., & Schüssler, M. 2007, Astronomy and Astrophysics, 465, L43, doi: 10.1051/0004-6361:20077253 6.3, 6.4.1

Vögler, A., Shelyag, S., Schüssler, M., et al. 2005, Astronomy and Astrophysics, 429, 335, doi: 10.1051/0004-6361:20041507 1, 3.1, 3.2, 3.4, 3.10.2, 4.1, 6.3

Vranjes, J., & Krstic, P. S. 2013, Astronomy and Astrophysics, 554, A22, doi: 10.1051/0004-6361/201220738 2.2

Vranjes, J., Poedts, S., Pandey, B. P., & De Pontieu, B. 2008, Astronomy and Astrophysics, 478, 553, doi: 10.1051/0004-6361:20078274 1

Wedemeyer-Böhm, S., Lagg, A., & Nordlund, Å. 2009, Space Science Reviews, 144, 317, doi: 10.1007/s11214-008-9447-8 1.5

Wedemeyer-Böhm, S., & Wöger, F. 2007, Proceedings of the International Astronomical Union, 3, 66, doi: 10.1017/S1743921308014671 1

Weiss, N. O. 1966, in Proceedings of The Royal Society of London. Series A, 310–328. http://adsabs.harvard.edu/cgi-bin/nph-data_query?bibcode=1966RSPSA.293..310W&link_type=EJOURNAL 1

Withbroe, G. L., & Noyes, R. W. 1977, In: Annual review of astronomy and astrophysics. Volume 15. (A78-16576 04-90) Palo Alto, 15, 363, doi: 10.1146/annurev.aa.15.090177.002051 5.5, 7

Wurster, J., Price, D., & Ayliffe, B. 2014, Monthly Notices of the Royal Astronomical Society, 444, 1104, doi: 10.1093/mnras/stu1524 4.3.2, 4.4.2

Xia, C., & Keppens, R. 2016, The Astrophysical Journal, 823, 22, doi: 10.3847/0004-637X/823/1/22 4.3.2

Xia, C., Keppens, R., & Fang, X. 2017, Astronomy and Astrophysics, 603, A42, doi: 10.1051/0004-6361/201730660 4.3.2

Zaqarashvili, T. V., Khodachenko, M. L., & Rucker, H. O. 2011, Astronomy and Astrophysics, 529, A82, doi: 10.1051/0004-6361/201016326 1, 4.1

Zhugzhda, I. D., & Dzhalilov, N. S. 1984, Astronomy and Astrophysics (ISSN 0004-6361), 132, 45 2.3.4